Using Density Matrix Renormalization Group to Study Open Quantum Systems

Cheng Guo

München 2012

Using Density Matrix Renormalization Group to Study Open Quantum Systems

Cheng Guo

Dissertation
an der Fakultät für Physik
der Ludwig–Maximilians–Universität
München

vorgelegt von
Cheng Guo
aus Linyi

München, den 30.10.2012

Erstgutachter: Prof. Jan von Delft
Zweitgutachter: Prof. Ulrich Schollwöck
Tag der mündlichen Prüfung: 12 December 2012

Contents

Abstract

This thesis is concerned with open quantum systems, and more specifically, quantum impurity models. By this we mean a small local quantum system in contact with a macroscopic non-interacting environment. This can be used to model individual impurities in metals and quantum information systems where the influence from the surrounding environment is not negligible. The numerical renormalization group (NRG) is the traditional method to study quantum impurity models. However its application is limited when dealing with real-time dynamics and bosonic systems. In recent years some of NRG's techniques have been introduced to the density matrix renormalization group method (DMRG), which itself is the most powerful numerical method to study one-dimensional quantum systems. The resulting method shows great potential, and this thesis explores and extends the power of the NRG+DMRG combination in treating open quantum systems.

We focus mainly on two types of problem. The first is an open quantum system with a time-dependent Hamiltonian, which for example could be the theoretical description of various problems encountered in qubit manipulation. We combine NRG discretization and adaptive time-dependent DMRG (t-DMRG) to study the dissipative Landau-Zener problem. We also use this method to study the quantum decoherence process and the dynamical properties of the telegraph noise model. The results show that the NRG and t-DMRG combination is a fast, accurate and versatile method for such problems. The second type of problem we study involves the quantum critical properties of one- and two-bath spin-boson models. Unlike fermion and spin models, models with bosons are difficult to treat numerically as each boson basis has an infinite number of dimensions. By introducing the optimal boson basis into the variational matrix product state method (VMPS), which is a variant of DMRG, we can deal with an effective local boson basis as large as 10^{10}. This is the crucial improvement over NRG which can only deal with at most a few dozen local basis states. With this powerful tool we have settled a controversy about the nature of the quantum phase transition in a sub-Ohmic spin-boson model regarding quantum to classical mapping. There, NRG fails to yield the right result due to the highly truncated local boson basis. We also explore the phase diagram of the two-bath spin-boson model and find a new critical phase. We demonstrate that NRG+VMPS with optimal boson basis represents a powerful setting to study quantum impurity models with a bosonic environment.

Zusammenfassung

Diese Dissertation handelt von offenen Quantensystemen, mit Spezialisierung auf Quantenstörstellenmodelle. Diese sind kleine lokale Quantensysteme, die im Kontakt mit einer makroskopischen nichtwechselwirkenden Umgebung stehen. Sie sind nützlich, um einzelne Störstellen in Metallen und Quanteninformationssystemen zu untersuchen, bei denen der Einfluss der Umgebung nicht vernachlässigbar ist, und deren Beschreibung im Falle einer starken Ankopplung über eine einfache perturbative Beschreibung hinausgeht. Die numerische Renormierungsgruppe (NRG) ist eine Standardmethode für die Untersuchung von Quantenstörstellenmodellen. Allerdings kann sie nur begrenzt auf dynamische Systeme und Systeme von Bosonen angewendet werden. In den letzten Jahren wurden einige NRG Methoden auf die Dichtematrix Renormierungsgruppe (DMRG) übertragen – eine mächtige quasi-exakte numerische Methode für die Untersuchung eindimensionaler Systeme. Die Kombination beider Methoden (NRG+DMRG) bietet daher einen breiten starken Rahmen, der in dieser Dissertation auf offene Quantensysteme angewendet wird.

Der Schwerpunkt liegt dabei auf zwei Arten von Problemen. Der erste Schwerpunkt bezieht sich auf offene Quantensysteme. Dies spielt eine wichtige Rolle in der theoretischen Beschreibung von Problemen in Bezug auf qubit Manipulation. Wir kombinieren die NRG Diskretisierung und die adaptive zeitabhängige DMRG (t-DMRG), um das dissipative Landau-Zener Problem zu untersuchen. Wir nutzen diese Methode ebenfalls, um die Quantendekohärenz und dynamische Eigenschaften von Telegraphrauschmodellen zu untersuchen. Die Ergebnisse belegen, dass die NRG und t-DMRG Kombination eine schnelle, genaue und vielseitige Methode für solche Probleme darstellt. Der Zweite Schwerpunkt handelt von kritischen Quanteneigenschaften von Spin-Boson Modellen mit einem, bzw. zwei Bädern. Anders als bei fermionischen und Spinmodellen ist es schwierig, Modelle mit Bosonen numerisch zu beschreiben, da jedes Boson bereits eine unendliche Anzahl an Zuständen hat. Indem wir die optimale Bosonenbasis in eine Art von DMRG, die variationelle Matrixproduktzustandmethode (VMPS), einführen, können wir eine effektive lokale Bosonenbasis der Größenordnung 10^{10} erreichen. Dies ist eine enorme Verbesserung gegenüber der NRG, die höchstens einige Dutzend lokale Basiszustände beschreiben kann. Mit diesem mächtigen Werkzeug konnten wir die Kontroverse über die Art des Quantenphasenübergangs in einem sub-ohmschen Spin-Boson Modell auflösen. NRG kann in diesem Fall wegen der stark reduzierten lokalen Bosonenbasis keine korrekten Vorhersagen liefern. Wir untersuchen ebenfalls das Phasendiagramm des Spin-Boson Modells mit zwei Bädern und finden eine neue kritische Phase. Wir zeigen, dass NRG+VMPS mit der optimalen

Bosonenbasis eine mächtige Methode für die Untersuchung von Quantenstörstellenmodellen in einer bosonischen Umgebung darstellt.

Chapter 1

Introduction

An open quantum system is a general term that describes a quantum system interacting with an effective non-interacting macroscopic environment. If the quantum system comprises only a small number of degrees of freedom, it is also called a quantum impurity system or dissipative quantum system depending on the nature of the system or the perspective of the study. Fig. 1.1 shows two scenarios of open quantum systems: the magnetic impurity inside a metal which causes the Kondo effect [5, 47] and the experimental setup of a quantum bit which suffers from environmental noises [17]. Many theoretical models have been proposed to describe open quantum systems, such as the Kondo model, the Anderson impurity model [5] and some models we will study in this thesis, namely the resonant level model [33, 52], the spin-boson model [52] and the telegraph noise model [67]. These open quantum models play an important role in many branches of modern physics like condensed matter physics, quantum information theory, quantum optics, quantum measurement theory, etc.

There are numerous theoretical techniques to study these open quantum models such as perturbation theory, density matrix theory, Green's functions etc. However due to the many-particle nature of the full system, except for a few of the simplest models, analytical methods often involve approximations which either restrict their usage to some special cases or may make it difficult to differentiate features from the model itself or from the approximations made during the analytical study. Therefore a generally applicable, first principle numerical method is desirable as an alternative to the analytical approach to understand the diverse problems commonly encountered in the research area of nanotechnology and quantum information. This is the direction I will try to explore in my thesis.

The earliest and still one of the most important numerical methods to study open quantum systems is the numerical renormalization group method (NRG) [110, 48]. It was originally invented in the 1970s by Kenneth Wilson to solve the Kondo problem which could not be achieved by any analytical methods such as perturbation theory at that time. After its initial success on the Kondo problem, NRG has been extended to solve other open quantum models and problems other than thermal dynamic properties [19, 43, 101, 63, 28, 18, 48, 9, 37, 4, 10, 59] and has been a standard tool for many decades in this field.

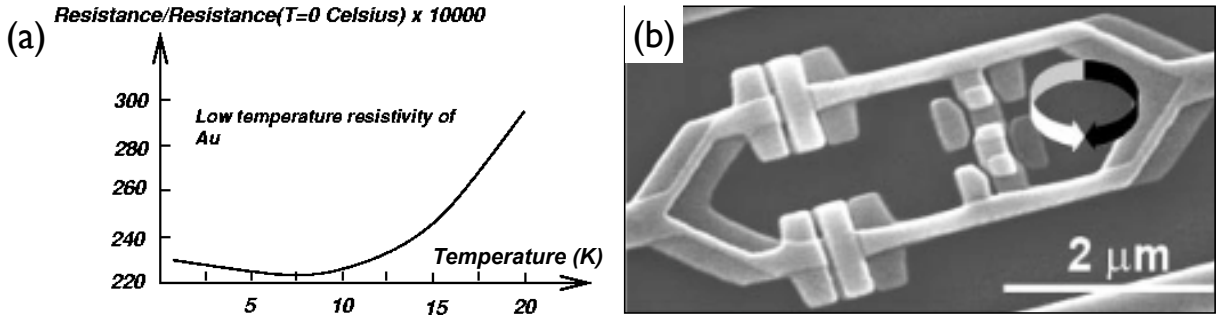

Figure 1.1: Two scenarios of open quantum systems. (a) The coupling between the magnetic impurity with the conduction electrons inside a metal causes the Kondo effect which appears macroscopically as a logarithmic increase of resistivity at very low temperature. The figure is from Ref. [22]. (b) Scanning micrography of a superconducting flux qubit. Similar experimental realizations of qubits all suffer from the destructive noise of the surrounding environment. The image is from Ref. [17].

In addition to its numerical nature, NRG also provides an extremely systematic approach to quantum impurity models through its innovative approach based on renormalization. Finite-size spectra as well as fixed-point spectra can be used to drive effective models which are again amenable to analytical work.

Even though NRG has been successfully extended to study many other open quantum systems it is not applicable to one-dimensional real-space lattices. Twenty years after the invention of NRG Steven R. White, who was a PhD student of Wilson, proposed a new numerical method – the density matrix renormalization group method (DMRG), to solve one-dimensional lattice systems [105, 103]. Though inspired by NRG, the idea behind the new method was very different. In fact as was only made clear later, unlike NRG it is not a true renormalization group method, but a variational one instead.

DMRG quickly became popular because of its unprecedented accuracy to study the ground state and low lying states of 1D quantum lattice systems [109, 84, 71, 8, 68, 41, 58]. It has also been extended in two directions: one is to dynamical properties [34, 72, 49, 40] and thermodynamical properties [13, 99]; the other is to generalize DMRG to other systems such as 2D or 3D systems [62, 106, 36, 114], to momentum space [113, 61], or quantum chemistry systems [26, 104, 21]. The performance of DMRG in these systems is not as good as on simple real space 1D lattice systems. However, it serves as an inspiring starting point of a new generation of algorithms to deal with more complicated systems, collectively know as tensor network methods [56, 94, 92, 93, 53, 32, 88, 44, 78, 25, 54, 42, 115]. The field it has opened is one of the most exciting areas in condensed matter physics, quantum information and even high energy physics [73, 86].

During the development of DMRG people also got a deeper understanding of why DMRG works so well with some systems (1D nearest neighbor lattice system) but becomes expensive when dealing with other systems (2D/3D system). The breakthrough was the realization that the wave function DMRG generates has the representation of a matrix product state, and that DMRG can be reformulated as a variational matrix product state

method (VMPS) [66, 89, 91, 69].

VMPS has a clear mathematical structure. While DMRG experts use VMPS language to understand some theoretical aspects of DMRG, physicist in the field of quantum information also started using MPS framework to study problems related to the classical simulation of quantum systems. There "classical simulation" means to use a classical computer to simulate, or in the language of computational complexity theory, to use a deterministic Turing machine to simulate. By studying the classical simulation of quantum systems, one can understand better the advantage of quantum computers [27, 23]. If there exist algorithms for classical computers to simulate any quantum systems efficiently (in polynomial time), then the advantage of quantum computers over classical computers would vanish and the computational complexity class BQP (bounded error quantum polynomial time) would be equal to P (polynomial time). Otherwise, those quantum systems turn out to be difficult to simulate on classical computers, and would be good candidates to harness the power of quantum computing.

In 2003, Vidal proposed the time-evolving block decimation algorithm (TEBD) [94], and proved that any quantum system with a limited amount of entanglement could be simulated with TEBD. Therefore, one should choose those highly entangled quantum systems to build a quantum computer. Interestingly on the other hand, lots of systems in condensed matter physics are only weakly entangled according to TEBD's standard, which means TEBD could be used to simulate the dynamics of such systems. Daley et al. and White et al. incorporated TEBD into DMRG, and proposed the adaptive time-dependent DMRG (t-DMRG) [20, 108] to simulate the real-time dynamics of quantum 1D system with nearest neighbor interactions.

MPS is not only a bridge between quantum information and condensed matter physics, it also connects two powerful numerical methods mentioned above: NRG and DMRG. In 2005, Weichselbaum et al. showed that NRG can also be formulated in the MPS representation and it shares lots in common with DMRG in this language [100]. This is a key argument why we could use DMRG/VMPS to study quantum impurity models.

A key benefit to use DMRG to study open quantum systems is that we can directly apply t-DMRG and other existing DMRG techniques. NRG has also been extended to study the dynamics of open quantum systems (TD-NRG) [3], but it is only restricted to the quenched type time-dependence of the Hamiltonian while t-DMRG can treat the Hamiltonian with arbitrary time-dependence. The second benefit is that DMRG/VMPS uses a variational approach to calculate the ground state, which makes it more flexible to explore new ideas. More specifically, in this thesis only the use of DMRG/VMPS allowed us to employ non-logarithmic discretization and the optimal boson basis, which were crucial to the success of the projects presented in this thesis.

Overall, this thesis is organized as follows. In chapter 2 I will review the numerical methods used in this thesis: NRG, DMRG, t-DMRG and VMPS. As a benchmark, we then first study an exactly solvable time-dependent open quantum system problem with DMRG in Chap. 3. It is a resonant level model with a Landau-Zener type time-dependent external potential. In Chap. 4, we introduce an optimal boson basis to VMPS, which allows us to effectively handle up to 10^{10} local boson states, and use VMPS to study the phase

diagram and critical behavior of one- and two-bath spin-boson models. In Chap. 5, we study several dynamical properties of the quantum telegraph noise model. In the appendices, I will briefly introduce two open source programs we developed for the projects in this thesis.

Chapter 2

DMRG, NRG and VMPS

In this chapter I will review the numerical methods used in this thesis. As there are already extensive reviews for each of these methods, the main purpose of this chapter is not to cover every aspect of these methods, but rather to concentrate on the most essential and relevant parts to make the thesis self-contained. I will first introduce NRG, DMRG and t-DMRG separately and then introduce the matrix product state representation to connect NRG and DMRG within the framework of VMPS.

2.1 NRG

The Numerical Renormalization Group (NRG) [110, 48, 9] is a very general method to study open quantum systems. There is no restriction on the nature of the impurity (system). Regarding the bath (environment), it can be fermions, bosons or both; it can be one-, two- or three-dimensional. NRG does have one restriction on the bath: it should consist of effective noninteracting particles. For a noninteracting bath, the real dimension is irrelevant because its degree of freedom can be integrated out and all the relevant bath properties to the impurity are captured in the spectral function of the bath $\Delta(\omega)$, with the energy ω its only remaining parameter. NRG coarse-grains the continuous bath spectral function logarithmically, maps this onto a semi-infinite chain of sites with exponentially decaying coupling, then diagonalizes the Hamiltonian of the whole system iteratively. In the following I will explain these steps in detail.

2.1.1 Logarithmic discretization

To calculate the influence of the bath on the impurity in a numerical setting, the continuous bath spectral function is first discretized logarithmically. There are two main reasons for using logarithmic discretization in NRG. First, the relevant energy scale can be exponentially low, and logarithmic discretization makes sure that small energy scales can be reached within a small number of energy intervals. If one uses linear discretization, one would need an impractically long chain. The second reason is that logarithmic dis-

cretization (with large enough logarithmic discretization parameter Λ defined in Eq. 2.1) separates consecutive energy scales, so that discarded high-energy states of a given NRG iteration have limited effect on the following iterations.

Suppose the band-width of the bath is $[-1, 1]$, in other words the bath spectral function is defined in the interval $[-1, 1]$ and all energies are taken in units of the bandwidth. According to logarithmic discretization, we discretize the band in energy space by consecutive intervals determined by the following positions

$$\omega_n = \pm\Lambda^{-n}, n = 1, 2, \cdots, \tag{2.1}$$

where $\Lambda > 1$ is a dimensionless parameter, called the logarithmic discretization parameter. The width of each energy level $\theta_n = |\omega_{n+1} - \omega_n|$ is $1/\Lambda$ of the previous level, so we get finer and finer energy resolution when we approach $\omega = 0$. The spectral function of a bosonic bath is defined in $[0, \omega_c]$. Usually the cut-off frequency ω_c is set to 1 as the unit of energy. For the bosonic bath we only use the positive part of Eq. (2.1).

After cutting the continuous spectral function into slices we calculate the effect of each of them on the impurity. Clearly, using a single energy level to represent a whole energy slice, is a crude approximation for high energy slices as they cover a wide range of energies. Nevertheless it is still used because NRG is traditionally a tool to study the low temperature properties where the most important part of the bath spectral function lies at small energies around $\omega = 0$. When one does need to represent the high energy part of the band properly, one can resort to the "z-averaging" technique to improve this approximation [98]. The basic idea behind this is a shift in the discretization of Eq. (2.1), with an additional parameter z,

$$\omega_n = \pm\Lambda^{-n+z}, n = 1, 2, \cdots, z \in [0, 1). \tag{2.2}$$

For each choice of z we cut the band at different positions, and when $z = 0$ it is equivalent to Eq. (2.1). One can chose several equality spaced z values and calculate the problem separately, after which an averaging of the independent results is performed to reduce the artifacts caused by the inaccurate representation of the band especially at the high energy part. Thus the method got the name "z-averaging".

As the most important part of this thesis refers to the spin-boson model, I will use it as an example in the following. The original continuous Hamiltonian is

$$H = H_{loc} + \int_0^1 \omega a_\omega^\dagger a_\omega d\omega + \frac{\sigma_z}{2} \int_0^1 [\rho(\omega)]^{1/2} \lambda(\omega)(a_\omega + a_\omega^\dagger) d\omega, \tag{2.3}$$

where

$$H_{loc} = -\Delta\frac{\sigma_x}{2} + \epsilon\frac{\sigma_z}{2} \tag{2.4}$$

describes the local Hamiltonian. $\epsilon(\Delta)$ stands for the Zeeman splitting in an actual magnetic field in the z- (x-) direction. $\rho(\omega)$ is the density of states, and $\lambda(\omega)$ describes the coupling strength between the spin and the bath. By definition, its relation to the bath spectral function is

$$J(\omega) = \pi\rho(\omega)[\lambda(\omega)]^2. \tag{2.5}$$

The boson operators $a_\omega^\dagger$ and a_ω satisfies commutation relation

$$[a_\omega, a_{\omega'}^\dagger] = \delta(\omega - \omega'). \tag{2.6}$$

The effect of the bath on the impurity is fully determined by the spectral function $J(\omega)$. Therefore, we are free to choose an arbitrary form of density of states $\rho(\omega)$ and the corresponding $\lambda(\omega)$ as long as Eq. (2.5) is satisfied. The integrals in the Hamiltonian. (2.3) can be carried out in each energy intervals. With this, we transform the Hamiltonian (2.3) into the discretized form

$$H = H_{loc} + \sum_{n=0}^{\infty} \xi_n a_n^\dagger a_n + \frac{\sigma_z}{2\sqrt{\pi}} \sum_{n=0}^{\infty} \gamma_n (a_n + a_n^\dagger), \tag{2.7}$$

with

$$\gamma_n^2 = \int_{\Lambda^{-(n+1)}}^{\Lambda^{-n}} J(\omega) d\omega, \tag{2.8}$$

$$\xi_n = \gamma_n^{-2} \int_{\Lambda^{-(n+1)}}^{\Lambda^{-n}} J(\omega)\omega d\omega. \tag{2.9}$$

The standard parametrization of the bosonic bath spectral function is

$$J(\omega) = 2\pi\alpha\omega_c^{1-s}\omega^s. \tag{2.10}$$

The cut-off frequency is set as the unit of energy $\omega_c = 1$. Substituting Eq. (2.10) into Eq. (2.8) and Eq. (2.9) we get:

$$\xi_n = \frac{s+1}{s+2}\frac{1-\Lambda^{-(s+2)}}{1-\Lambda^{-(s+1)}}\Lambda^{-n}, \tag{2.11}$$

$$\gamma_n^2 = \frac{2\pi\alpha}{s+1}(1-\Lambda^{-(s+1)})\Lambda^{-n(s+1)}. \tag{2.12}$$

2.1.2 Iterative diagonalization of the Wilson chain

The discretized Hamiltonian Eq. (2.7) is of a "star structure": the spin couples to boson modes of all energy scales. To adapt to later renormalization step, it is necessary to transform this star structure into a half-infinite chain form with only nearest neighbor interaction. This form is called the "Wilson chain" in NRG.

The star Hamiltonian is in a bilinear form. Therefore we can express the bath and coupling part as a matrix with $\vec{a} = (\sigma_z, a_0, a_1, a_2, \cdots)^T$ as the base vector. Then the star Hamiltonian is

$$H = H_{loc} + \vec{a}^T A \vec{a}, \tag{2.13}$$

where the matrix A is

$$A = \begin{pmatrix} 0 & \frac{\gamma_0}{2\sqrt{\pi}} & \frac{\gamma_1}{2\sqrt{\pi}} & \frac{\gamma_2}{2\sqrt{\pi}} & \cdots \\ \frac{\gamma_0}{2\sqrt{\pi}} & \xi_0 & 0 & 0 & \\ \frac{\gamma_1}{2\sqrt{\pi}} & 0 & \xi_1 & 0 & \\ \frac{\gamma_2}{2\sqrt{\pi}} & 0 & 0 & \xi_2 & \\ \vdots & & & & \ddots \end{pmatrix}. \tag{2.14}$$

In its matrix form, transforming the Hamiltonian to the Wilson chain mathematically means to tri-diagonalize A. We can use standard numerical routines like Lanczos for tri-diagonalizing a Hermitian matrix. Suppose the resulting tri-diagonal matrix is B, with the corresponding unitary transformation matrix U, then with

$$A = U^\dagger B U, \tag{2.15}$$

we can define a new set of boson operators

$$\vec{b} \equiv (\sigma_z, b_0, b_1, b_2, \cdots) = U\vec{a}, \tag{2.16}$$

and express the Hamiltonian with the new boson sites as

$$\begin{aligned} H &= H_{loc} + \vec{a}^T A \vec{a} \\ &= H_{loc} + \vec{a}^T U^\dagger B U \vec{a} \\ &= H_{loc} + \vec{b}^T B \vec{b}, \end{aligned} \tag{2.17}$$

or explicitly as

$$H = H_{loc} + \sqrt{\frac{\eta_0}{\pi}}\frac{\sigma_z}{2}(b_0 + b_0^\dagger) + \sum_{n=0}^{\infty} \epsilon_n b_n^\dagger b_n + \sum_{n=0}^{\infty} t_n (b_n^\dagger b_{n+1} + b_{n+1}^\dagger b_n), \tag{2.18}$$

where $\eta_0 = \int J(\omega) d\omega$ encodes the overall coupling between impurity and bath. The boson energies ϵ_n and the hopping amplitudes t_n decay exponentially as Λ^{-n}. This is characteristic of the bosonic bath. For a fermionic bath, the decay rate is $\Lambda^{-n/2}$. Eq. (2.18) is the Wilson chain Hamiltonian. It is a semi-infinite 1D lattice with the impurity at one end. The energy scale decays exponentially as one proceeds along the chain. The Wilson chain is consistent with the fundamental idea behind the renormalization group that the various energy scales are only locally coupled. More specifically, a physical process happening at a certain energy scale only directly couples to its nearby energy scales which also implies that the process at any energy scales may or may not have effect on a process at an energy scale far away from it (relevant and irrelevant operators are related with this phenomenon) [110]. Also note that the transformation from the star geometry to the Wilson chain is numerically exact.

The basic process of NRG is as follows: we can view the Wilson chain Hamiltonian Eq. (2.18) as the limit of a series of Hamiltonians with better and better description of smaller and smaller energy scales

$$H = \lim_{N\to\infty} \Lambda^{-N} H_N. \tag{2.19}$$

Λ^{-N} is the renormalization rescaling factor, and it makes the energy spectrum of successive Hamiltonians comparable. The recurrence relation of the Hamiltonian series is

$$H_{N+1} = \Lambda H_N + \Lambda^{N+1}[\epsilon_{N+1} b_{N+1}^\dagger b_{N+1} + t_N (b_N^\dagger b_{N+1} + b_{N+1}^\dagger b_N)]. \tag{2.20}$$

The first Hamiltonian includes the impurity and the first site of the Wilson chain

$$H_0 = H_{loc} + \sqrt{\frac{\eta_0}{\pi}} \frac{\sigma_z}{2} (b_0 + b_0^\dagger) + \epsilon_0 b_0^\dagger b_0. \tag{2.21}$$

Fig. 2.1 illustrates the iterative diagonalization of NRG. Starting from $N = 0$, we add one site to form the Hamiltonian H_{N+1} according to Eq. (2.20). It includes rescaling H_N by a factor of Λ (for fermionic bath $\Lambda^{1/2}$) and the coupling term to the new added site by a factor of Λ^{N+1} (for fermionic bath $\Lambda^{(N+1)/2}$). Then we diagonalize the Hamiltonian H_{N+1} and find all eigenstates. The lowest D states are used as the new combined basis. When the original dimension of H_{N+1} is smaller than D, all eigenstates will be used as the new basis of the new block. Given the basis of H_N, and the basis of the added site are $|\tilde{s}\rangle$ and $|n\rangle$ respectively, then the new combined states $|s\rangle$ are given by

$$|s\rangle = \sum_{\tilde{s}n} A_{s,(\tilde{s}n)} |\tilde{s}\rangle |n\rangle. \tag{2.22}$$

$(\tilde{s}n)$ is the combined column index. Each row of $A_{s,(\tilde{s}n)}$ represents a kept eigenstate. Afterwards, we express all the operators of H_{N+1} in the new basis $|s\rangle$. If we do not use the truncated new basis, the dimension of the basis will increase exponentially as one adds more and more sites, thus restricting the calculation to very short Wilson chains. The above process is shown in Fig. (2.2).

Connecting the energy levels of each iteration we will obtain the renormalization flow of energy levels. This kind of diagram is called the flow diagram. The pattern of the flow diagram is normally changing through iterations before it finally settles at a fixed pattern which is called the stable fixed point. There can be some iteration regimes in which the pattern of the spectrum in the flow diagram is not changing, and such regimes are called fixed points. The iterative diagonalization of NRG normally stops at the fixed point with the lowest energy scale, that is the stable fixed point. Analyzing the flow diagram and fixed point spectra can reveal much of the underlying physics of the system. As such, it constitutes an important NRG technique.

The truncation scheme used by NRG is the essential reason why the logarithmic discretization should be used. If we want the discarded states to have little effect on later

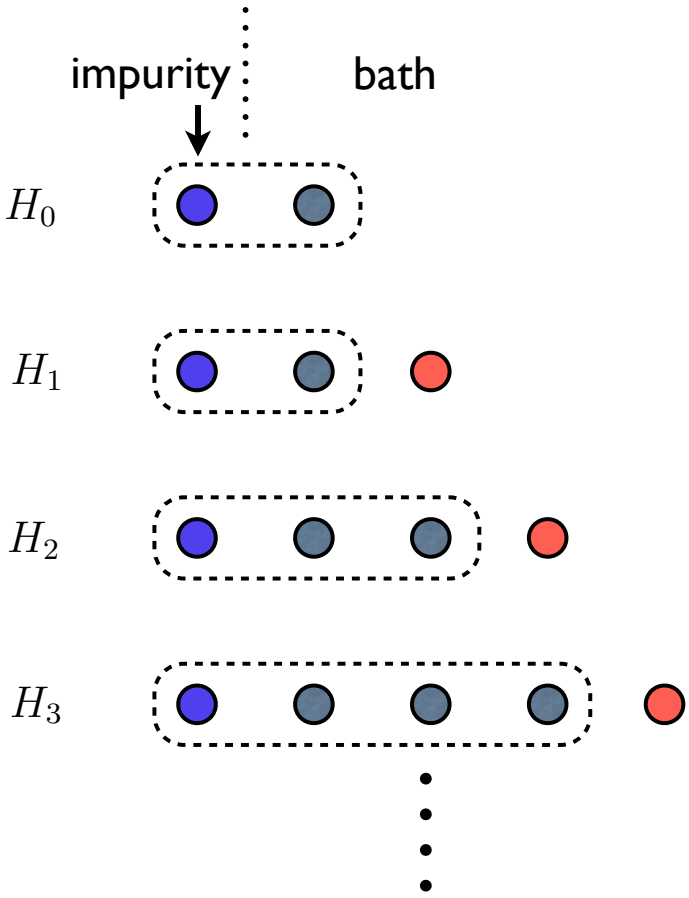

Figure 2.1: Illustration of NRG iterative diagonalization. The new Hamiltonian H_{N+1} is formed by adding another site at the end of the previous Wilson chain. The dimension of the effective basis needs to be truncated given a finite amount of numerical resources.

iterations, we would want the energy scale of those discarded states to be separated far away enough from the energy scales of later iterations. For this reason the logarithmic discretization parameter Λ should not be too small, and usually one should use $\Lambda \geq 2$ in NRG. I will also discuss in detail later that when we replace the NRG truncation scheme by DMRG truncation scheme the logarithmic discretization is no longer required.

2.2 Traditional DMRG

In this section I present the basic procedure of DMRG in its original form described by White [105, 103]. It is a very accurate numerical method to study the ground state of 1D quantum lattice systems. I use it to calculate the ground state of an engineered Hamiltonian as the starting state for time-evolution when I study the dissipative Landau-Zener problem (Chap. 3) and the quantum telegraph noise model (Chap. 5). When I study the spin-boson model in Chap. 4 I use its modern formulation – variational matrix product state method

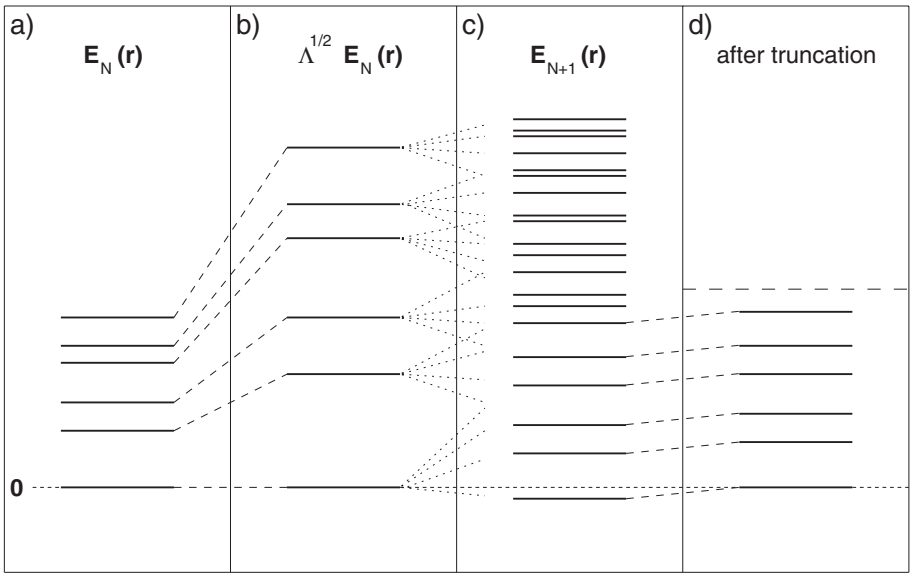

Figure 2.2: The spectrum of the NRG Hamiltonians during rescaling, shifting and truncating. (Figure taken from Ref. [9]). (a) The energy spectrum of H_N, $E_N(r)$, with ground state energy set to 0. r labels the energy levels. (b) For a fermionic bath, H_N is rescaled by a factor of $\Lambda^{1/2}$ (for boson by the factor Λ) before adding a new site. (c) The added site causes splitting of the original energy levels. The new ground state is below 0 after the splitting of levels. (d) Truncate the high energy states and keep the lowest D eigenstates only. We use the new ground state as the energy reference and shift all levels up which concludes one iteration.

(VMPS), which I will introduce in the last section of this chapter.

The traditional DMRG method includes two parts: the infinite DMRG (iDMRG) which is used to grow a 1D lattice and finite DMRG (fDMRG) which is used to variationally optimize the ground state of the resulting lattice from iDMRG. iDMRG can be used alone to study an infinite system by analyzing its asymptotic properties when approaching infinite system size. fDMRG is used to study a finite 1D system. fDMRG in its original formulation requires iDMRG to build a chain with certain length L for subsequent optimization.

2.2.1 Infinite DMRG

From a retrospective view one can clearly see the influence of NRG on DMRG. NRG starts from one system site and adds environmental sites one by one until convergence is reached. Similarly iDMRG starts with two sites: one called the "system" block and another called the "environment" block as shown in the first row of Fig. 2.3. The two-blocks are equivalent as they are just two normal sites in a homogeneous 1D quantum chain, for which DMRG is usually used. The 1D chain is not an open quantum system where there is distinction between system and environment. Here, the name "system" and "environment" are assigned arbitrarily. Neither block is more special than the other.

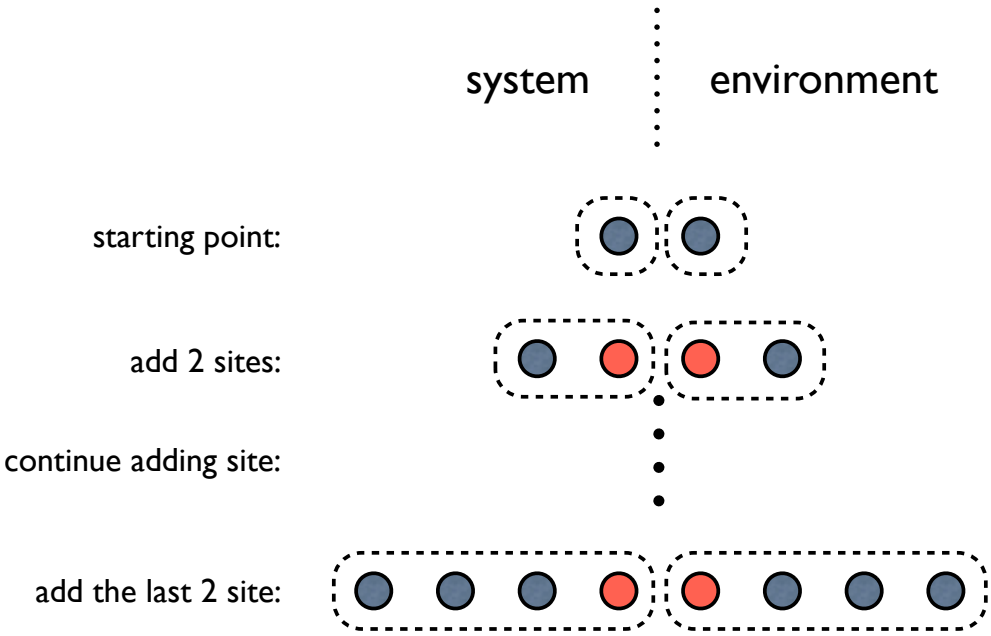

Figure 2.3: Illustration of the basic steps of infinite DMRG. Red sites are newly added sites at the current step. After adding a new site, the block basis is truncated according the DMRG criteria to prevent the dimension from increasing exponentially.

Similar to NRG, two new sites (shown in red in Fig. 2.3) are added to the two-blocks respectively. The blocks with added sites are called new system block and new environment block. If the basis of the old blocks are $|\tilde{s}\rangle$ and $|\tilde{e}\rangle$ and the basis of a free site is $|n\rangle$ the basis of the new blocks are:

$$\begin{aligned} |s\rangle &= \sum_{n,\tilde{s}} I_{s,(\tilde{s}n)} |\tilde{s}\rangle |n\rangle, \\ |e\rangle &= \sum_{n,\tilde{e}} I_{e,(n\tilde{e})} |n\rangle |\tilde{e}\rangle. \end{aligned} \tag{2.23}$$

Here the symbol I means the identity matrix. $(\tilde{s}n)$ and $(n\tilde{e})$ are combined indices. If the dimension of the old blocks is D and the dimension of the free site basis is d, then the dimension of the new blocks' basis will be expanded to Dd. Adding more and more sites in this way would result in an exponential increase of the dimension of the basis. Therefore a truncation scheme is again necessary to make the method practical.

The truncation criteria, telling which states or linear combination of states in Eqs. (2.23) should be kept, is one big difference between DMRG and NRG. If we use NRG's criteria, that is we keep the D lowest lying eigenstates of the Hamiltonian of the new block, we will not get the desired ground state. The reason is that unlike the Wilson chain in NRG the eigenstates of the subsystem in real space have weak connection with the eigenstates of the whole system. With this in mind it becomes natural that the states to keep should be the "important" states of the subsystem with respect to the overall ground state when

it is embedded in the whole system. In other words, targeting the overall ground state of the system and thus a single state, we should keep the eigenstates of the reduced density matrix of the subsystem corresponding to the biggest eigenvalues. This criteria applies both to the system and the environment block.

The representation of the ground state wave function of whole system (or by the DMRG nomenclature the super block) in terms of of the system and environment block is given by

$$|\psi^G\rangle = \sum_{s,e} \psi^G_{se}|s\rangle|e\rangle, \tag{2.24}$$

where ψ_{se} is a matrix of the size $Dd \times Dd$. Here D is the dimension of the old system and environment, and d is the dimension of newly added sites. The reduced density matrices of the two subsystems would be (I use capital letters to indicate the subsystem and lower case letters to label the basis of the subsystems)

$$\begin{aligned} \rho^S &= Tr_E|\psi\rangle\langle\psi| = \sum_e \psi^*_{se}\psi_{s'e}|s\rangle\langle s'|, \\ \rho^E &= Tr_S|\psi\rangle\langle\psi| = \sum_s \psi^*_{se}\psi_{se'}|e\rangle\langle e'|. \end{aligned} \tag{2.25}$$

Therefore after the new blocks are formed, one should first calculate the ground state of the super block. The Hamiltonian of the super block is of the form

$$H^{sup} = H^S \otimes I^E + I^S \otimes H^E + O^S \otimes O^E. \tag{2.26}$$

where H^S is the Hamiltonian of the system block, I^S is the identity matrix , O^S is an operator of the system block. The last term in Eq. (2.26) usually is a sum of several pairs of operators (e. g. $c^\dagger_i c_{i+1} + H.C.$), but for simplicity here only one pair is assumed. The dimension of the super block Hamiltonian is D^2d^2.

In DMRG we do not expand the super block Hamiltonian explicitly in full because this would be very expensive if all we want is just the ground state (and a few low lying states) of this Hamiltonian. Luckily there are a few sparse matrix diagonalization algorithms such as Lanczos, conjugate gradient or Arnold algorithm which only require a function $\vec{y} = f(\vec{x}) = A\vec{x}$ to be able to calculate the ground state of the matrix A. Therefore all we need is to provide the algorithm the function

$$\begin{aligned} |\phi\rangle &= H^{sup}|\psi\rangle \\ &= \sum_{s,e}(\sum_{s'} H^S_{ss'}\psi_{s'e} + \sum_{e'} \psi_{se'}H^E_{e'e} + \sum_{s',e'} O^S_{ss'}\psi_{s'e'}O^E_{e'e})|s\rangle|e\rangle \\ &= \sum_{s,e} \phi_{se}|s\rangle|e\rangle. \end{aligned} \tag{2.27}$$

$H^S_{ss'}$ is the matrix element of the system block Hamiltonian in the $|s\rangle$ basis

$$H^S = \sum_{s,s'} H^S_{ss'}|s\rangle\langle s'|, \tag{2.28}$$

and other matrices are defined similarly.

After we obtain the ground state wave function, we can calculate the reduced density matrices according to Eqs. (2.25). Then we find D eigenvectors with the greatest eigenvalues for both ρ^S and ρ^E and use these vectors for the following renormalization transformation

$$\begin{aligned} |s\rangle &= \sum_{n,s} A^S_{s,(\tilde{s}n)} |\tilde{s}\rangle |n\rangle, \\ |e\rangle &= \sum_{n,e} A^E_{e,(n\tilde{e})} |n\rangle |\tilde{e}\rangle. \end{aligned} \tag{2.29}$$

This transformation then replaces Eq. (2.23), and thus truncates the full state space dimension Dd back down to D. All operators shall be represented in the new system and environment basis. This finishes one iDMRG step and we can add another two sites until we reach the targeted chain length.

When we use DMRG to study a finite chain of length L, the ground state from iDMRG is usually not accurate enough. fDMRG can be used to further minimize the ground state's energy variationally.

2.2.2 Finite DMRG

As illustrated in Fig. 2.4, we start fDMRG based on the final step of iDMRG. The old block information was stored during the previous iDMRG steps and is now read by fDMRG before the first step, which is the same as the last step of iDMRG–we add two site, diagonalize the super block Hamiltonian except we only renormalize the environment block. In the second step we use the new environment block we got from step one and read the stored system block with chain length $L/2-2$ as the old blocks and then add two sites to them respectively and the rest is just like the previous step until we reach the left most site of the chain. Then we change the sweeping direction while the role of the system and environment are switched. We can sweep back and forth a few times until the results converged. Normally a few sweeps (< 10) are sufficient.

2.2.3 Calculation of physical quantities

The ground state energy can be obtained directly from super block diagonalization. Other physical quantities can be calculated as the expectation values of their operator with respect to the ground state. In the DMRG calculation the operator of the desired physical quantity will be renormalized together with other operators like the block Hamiltonian and it is represented in the same basis as the wave function. For example, if the site lies in the system block the operator of the physical quantity A will be represented as

$$A = \sum_{s,s'} A_{ss'} |s\rangle\langle s'|. \tag{2.30}$$

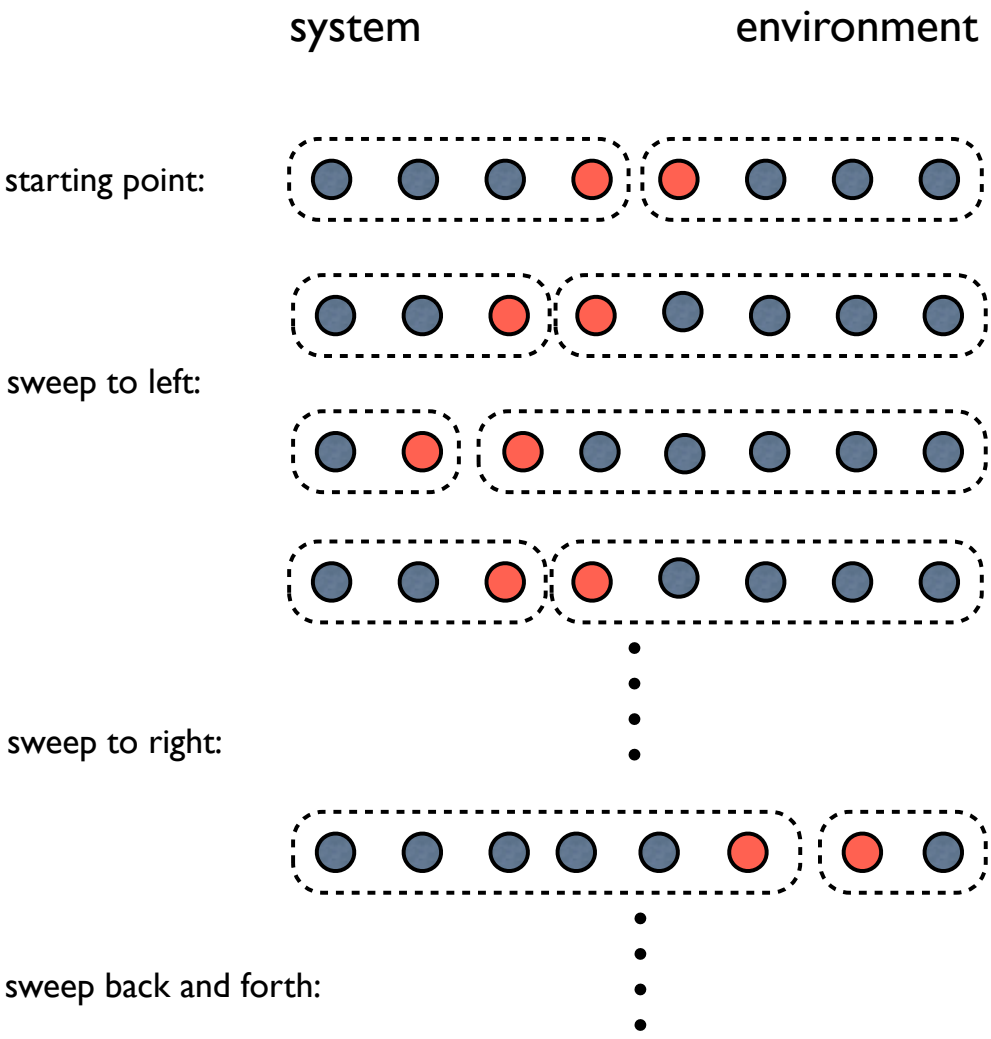

Figure 2.4: Illustration of the sweep of finite fDMRG. Unlike iDMRG where we add one site to each block, in fDMRG we increase the length of one block at the expense of the other thus keeping the total length fixed. One can sweep back and forth a few times to achieve better precision.

The physical quantity can be simply calculated as

$$\begin{aligned}\langle A\rangle &= \langle\psi^G|A|\psi^G\rangle \\ &= \sum_{s,s',e,e'} \psi^*_{s'e'} A_{ss'} \psi_{se} \langle s', e'|s'\rangle\langle s|s, e\rangle \\ &= \sum_{s,s',e} \psi^*_{s'e} A_{ss'} \psi_{se}. \end{aligned} \tag{2.31}$$

Operators acting one two sites should be treated differently depending whether the two sites lie on the same block or on different blocks. I will not elaborate this in detail as we only use physical quantities associated with a single site in this thesis.

2.3 Time-dependent DMRG

Several different approaches using DMRG to study the dynamics of 1D quantum systems have been proposed. One of the earliest method is static time-dependent DMRG [15, 55, 79]. The method I use is called the adaptive time-dependent DMRG (t-DMRG) invented in 2004 by two separate groups [20, 108] based on TEBD [94]. Compared with previous time-dependent DMRG, it is much faster and also able to handle Hamiltonians with arbitrary time dependence while the previous methods can only treat quench type time-dependent Hamiltonians.

The basic procedure of t-DMRG is to apply the time-evolution operator on the wave function

$$|\psi(t+\tau)\rangle = e^{-iH(t)\tau}|\psi(t)\rangle. \tag{2.32}$$

τ is a small time interval, and $H(t)$ is the time dependent super block Hamiltonian. As explained in the previous section, $H(t)$ is never explicitly calculated for efficiency reasons in iDMRG and fDMRG. In t-DMRG similarly we do not calculate $e^{-iH(t)\tau}$ explicitly.

To apply the time-evolution operator we first use the Suzuki-Trotter decomposition to break $e^{-iH(t)\tau}$ into a product of local operators. The first order Suzuki-Trotter decomposition is

$$\begin{aligned} e^{-iH\tau} &= e^{-iH_{odd}\tau}e^{-iH_{even}\tau} + O(\tau^2) \\ &= e^{-i(H_1+H_3+\cdots)\tau}e^{-i(H_2+H_4+\cdots)\tau} + O(\tau^2) \end{aligned} \tag{2.33}$$

where $H_1, H_2, \cdots$ are the local Hamiltonians acting on the 1st-2nd sites, 2nd-3rd sites, ..., as shown in Fig. 2.5. If there are one-site terms in the Hamiltonian, they can be grouped to either side of the two local Hamiltonians as long as the choice is consistent throughout the whole chain. As the local Hamiltonians with the same parity index commute with each other (H_1 commutes with H_3, H_2 commutes with H_4, etc.) Eq. (2.33) can be further written as

$$\begin{aligned} e^{-iH\tau} &= e^{-iH_1\tau}e^{-iH_3\tau}\cdots e^{-iH_2\tau}e^{-iH_4\tau}\cdots + O(\tau^2) \\ &\equiv U_1U_3\cdots U_2U_4\cdots + O(\tau^2) \end{aligned} \tag{2.34}$$

The local time-evolution operators U_k can be easily evaluated. To apply them on the wave function we need to transform the wave function from the "two-block" setup as in Eq. (2.24) to a "four-block" setup as illustrated in Fig. 2.6, combining the relations of Eq. (2.23) into the new basis the wave function is

$$|\psi\rangle = \sum_{s,n_1,n_2,e} \psi_{s,n_1,n_2,e}|s\rangle|n_1\rangle|n_2\rangle|e\rangle. \tag{2.35}$$

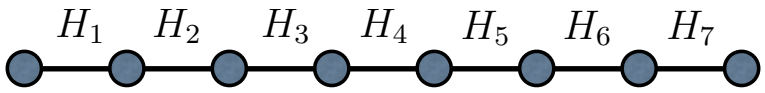

Figure 2.5: Local Hamiltonians in the definition of Trotter decomposition.

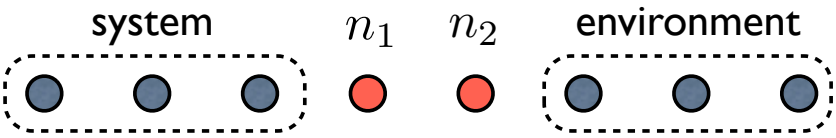

Figure 2.6: Illustration of the four-block setup of the super block basis. The super block wave function is transformed from the original two-block setup used in iDMRG and fDMRG into this four-block setup so that one can apply local operators easily. White's original version of DMRG [105, 103] also adopted the four-block setup to save memory usage.

Indeed in White's original version of DMRG [105, 103] he used the four-block setup for iDMRG and fDMRG too because it is more memory efficient than the two-block setup I used. Nowadays the PC memory is several orders of magnitude larger than those when DMRG was first invented in the early 90s, and the bottle neck is no longer the memory but how fast one can compute $H|\psi\rangle$. In the two-block setup the wave function is always stored as a matrix which make it much easier to use some highly optimized linear algebra libraries (MKL, ATLAS) to speed up the $H|\psi\rangle$ calculation.

The local time-evolution operator is represented in the local basis $|n_1\rangle|n_2\rangle$. Therefore after we transformed the wave function into the four-block setup, U is applied on the wave function as

$$\begin{aligned} |\psi'\rangle &= U|\psi\rangle \\ &= \sum_{n_1' n_2' n_1 n_1, s, e} U_{n_1 n_2, n_1' n_2'} \psi_{s, n_1', n_2', e} |s\rangle |n_1\rangle |n_2\rangle |e\rangle \end{aligned} \tag{2.36}$$

Next we need to shift the basis two sites to the left (right). The procedure is similar to fDMRG except we do not need to calculate the ground state of the super block Hamiltonian. Instead we base on $|\psi'\rangle$ to evaluate the reduced density matrix of the left (right) block and find the renormalization transformation matrices A^S (A^E) as in Eq. (2.29). This basis shifting technique is called "wave function prediction" by Steven White [106] because it was first used as a guess of the next step wave function in fDMRG to speed up convergence (the speed up is significant therefore should always be used). In this way one can apply all the even bond U during a sweep from left to right, and then all the odd bond U when sweeping back to the left side as illustrated in Fig. 2.7(a). This finishes one time step τ. Unlike previous time-dependent DMRG where a basis to incorporate wave functions of all time steps is required, t-DMRG always updates the basis to adapt to the current wave function. This saves lots of resources and is the reason behind the name "*adaptive* time-dependent DMRG".

In my program I used second order Trotter-Suzuki decomposition, as it is a simple modification to the first order decomposition but has a smaller decomposition error [85, 108].

$$e^{-i\tau(A+B)} = e^{-i\tau/2A} e^{-i\tau B} e^{-i\tau/2A} \tag{2.37}$$

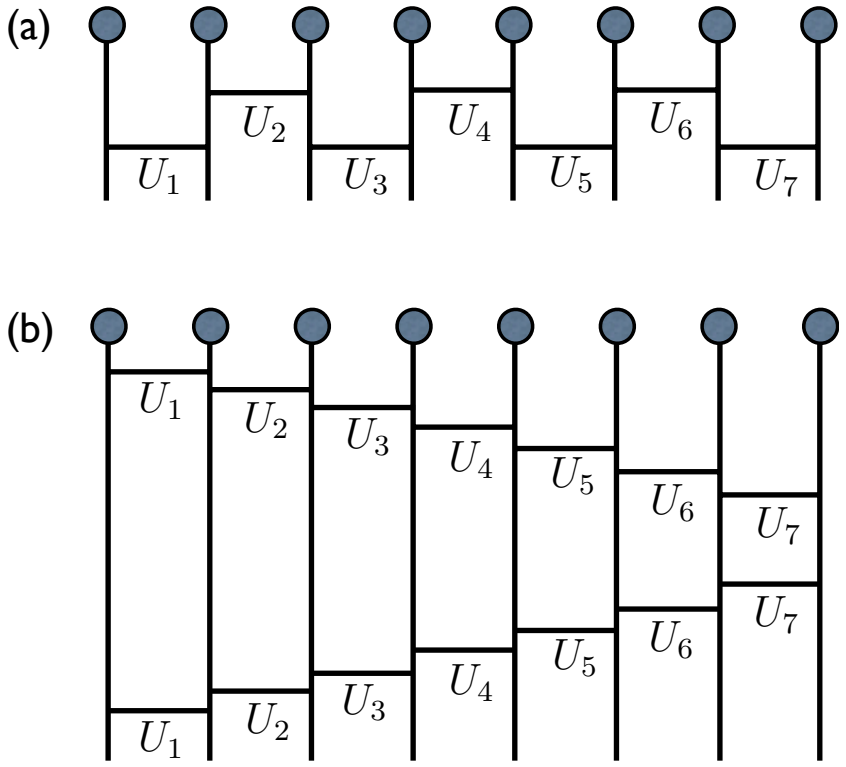

Figure 2.7: Illustration of the application of time-evolution operator decomposed on the wave function. Local time-evolution operators closer to the lattice are applied first. (a) The first order Trotter-Suzuki decomposition; (b) the second order Trotter-Suzuki decomposition. Note that definition of the local time-evolution operators are different in (a) and (b).

where A and B are non-commute operators. If we let $A = H_1$ and $B = H_2 + H3 + \cdots$ and use Eq. 2.37 iteratively in this manner we will have

$$\begin{aligned} e^{-iH\tau} &= e^{-i\frac{\tau}{2}H_1} e^{-i\frac{\tau}{2}H_2} \cdots e^{-i\frac{\tau}{2}H_L} e^{-i\frac{\tau}{2}H_L} \cdots e^{-i\frac{\tau}{2}H_2} e^{-i\frac{\tau}{2}H_1} + O(\tau^3) \\ &\equiv U_1 U_2 \cdots U_L U_L \cdots U_2 U_1 + O(\tau^3) \end{aligned} \tag{2.38}$$

Note here the local time-evolving operators are defined differently as in the second order. They are half time-step operators because one needs to apply them twice to evolve one time step. The application of one time-step τ evolution operator with the second order decomposition on the wave function is illustrated in Fig. 2.7(b). That is when we sweep from left to right we apply U_1 to U_L one by one, then we sweep back and apply all the local U operators in the opposite order.

2.4 VMPS

In 1995, Östlund and Rommer first pointed out that DMRG is a variational method based on a matrix product state [66]. Variational matrix product state method (VMPS) is the

reformulation of density matrix renormalization group method in matrix product state representation [57, 38, 69]. VMPS and DMRG are mathematically equivalent, however VMPS is more concise and easier to deal with both theoretically and numerically. In this thesis, I use VMPS instead of the original DMRG method to study the spin-boson model in Chap. 4.

2.4.1 Matrix product state

The basis transformation of NRG (Eq. (2.22)) and DMRG (Eq. (2.25)) are of the same form, except that we form the transformation A matrix with different criteria. It is straightforward to verify that by iteratively using Eq. (2.22) or Eq. (2.25) we can write the wave function in the following form

$$|\psi\rangle = \sum_{\{n_k\}} \sum_{\alpha,\beta,\gamma,\cdots,\mu,\nu} A^1_{\alpha n_1} A^2_{\alpha\beta n_2} A^3_{\beta\gamma n_3} \cdots A^{L-1}_{\mu\nu n_{L-1}} A^L_{\nu n_L} |n_1, n_2, n_3, \cdots, n_{L-1}, n_L\rangle. \tag{2.39}$$

The coefficients of the wave function are products of matrices, therefore this is called a matrix product state (MPS). MPS is the common mathematical structure underlying NRG and DMRG, therefore it connects the seemingly quite independent methods. MPS enables us to bring some NRG techniques to DMRG and to use DMRG to study open quantum systems [100, 74]. This will be explained in detail in later chapters. In this section, I will only review some general properties of MPS.

If the dimension of the A matrices D is large enough, we can represent any state in MPS form. However, in practice the reason why we want to represent a quantum wave function in the MPS form is that MPS can represent certain kinds of quantum states either exactly or to a very good approximation with relatively small D ($D \lesssim 100$ for example in this thesis). The criteria for such kind of quantum states is that the entanglement of the state is relatively small. Fortunately, this is the case for ground states of 1D quantum lattices due to the area law [69, 24]. However, for excited states when dealing with real-time evolution in true out-of equilibrium, entanglement also can grow, such that t-DMRG is sometimes limited to relatively short time windows.

We can use von Neumann entropy as a measure of the entanglement between two blocks of the whole system. The von Neumann entropy is defined as

$$S = -Tr\rho \ln \rho = -\sum_r \eta_r \ln \eta_r, \tag{2.40}$$

with ρ the reduced density matrix and η_r its eigenvalues satisfying $\sum_r \eta_r = 1$. Therefore von Neumann entropy will reach its maximum value when all η_r are equal. If we calculate the reduced density matrix from MPS, the dimension of ρ is the same as for the A matrices. The upper bound for the block entropy is thus

$$S_{max} = -\sum_{r=1}^{D} \frac{1}{D} \ln \frac{1}{D} = \ln D. \tag{2.41}$$

Eq. (2.41) implies that the amount of entanglement along the MPS can increase only logarithmically with the matrix dimension D.

An MPS as in Eq. (2.39) contains lots of indices, and thus is a complex representation of a simple many-body wave function. Therefore, it is sometimes more convenient to illustrate the underlying structure pictorially with a diagram like the one shown in Fig. 2.8.

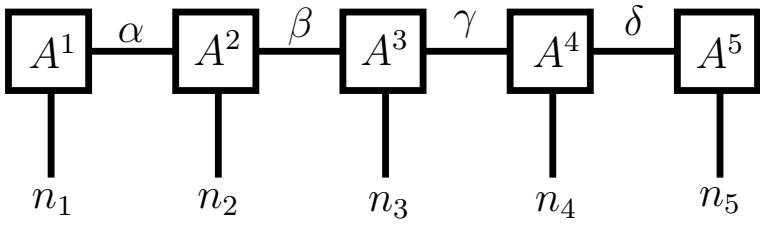

Figure 2.8: Schematic diagram of a MPS wave function with 5 sites. Squares represent the A-tensors of the MPS, and lines represent their indices. Lines connecting two squares are contracted indices (that is they are summed over). Open lines connect to the basis, and in this diagram they connect to the local basis n_k.

Now I will use the 5 sites MPS to show how to calculate (1) an overlap, (2) the action of an operator, and (3) the expectation value with MPS with the help of the schematic diagram. The overlap of two wave functions is calculated by contracting the corresponding local indices of the two wave functions

$$\begin{aligned}
\langle\psi_B|\psi_A\rangle &= \sum_{\{n'_k\}}\sum_{\alpha',\beta',\gamma',\delta'} (B^1_{\alpha' n'_1} B^2_{\alpha'\beta' n'_2} B^3_{\beta'\gamma' n'_3} B^4_{\gamma'\delta' n'_4} B^5_{\delta' n'_5})^* \langle n'_1, n'_2, n'_3, n'_4, n'_5| \\
&\quad \times \sum_{\{n_k\}}\sum_{\alpha,\beta,\gamma,\delta} A^1_{\alpha n_1} A^2_{\alpha\beta n_2} A^3_{\beta\gamma n_3} A^4_{\gamma\delta n_4} A^5_{\delta n_5} |n_1, n_2, n_3, n_4, n_5\rangle \\
&= \sum_{\{n_k\}}\sum_{\alpha,\beta,\gamma,\delta}\sum_{\alpha',\beta',\gamma',\delta'} (B^1_{\alpha' n_1} B^2_{\alpha'\beta' n_2} B^3_{\beta'\gamma' n_3} B^4_{\gamma'\delta' n_4} B^5_{\delta' n_5})^* A^1_{\alpha n_1} A^2_{\alpha\beta n_2} A^3_{\beta\gamma n_3} A^4_{\gamma\delta n_4} A^5_{\delta n_5}.
\end{aligned}$$

The corresponding diagram for overlap is shown in Fig. 2.9

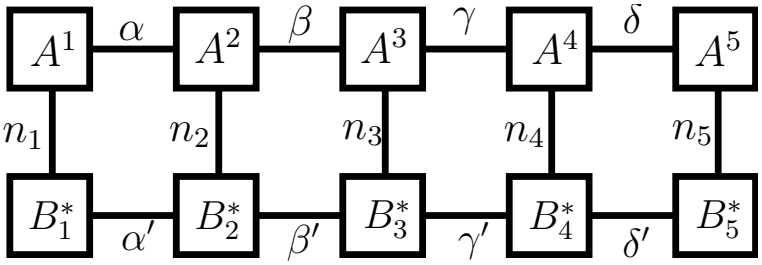

Figure 2.9: Schematic diagram of the overlap of two MPS wave functions $|\psi_A\rangle$ and $|\psi_B\rangle$. Complex conjugate tensors will be used when the local indices are pointing up like the B tensors in this diagram. Overlap is calculated by contracting all local indices of two wave functions.

In DMRG if one wants to apply a local operator on a wave function, one typically needs to perform a partial DMRG sweep to the location where the operator acts. In MPS representation the application of the operator is straight forward since the wave function is expressed in the native local basis. For example the application of a two site operator

$$U_{23} \equiv \sum_{(n_2'n_3'),(n_2n_3)} U_{(n_2'n_3'),(n_2n_3)} |n_2', n_3'\rangle\langle n_2, n_3| \tag{2.42}$$

is

$$\begin{aligned} U_{23}|\psi\rangle &= \sum_{\{n_k\}} \sum_{\alpha,\beta,\gamma,\delta} A^1_{\alpha n_1} A^2_{\alpha\beta n_2} A^3_{\beta\gamma n_3} A^4_{\gamma\delta n_4} A^5_{\delta n_5} |n_1, n_2, n_3, n_4, n_5\rangle \\ &= \sum_{\{n_k\}} \sum_{\alpha,\beta,\delta} A^1_{\alpha n_1} \sum_{n_2',n_3',\gamma,} (U_{(n_2n_3),(n_2'n_3')} A^2_{\alpha\beta n_2'} A^3_{\beta\gamma n_3'}) A^4_{\gamma\delta n_4} A^5_{\delta n_5} |n_1, n_2, n_3, n_4, n_5\rangle \\ &= \sum_{\{n_k\}} \sum_{\alpha,\beta,\delta} A^1_{\alpha n_1} C^{23}_{\alpha\gamma n_2 n_3} A^4_{\gamma\delta n_4} A^5_{\delta n_5} |n_1, n_2, n_3, n_4, n_5\rangle. \end{aligned}$$

Immediately after the operation, this results in the enlarged tensor $C^{23}_{\alpha\gamma n_2 n_3}$. To restore the original MPS form, we need to perform singular value decomposition (SVD) on the tensor $C^{23}_{\alpha\gamma n_2 n_3}$

$$\begin{aligned} C^{23}_{\alpha\gamma n_2 n_3} &= C^{23}_{(\alpha n_2),(\gamma n_3)} \\ &= \sum_\beta \tilde{\tilde{A}}^2_{(\alpha n_2)\beta} \lambda_\beta \tilde{A}^3_{\beta(\gamma n_3)} \\ &= \sum_\beta \tilde{A}^2_{(\alpha n_2)\beta} \tilde{A}^3_{\beta(\gamma n_3)} \\ &= \sum_\beta \tilde{A}^2_{\alpha\beta n_2} \tilde{A}^3_{\beta\gamma n_3}. \end{aligned} \tag{2.43}$$

In the first line of Eq. (2.43) we reorder and combine the indices of tensor C^{23} and transform it to a matrix. λ_β in the second line is the singular value vector and it is absorbed into $\tilde{A}^2_{(\alpha n_2)\beta}$ in the third line. In the last line indices are resorted to their MPS order. Fig. 2.10 illustrates this process with a schematic diagram.

The calculation of an expectation value can be reduced to the combination of the previous two operations. However an alternative way is to directly contract all indices. This way also enables us to easily calculate the expectation value of a operator acting simultaneously on any number of sites like the example shown in Fig. 2.11.

2.4.2 Variational matrix product state

Variational matrix product state (VMPS) can be considered as a generalization of finite DMRG. The finite DMRG introduced in the previous section is equivalent to two-site

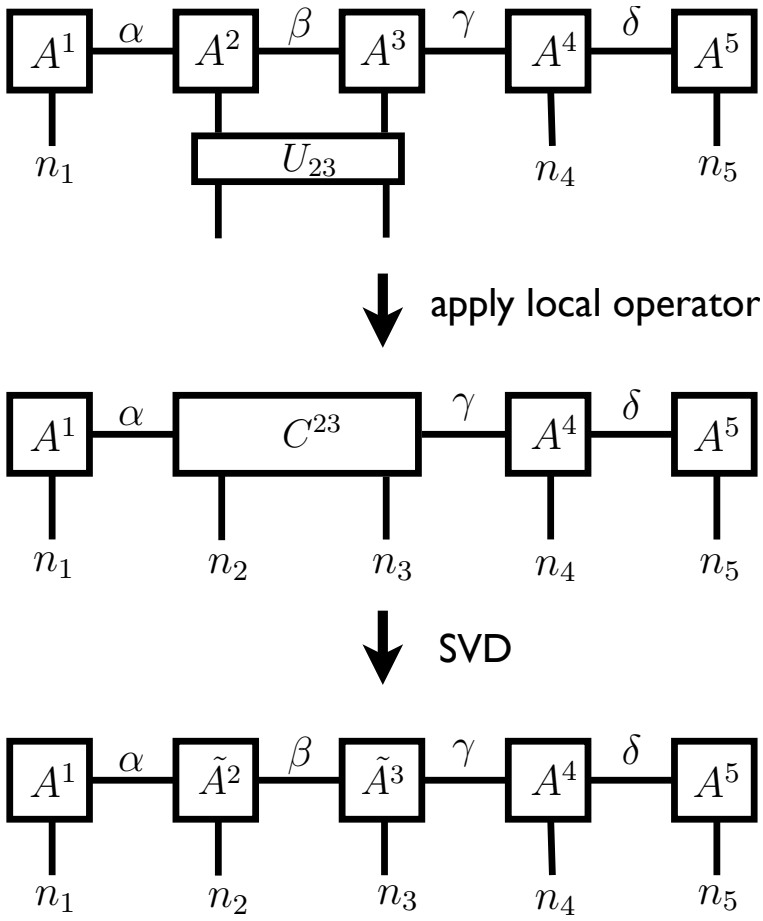

Figure 2.10: Schematic diagram of applying a local operator U^{23} on a MPS. First contract the local indices on site 2 and 3 with the indices of U^{23}. This will result a big tensor C^{23}. Then a singular value decomposition is performed to restore the original MPS structure. [See Eq. (2.43)]

VMPS, which means we optimize two sites each time of the optimization. Here we introduce the single site VMPS, which only optimizes one site at each optimization step. Compared with two-site VMPS, it converges slower but the dimension of the optimization problem is smaller than two site VMPS. This is a big advantage when dealing with bosonic systems.

Simply speaking VMPS minimizes the energy by variationally optimizing the A matrices sequentially at a time. At the center of the VMPS calculation is the optimization problem at one site. All the subsystem operators and Hamiltonians are transformed into the effective basis of the current site. The wave function in the local basis is just the A matrix

$$|\psi\rangle = \sum_{\alpha\beta n_k} A^k_{\alpha\beta n_k} |\alpha, \beta, n_k\rangle. \tag{2.44}$$

The local optimization problem is to find the $A^k_{\alpha\beta n_k}$ ($|\psi\rangle$) which minimizes the quantity $\langle\psi|H|\psi\rangle/\langle\psi|\psi\rangle$. This $|\psi\rangle$ is by definition the ground state of H. Therefore, the variational

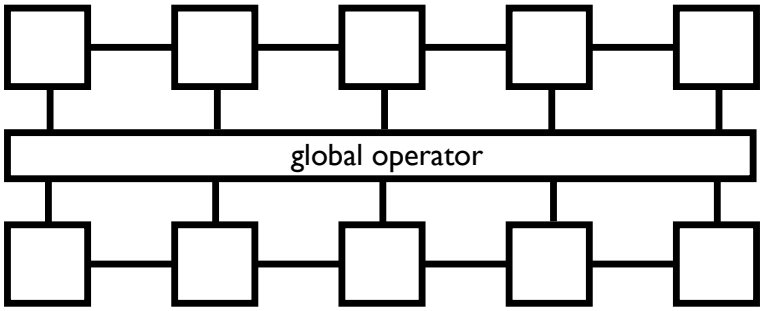

Figure 2.11: Schematic diagram of calculating the expectation value of a global operator by simply contracting all local indices with the corresponding indices of the global operator. I omit all the labels for simplicity.

problem is transformed into an eigenvalue problem. Similar to DMRG, H is a big sparse matrix, and we cannot and do not have to explicitly expand it into full matrix form. To solve the eigenvalue problem, all we need is to provide the sparse diagonalization algorithm the function $|\phi\rangle = H|\psi\rangle$. In the $|\alpha, \beta, n_k\rangle$ basis the Hamiltonian reads

$$\begin{aligned} H &= H_L \otimes I_k \otimes I_R + I_L \otimes I_k \otimes H_R + I_L \otimes H_k \otimes I_R \\ &\quad + O_L \otimes O_k \otimes I_R + I_L \otimes O_k \otimes O_R, \end{aligned} \tag{2.45}$$

with H_L and H_R the Hamiltonian of the block on the left and right side of the current site k respectively. I_L, I_R, I_k are identity matrices in their respective spaces. In Eq. (2.45), H_k is the single site term in the Hamiltonian that acts on site k. For example, in the Hamiltonian Eq. (2.18), this is the onsite potential $\epsilon_k b_k^\dagger b_k$. O_L and O_R are operators on site $k-1$ and $k+1$ in left and right block basis. O_k is site operator on site k. The last two terms in the Hamiltonian (2.45) normally consist of several such terms summed over. For simplicity, only a single term is shown. Furthermore, it is assumed throughout that the Hamiltonian is short ranged in that it only contains local and nearest-neighbor terms. Take the Hamiltonian (2.18) for example, with the current site the last two terms in the Hamiltonian (2.45) account for the following four terms: $t_{k-1} b_{k-1}^\dagger b_k$, $t_{k-1} b_k^\dagger b_{k-1}$, $t_k b_k^\dagger b_{k+1}$ and $t_k b_{k+1}^\dagger b_k$. Therefore $H|\psi\rangle$ can be split into five parts which are illustrated using the schematic diagram in Fig. (2.12).

O_k and H_k are local operators that act within the Fock space of site k. Their matrix representations thus are elementary and known from the setup. However the calculation of the block operators and Hamiltonians O_L, H_L, etc. requires more effort. Let us first take a close look of the operator O_R for example. In the $|\alpha, \beta, n_k\rangle$ basis it is

$$O_R = \sum_{\beta,\beta'} O^R_{\beta\beta'} |\beta\rangle\langle\beta'|. \tag{2.46}$$

Actually O_R is just the local operator of site $k+1$

$$O_{k+1} = \sum_{n_{k+1}, n'_{k+1}} O^{k+1}_{n_{k+1}, n'_{k+1}} |n_{k+1}\rangle\langle n'_{k+1}|, \tag{2.47}$$

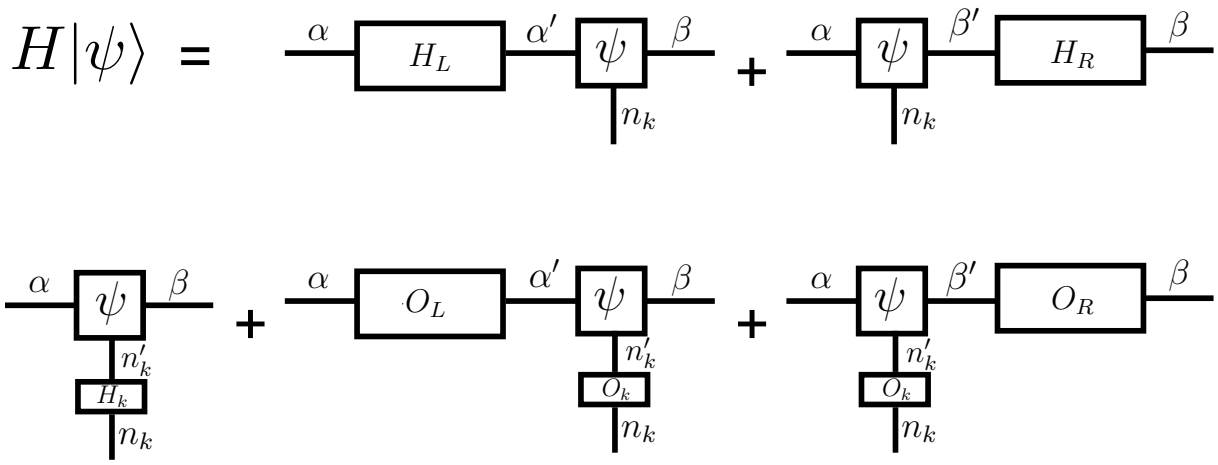

Figure 2.12: Schematic diagram of the five terms in Eq. (2.45) required to compute $H|\psi\rangle$.

and is transformed into the $|\beta\rangle$ basis according to the basis transformation

$$|\beta\rangle = \sum_{\gamma, n_{k+1}} A^{k+1}_{\beta\gamma n_{k+1}} |\gamma, n_{k+1}\rangle. \tag{2.48}$$

The $A^{k+1}_{\beta\gamma n_{k+1}}$ in this formula is in its "right orthogonal" form which means

$$\sum_{\gamma, n_{k+1}} (A^{k+1}_{\beta'\gamma n_{k+1}})^* A^{k+1}_{\beta\gamma n_{k+1}} = \delta_{\beta'\beta} \tag{2.49}$$

Any matrix A^k in MPS (except the leftmost one) can be right-orthonormalized by a singular value decomposition. The resulting right matrix from SVD is used as the new A^k and the left matrix and singular values are absorbed into A^{k-1}. "Left-orthonormalized" A^k can be calculated in the same way.

Successively applying such basis transformation as Eq. (2.48) we can represent $|\beta\rangle$ with the only local basis and the transformation of O_{k+1} to O_R is illustrated in Fig. 2.13(a). If the MPS is in its canonical form, that is all matrices have been right-orthonormalized, then (a) reduces to (b). Therefore the calculation of the matrix elements O_{k+1} simply requires

$$O^R_{\beta\beta'} = \sum_{\gamma, n'_{k+1}, n_{k+1}} (A^{k+1}_{\beta\gamma n'_{k+1}})^* O^{k+1}_{n_{k+1} n'_{k+1}} A^{k+1}_{\beta'\gamma n_{k+1}}. \tag{2.50}$$

The block Hamiltonians H_L and H_R are calculated iteratively. I take H_R (at site k) for example, and the iterative relation is

$$H_R = I_{k+1} \otimes H'_R + H_{k+1} \otimes I'_R + O_{k+1} \otimes O'_R \tag{2.51}$$

where H'_R is the H_R at site $k+1$, same for I'_R and O'_R. The formula is illustrated in Fig. 2.14. O'_R is obtained in the same way as shown in Fig. 2.13. H_R is evaluated using Eq. (2.51) iteratively from the rightmost site, where H'_R and O'_R are both 0. All the H_R and O_R at each site are stored for later use.

The procedure of VMPS I used can be summarized as follows

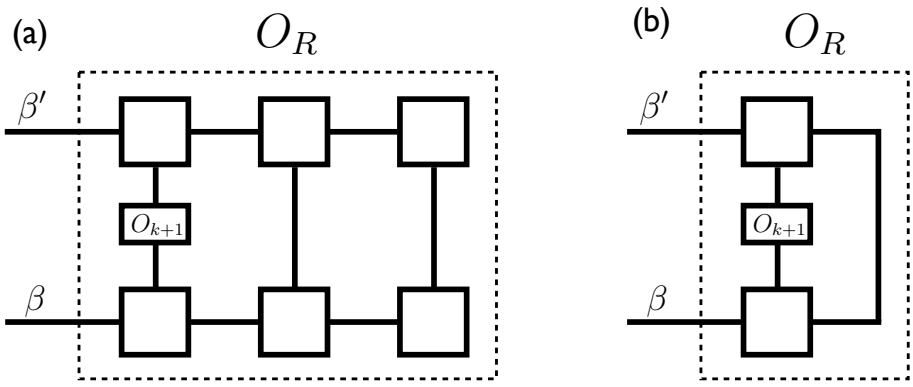

Figure 2.13: Transforming the local operator into the right block basis. The whole structure inside the dashed line is O_R. Because all matrices shown in this plot are assumed to be right-orthonormalized (a) can be reduced to (b).

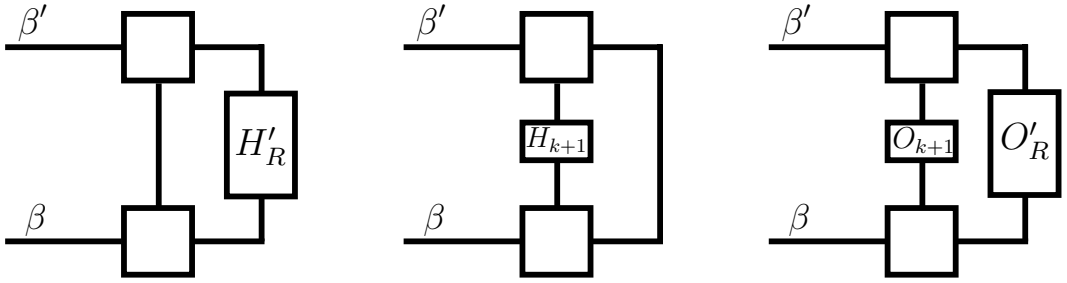

Figure 2.14: The three terms in H_R.

1. Generate a random MPS as the starting point.

2. From the right side calculate H_R and O_R at each site and store them for later steps. At the same time the MPS is right-orthonormalized.

3. Optimize the A matrices sequentially at a time from the left side. At the same time calculate and store H_L and O_L at each site.

4. Repeat step 2 and 3 until convergence is reached. Note that I do not optimize the A matrices while sweeping from right to left because I only study the Wilson chain in this thesis. Considering the energy scale decreases from left to right, in the spirit of NRG the optimization should start from the high energy end.

5. Calculate physical quantities or flow diagram.

With this I finished introducing the basic methods I used in this thesis. In the remainder of this thesis, we will adapt and specialize these methods to the models under consideration.

Chapter 3

Landau-Zener problem

3.1 The standard Landau-Zener problem

The standard Landau-Zener problem [50, 117] is a simple time-dependent problem of a two level system. As a highly idealized model it can be used to describe numerous dynamical processes in different contexts like molecular collisions [16], nano-systems [87, 102, 77], Bose-Einstein condensates [112] and quantum information processing [6, 39, 65, 82]. The time-dependent Hamiltonian is

$$H(t) = \begin{pmatrix} \frac{vt}{2} & \Delta \\ \Delta & -\frac{vt}{2} \end{pmatrix}, \tag{3.1}$$

with t the time, v the speed of level crossing and Δ is the coupling matrix element. For convenience I assume that the two level system consists of a spin. Using Pauli matrices, the Hamiltonian (3.1) becomes

$$H(t) = \frac{vt}{2}\sigma_z + \frac{\Delta}{2}\sigma_x. \tag{3.2}$$

At $t = -\infty$ the system is assumed to be in spin up state $|\uparrow\rangle$. If v is slow enough so that we can consider the LZ process as an adiabatic process then at $t = +\infty$ the system will still be in the $|\uparrow\rangle$ state. Beyond the adiabatic limit, there will be some probability for the spin to flip especially around $t = 0$ when the energy splitting is small. Therefore, at $t = +\infty$ the spin state will be a superposition of $|\downarrow\rangle$ and $|\uparrow\rangle$. The exact calculation of the transition probability is not trivial, but the result is very simple:

$$P = \exp(-\frac{\pi\Delta^2}{2v}). \tag{3.3}$$

In a more realistic scenario the two level system will be in contact with an environment. The large number of degrees of freedom in the environment makes the Landau-Zener process difficult to study analytically. In our paper included as the next section, we show how to combine NRG and tDMRG to study such a typical time-dependent problem of open quantum system from a numerical point of view.

3.2 Publication: DMRG study of a quantum impurity model with Landau-Zener time-dependent Hamiltonian

Density matrix renormalization group study of a quantum impurity model with Landau-Zener time-dependent Hamiltonian

Cheng Guo,[1,2] Andreas Weichselbaum,[1] Stefan Kehrein,[1] Tao Xiang,[3,2] and Jan von Delft[1]
[1]*Physics Department, Arnold Sommerfeld Center for Theoretical Physics, D-80333 München, Germany and Center for NanoScience, Ludwig-Maximilians-Universität München, D-80333 München, Germany*
[2]*Institute of Theoretical Physics, Chinese Academy of Sciences, P.O. Box 2735, Beijing 100080, China*
[3]*Institute of Physics, Chinese Academy of Sciences, P.O. Box 603, Beijing 100080, China*
(Received 17 November 2008; revised manuscript received 3 February 2009; published 30 March 2009)

We use the adaptive time-dependent density matrix renormalization group method (t-DMRG) to study the nonequilibrium dynamics of a benchmark quantum impurity system which has a time-dependent Hamiltonian. This model is a resonant-level model, obtained by a mapping from a certain Ohmic spin-boson model describing the dissipative Landau-Zener transition. We map the resonant-level model onto a Wilson chain, then calculate the time-dependent occupation $n_d(t)$ of the resonant level. We compare t-DMRG results with exact results at zero temperature and find very good agreement. We also give a physical interpretation of the numerical results.

DOI: 10.1103/PhysRevB.79.115137 PACS number(s): 03.65.Yz, 74.50.+r, 33.80.Be, 73.21.La

I. INTRODUCTION

Quantum impurity models, describing a discrete degree of freedom coupled to a continuous bath of excitations, arise in many different contexts in condensed-matter physics. In particular, they are relevant for the description of transport through quantum dots and of qubits coupled to a dissipative environment.[1,2] In recent years, there has been increasing interest in studying the real-time dynamics of such models for Hamiltonians $H(t)$ that are explicitly time dependent, as relevant, for example, to describe external manipulations being performed on a qubit. It is thus important to develop reliable numerical tools that are able to deal with such problems under very general conditions.

The most widely used numerical method to study quantum impurity systems is Wilson's numerical renormalization group (NRG).[3] With the recently proposed time-dependent NRG (TD-NRG) (Ref. 4) one can now calculate certain class of time-dependent problems where a sudden perturbation is applied to the impurity at time $t=0$. TD-NRG may very well be accurate for arbitrary long time. However, up to now, TD-NRG is not capable of dealing with a Hamiltonian $H(t)$ with a time dependence more general than a single abrupt change in model parameters at $t=0$. We will show in this paper that the adaptive time-dependent density matrix renormalization group method (t-DMRG) is a promising candidate for treating a general time-dependent Hamiltonian $H(t)$.

The density matrix renormalization group (DMRG) method is traditionally a numerical method to study the low lying states of one-dimensional quantum systems.[5] The recent extension of this method, the adaptive t-DMRG,[6,7] can simulate real-time dynamics of one-dimensional models with time-dependent Hamiltonians as well. t-DMRG has already been used to study problems involving real-time dynamics of one-dimensional quantum systems, for example the far-from-equilibrium states in spin-1/2 chains,[8] dynamics of ultracold bosons in an optical lattice,[9,10] transport through quantum dots,[11] dynamics of quantum phase transition,[12] and demonstration of spin charge separation.[13] These works showed that t-DMRG is a versatile and powerful method to study the real-time dynamics of one-dimensional quantum systems.

The underlying mathematical structures of DMRG and NRG are similar in the matrix product state representation language.[14] Indeed, once a quantum impurity model has been transformed into the form of a Wilson-chain model, it can be treated by DMRG instead of NRG.[14–17] This possibility opens the door toward studying time-dependent quantum impurity models using t-DMRG. In this paper, we take a first step in this direction by using t-DMRG to study a simple, exactly solvable quantum impurity model whose Hamiltonian is a function of time. This model allows us to benchmark the performance of t-DMRG by comparing its results to those of the exact solution.

II. MODEL AND DMRG METHOD

We study the resonant-level model with a time-dependent potential applied to the level. The Hamiltonian is

$$\hat{H}(t) = \epsilon_d(t) d^\dagger d + \sum_k \epsilon_k c_k^\dagger c_k + V \sum_k (d^\dagger c_k + c_k^\dagger d). \qquad (1)$$

$d^\dagger$ creates a spinless fermion on the level (impurity) and $c_k^\dagger$ creates a spinless fermion with momentum k in a conduction band whose density of states is constant between $-D$ and D and zero otherwise, with Fermi energy set equal to 0. The energy of the local band is swept linearly with time, $\epsilon_d(t)=Dvt$, where v is the sweeping rate in units of the half band width D. This model is equivalent to the dissipative Landau-Zener model with a Ohmic boson bath whose spectral function is $J(\omega)=2\pi\alpha\omega$, for $\omega \ll \omega_c$, where ω_c is the high energy cutoff,[18] and the dimensionless strength of dissipation parameter α is henceforth set equal to $\frac{1}{2}$. When α is close but not equal to $\frac{1}{2}$, Hamiltonian (1) contains an additional interaction term proportional to $U(d^\dagger d - \frac{1}{2})(\Sigma_{k,k'} c_k^\dagger c_{k'} - \frac{1}{2})$,[19] but this case will not be considered here.

At time $t_0 \to -\infty$ the local level contains a spinless fermion and the band is half filled. Then, we lift the energy of the

level linearly with time. As the level approaches the band, the probability that the fermion jumps to and from the band will increase, and decrease after the level has passed the band. In this paper we study this problem in detail. In particular, we are interested in the expectation value of the occupation number on the level $n_d(t)$ at time t.

Before using t-DMRG to solve this problem, we need to transform the Hamiltonian to a DMRG-friendly form. This can be realized by using a standard Wilson mapping (originally invented in the context of NRG), which include two steps: logarithmic discretization of the band and converting the Hamiltonian to a hopping form.[20,21] Here, we just give the final result: Hamiltonian (1) is mapped to a semi-infinite Wilson chain

$$\hat{H}(t) = \epsilon_d(t) d^\dagger d + \left(\frac{2\Gamma D}{\pi}\right)^{1/2} (f_0^\dagger d + d^\dagger f_0) + \frac{D}{2}(1+\Lambda^{-1}) \sum_{n=0}^{\infty} \Lambda^{-n/2} \xi_n (f_n^\dagger f_{n+1} + f_{n+1}^\dagger f_n), \quad (2)$$

where $\xi_n = (1-\Lambda^{-n-1})(1-\Lambda^{-2n-1})^{-1/2}(1-\Lambda^{-2n-3})^{-1/2}$. $\Gamma \equiv \pi\rho V^2$ is the hybridization parameter and ρ is the density of states at the Fermi level. $\Lambda > 1$ is a logarithmic discretization parameter, which means we divide the band into discrete energy intervals determined by $\pm\Lambda^{-1}$, $\pm\Lambda^{-2}$, $\pm\Lambda^{-3}$,.... In the limit $\Lambda \to 1$, the discretized spectrum becomes dense throughout the band. The hopping factors in Hamiltonian (2) decrease exponentially so it is sufficient to keep the first L sites to achieve an energy resolution of $\Lambda^{-L/2}$.

The dimensionless parameter $r \equiv 2\Gamma/v$ can be used to define three typical regimes of this problem. They are:

(i) *fast sweep*: $r \ll 1$,

(ii) *intermediate sweep*: $r \simeq 1$, and

(iii) *slow sweep*: $r \gg 1$.

We will examine the performance of DMRG in all these regimes.

The Wilson-chain form of Hamiltonian (2) can now be treated using DMRG. We first use infinite and finite DMRG (Ref. 5) to calculate the ground state of the initial Hamiltonian $\hat{H}(t_0)$ at t_0. This ground state is a very good approximation to the true initial state in the ideal case in which the level would start from $t_0 \to -\infty$ as long as $\epsilon_d(t_0) \ll -|\Gamma|$. In the fast and intermediate sweep regimes, we can choose t_0 so that the $\epsilon_d(t_0) = Dvt_0$ is far below the Fermi surface to satisfy $\epsilon_d(t_0) \ll -|\Gamma|$. In slow sweep regime we can do the same if we use a very large $|t_0|$. However, a more efficient way we adopt is to use a moderate t_0, but set $\epsilon_d(t_0)$ as a very low value (e.g., $-10000D$). After we get the starting state we apply the evolution operator $\mathcal{T} e^{-i\int_{t_0}^{t} \hat{H}(s)ds}$ on the starting state $|\Psi(t_0)\rangle$ to get the state $|\Psi(t)\rangle$ at time t using t-DMRG,

$$|\Psi(t)\rangle = \mathcal{T} e^{-i\int_{t_0}^{t} \hat{H}(s)ds} |\Psi(t_0)\rangle. \quad (3)$$

Here $\mathcal{T}$ is the time-ordering operator and we set $\hbar = 1$ in this paper.

More specifically, we first divide the time interval t into a series of tiny time steps of the length τ. The Hamiltonian is a function of time, but in each tiny time step it can be approximated by a constant, so we have

$$\mathcal{T} e^{-i\int_{t_0}^{t} \hat{H}(s)ds} \simeq e^{-i\tau\hat{H}(t-\tau/2)} \cdots e^{-i\tau\hat{H}(3/2\tau)} e^{-i\tau\hat{H}(\tau/2)}. \quad (4)$$

We chose the value of Hamiltonian in the middle of each interval to represent the Hamiltonian of that interval. At every time step we decompose $e^{-i\hat{H}(s)\tau}$ into local operators using second-order Suzuki-Trotter decomposition, and we get

$$\begin{aligned} e^{-i\hat{H}(s)\tau} &= e^{-i\tau[\hat{H}_{d,0}(s)+\hat{H}_{0,1}+\hat{H}_{1,2}+\cdots+\hat{H}_{L-1,L}]} \\ &= e^{-i(\tau/2)\hat{H}_{d,0}(s)} e^{-i(\tau/2)\hat{H}_{0,1}} e^{-i(\tau/2)\hat{H}_{1,2}} \cdots e^{-i(\tau/2)\hat{H}_{L-1,L}} \\ &\quad \times e^{-i(\tau/2)\hat{H}_{L-1,L}} \cdots e^{-i(\tau/2)\hat{H}_{1,2}} e^{-i(\tau/2)\hat{H}_{0,1}} e^{-i(\tau/2)\hat{H}_{d,0}} \\ &\quad + O(\tau^3), \end{aligned} \quad (5)$$

where

$$\hat{H}_{d,0}(s) = \epsilon_d(s) d^\dagger d + \left(\frac{2\Gamma D}{\pi}\right)^{1/2} (f_0^\dagger d + d^\dagger f_0), \quad (6)$$

and $H_{n,n+1}$ is the hopping term involving site n and $n+1$. The only time-dependent part of the Hamiltonian is the impurity so we only need to update the Suzuki-Trotter term of the impurity and the first site of the Wilson chain $e^{-i(\tau/2)\hat{H}_{d,0}(s)}$ at every time step.

We can also easily extend this method to study finite-temperature dynamics. Instead of using infinite and finite DMRG to find the starting state, we use finite-temperature DMRG (Ref. 22) to get the starting state. Then, one can evolve this purified state using t-DMRG to simulate the real-time dynamics at finite temperature.[23] In this paper, however, we only focus on the zero temperature and noninteracting case.

III. EXACT METHOD

Hamiltonian (2) is of quadratic form so we can write it as

$$\hat{H}(t) = (a_0^\dagger, a_1^\dagger, \ldots, a_{L-1}^\dagger) H(t) (a_0, a_1, \ldots, a_{L-1})^T, \quad (7)$$

where $a_0 \equiv d$ and $a_i \equiv f_{i-1}$. $H(t)$ is a $L \times L$ Hermitian matrix with L being the length of the Wilson chain.

By diagonalizing $H(t_0)$ we get

$$\hat{H}(t_0) = \sum_k E_k \tilde{a}_k^\dagger \tilde{a}_k. \quad (8)$$

The kth single-particle state is

$$|k\rangle = \tilde{a}_k^\dagger |0\rangle = \sum_i u_{ik} a_i^\dagger |0\rangle, \quad (9)$$

where u_{ik} are the eigenvectors of $H(t_0)$, in the sense that $\Sigma_j H(t_0)_{ij} u_{jk} = E_k u_{ik}$.

At t_0 the system is in its ground state, characterized by the single-particle distribution function

$$f(k) = \begin{cases} 0, & E_k > 0 \\ 1, & E_k < 0. \end{cases} \quad (10)$$

The initial density matrix of the whole system is

$$\hat{\rho}(t_0) = \sum_k f(k)|k\rangle\langle k|. \tag{11}$$

The density matrix evolves according to the von Neumann equation

$$i\frac{\partial\hat{\rho}(t)}{\partial t} = [\hat{H}(t), \hat{\rho}(t)]. \tag{12}$$

This equation can easily be solved with an ordinary differential equation solver such as ode45 of MATLAB. Then we can calculate the expectation value of operators, such as $\hat{n}_d(t)$, as

$$n_d(t) = \mathrm{Tr}[\hat{n}_d\hat{\rho}(t)] = \mathrm{Tr}[a_0^\dagger a_0\hat{\rho}(t)]. \tag{13}$$

IV. RESULTS AND PHYSICAL INTERPRETATION

In Fig. 1 we plot both the exact and DMRG results in the three typical parameter regimes at zero temperature, respectively. We use Wilson-chain length $L=160$ and logarithmic discretization parameter $\Lambda=1.08$ for all the three figures. We will discuss the discretization method in more detail in Sec. V. Note that we set $D=1$ in our calculation.

For all three regimes, the DMRG error (shown in Fig. 2 for fast regime) is at worst of order 1×10^{-4} when keeping $\chi=100$ states during DMRG calculation. This error can be further reduced by increasing χ.

Let us now try to understand the results physically. In the fast sweep regime the spinless fermion on the impurity does not have enough time to totally jump into the band, so the occupation on the impurity $n_d(t)$ converges to a finite value as the level is swept through and out of the band. In contrast, in the slow sweep regime the fermion ends up in the band with a very high probability. For comparison we also show the results of an adiabatic sweep in the slow sweep regime in Fig. 1. The adiabatic results are obtained from the thermodynamic average $\mathrm{Tr}[\hat{\rho}_{\epsilon_d(t)}\hat{n}_d]$, where $\hat{\rho}_{\epsilon_d(t)}$ is calculated using Eq. (11) with single-particle states $|k_{\epsilon_d(t)}\rangle$ of the Hamiltonian $H_{\epsilon_d(t)}$. Evidently, the DMRG and exact results agree very well with the adiabatic results.

Another important feature of the results is the oscillation of $n_d(t)$. To understand it, we first study a simplified model, in which we only consider one level in the band and disregard the rest levels for the moment. When there is one spinless fermion in this system the Hamiltonian is

$$H(t) = \begin{pmatrix} E_0(t) & \gamma \\ \gamma & E_1 \end{pmatrix}, \tag{14}$$

This is just the Hamiltonian of the original Landau-Zener problem. We denote the instantaneous two eigenstates as $|+\rangle_t$ and $|-\rangle_t$ with the corresponding eigenenergies $E_\pm(t)=\frac{1}{2}[E_0(t)+E_1\pm\omega(t)]$, where

$$\omega(t) = \sqrt{4\gamma^2 + [E_1 - E_0(t)]^2}. \tag{15}$$

The probability that a state of the form $|\phi(t)\rangle = a|-\rangle_t + b|+\rangle_t$ at time t will still be found in the same state at time $t+\delta t$ is given by

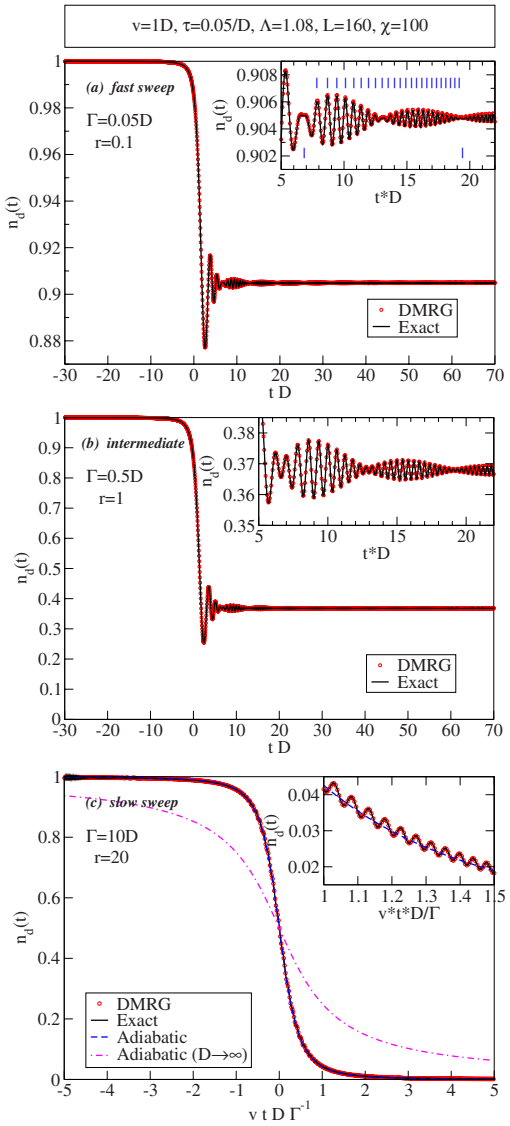

FIG. 1. (Color online) The local occupation number $n_d(t)$ as a function of time, calculated with both exact and DMRG method in the three parameter regimes. At the top, we give the choices made for the following parameters: sweeping speed v, Suzuki-Trotter step τ, logarithmic discretization parameter Λ, Wilson-chain length L, and the number of states kept in DMRG calculation χ. The value of hybridization parameter Γ and the corresponding dimensionless parameter $r\equiv 2\Gamma/v$ are given in each figure, respectively. The insets zoom in on fine details of the curves. (a) The markers in the inset indicate the periods of the oscillations and beats obtained from the simple physical picture discussed in the text [see Eq. (19)]. (c) The dashed lines are the reference results of the adiabatic sweep calculation, and the dash-dotted line is the adiabatic sweep result in infinite band limit, which is simply $n_d(\frac{\epsilon_d}{\Gamma})=\frac{1}{2}-\frac{1}{\pi}\arctan\frac{\epsilon_d}{\Gamma}$.

$$\tilde{P}(t) \equiv |\langle\phi(t)|\phi(t+\delta t)\rangle|^2, \tag{16a}$$

$$= |a|^4 + |b|^4 + 2|ab|^2\cos[\omega(t)\delta t]. \tag{16b}$$

In each time interval, the instantaneous oscillation frequency $\omega(t)$ of $\tilde{P}(t)$ is equal to the instantaneous oscillation

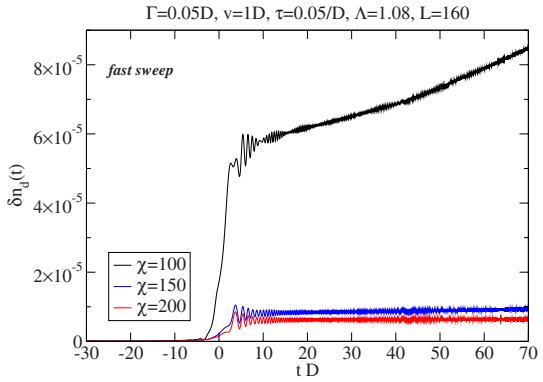

FIG. 2. (Color online) Error of the DMRG results for $\delta n_d(t) \equiv n_d^{\mathrm{DMRG}}(t) - n_d^{\mathrm{Exact}}(t)$ in fast sweep regime when keeping 100, 150, and 200 states.

frequency of $|\langle\phi(t_0)|\phi(t)\rangle|^2$ to the zeroth order in δt. Therefore, the probability for the system initially in a state $|\phi(t_0)\rangle$ to still be found in this state at a later time t,

$$P(t) \equiv |\langle\phi(t_0)|\phi(t)\rangle|^2, \tag{17}$$

will have an oscillating component proportional to $\cos[\int_{t_0}^{t}\omega(s)ds]$.

We now return to the original problem and use the picture described above to roughly estimate the period of the oscillations in the fast sweep regime. In the fast sweep regime according to Pauli exclusion principle the influence of the unoccupied levels of the upper half of the band is dominant. We can neglect the lower half of the band, and add up the contributions of all levels E_1 in the upper half band to the oscillations by integrating the above mentioned cosine term

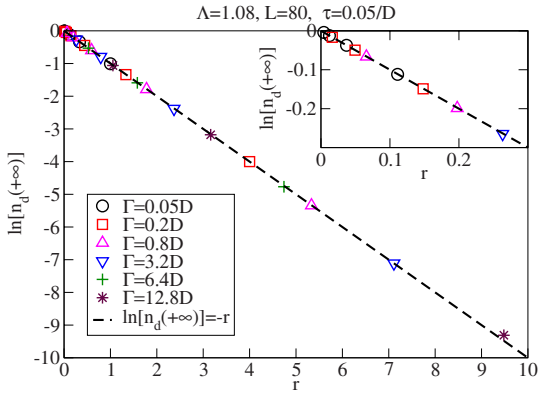

FIG. 3. (Color online) Exact results checking the relation between the final local occupation number $n_d(+\infty)$ and r. Numerically, we approximate $n_d(+\infty)$ by averaging $n_d(t)$ of the last four time steps. The time span we use here is $t \in [-200/D, 200/D]$. To get $n_d(+\infty)$ at different r, we choose six different Γ from a wide parameter regime, and with each Γ six different sweeping speed: $v=0.1D$, $0.3D$, $0.9D$, $2.7D$, $8.1D$, and $24.3D$ are used to calculate $n_d(+\infty)$. We only plot the data for $r<10$ because the accumulated numerical error becomes significant compared to $n_d(+\infty)$ for $r>10$. The dashed line is a reference line of $\ln[n_d(+\infty)]=-r$. The inset zooms in on small r.

TABLE I. The $n_d(+\infty)$ data used in Fig. 3

Γ \ v	0.1D	0.3D	0.9D	2.7D	8.1D	24.3D
0.05D	0.36516	0.71499	0.98419	0.96345	0.98766	0.99587
0.2D	0.01831	0.26199	0.63925	0.86164	0.95155	0.98358
0.8D		0.00480	0.16758	0.55114	0.81984	0.93593
3.2D			0.00081	0.09221	0.45177	0.76732
6.4D				0.00850	0.20404	0.58877
12.8D				0.00009	0.04162	0.34660

over the energies E_1. Therefore the occupation on the resonant level

$$n_d(t) \approx \int_0^D P(t)dE_1 \tag{18}$$

will contain an oscillating contribution proportional to

$$\sin\left[\frac{D}{2}(t-t_0)\right]\cos\left[\frac{1}{2}(vt^2 - Dt + Dt_0 - vt_0^2)\right]. \tag{19}$$

To get the above result, we approximated $\omega(t)$ by $E_1 - vt$, neglecting the term $4\gamma^2 = 4\Gamma D/\pi$ [$\gamma \equiv \sqrt{D\Gamma/\pi}$ is the prefactor of the hybridization term in the energy representation of Hamiltonian (1) (Ref. 20)]. This is a good approximation, except around $t=0$, when the local level is near the middle of the band, and $|E_0 - E_1|$ is not significantly larger than Γ.

The resulting Eq. (19) can be used to understand the nature of the oscillations and beats observed in the fast sweep regime in Fig. 1. The factor $\sin[D(t-t_0)/2]$ is the beat, and the period of the beats is $T_{\mathrm{beats}} = 4\pi/D$. We plot two markers with a separation of $4\pi/D$ under the curve in the inset of Fig. 1(a); they fit the period of the beats very well. The markers above the curve in the insets of Fig. 1(a) are obtained by solving

$$\frac{1}{2}(vt^2 - Dt + Dt_0 - vt_0^2) = 2m\pi + \text{const.}, \tag{20}$$

where m is an integer such that the markers are best aligned with the maxima of the oscillations shown. We can see that the final agreement in position is excellent.

Last but not the least, we examined the dependence of the final local level occupation number $n_d(+\infty)$ on r (shown in Fig. 3, Table I), and find it has the typical Landau-Zener exponential relation,

$$n_d(+\infty) = e^{-r}. \tag{21}$$

This agrees with previous analytical results.[24,25] Note that though $n_d(+\infty)$ only depends on r, the detailed structure of the $n_d(t)$ curve is determined by v and Γ respectively [see Eq. (20) for example].

V. ROLE OF DISCRETIZATION PARAMETER

As in NRG, the value chosen for the discretization parameter can affect the real-time dynamics, if it does not lie suf-

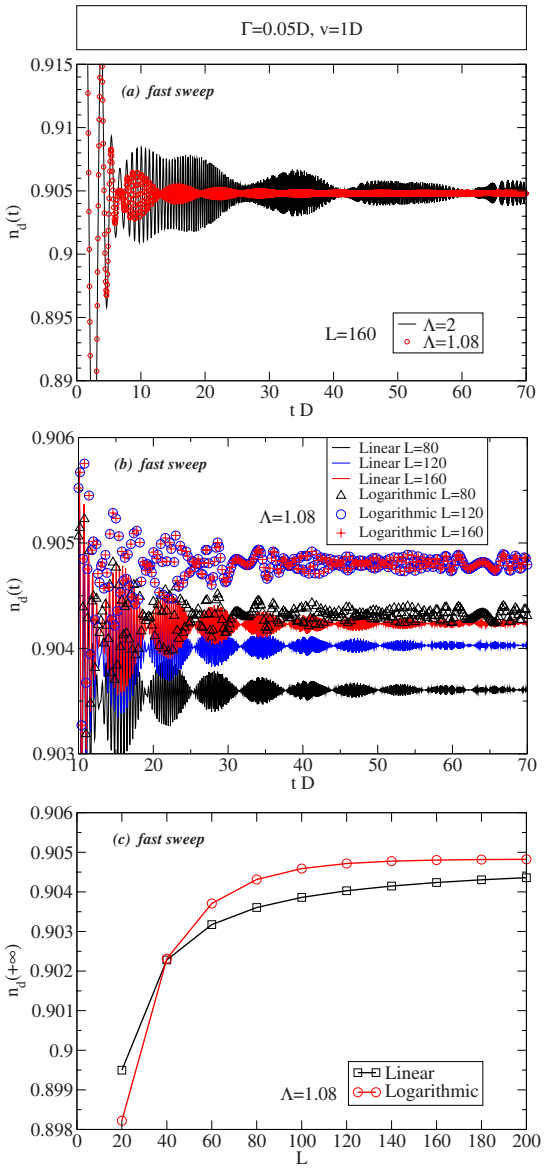

FIG. 4. (Color online) Comparison of the exact results of different logarithmic discretization parameters. Both figures zoom in on fine details. Here we study fast sweep regime as an example. (a) Comparison of the results with different Λ. The large oscillations for $\Lambda=2$ for later times are due to the relatively coarse discretization and hence artificial. [(b) and (c)] Comparison of the converging speed with respect to the Wilson-chain length L of linear and logarithmic discretization method.

ficiently close to 1. Figure 4(a) compares the exact results of $\Lambda=1.08$ and $\Lambda=2$ in fast sweep regime. Note that for $\Lambda=2$, big oscillations in $n_d(t)$ remain long after the transition. These are artificial consequences of the rather coarse discretization scheme, which diminish strongly as Λ is reduced toward 1. Indeed, for $\Lambda=1.08$, most of these oscillations have disappeared. Further reduction in Λ does not change the results significantly anymore. Note that, incidentally, the ability of allowing a logarithmic discretization parameter very close to 1 is a big advantage of DMRG over NRG.

With the physical picture described in Sec. IV, we can also understand why there are artificial oscillations if Λ is big. If we use a big logarithmic discretization parameter, the part of the band far away from the Fermi level is poorly represented by only a few levels, which means that the oscillations from different levels do not average out as well as would have been the case for a true continuum of levels.

We use logarithmic discretization instead of linear discretization because in the problem we studied, the levels near Fermi surface contribute more than levels far away from it, and logarithmic discretization represents the part of band around Fermi surface more efficiently.[27] This is reflected in the convergence of the results with respect to the Wilson-chain length L shown in Fig. 4. As other parameters are the same, the two discretization methods will both converge to the same result when $L\to\infty$. Therefore the faster the result converges the better the method is. We can see from Fig. 4(b) that the difference of $n_d(t)$ between $L=120$ and $L=160$ chains is already negligible for the case of logarithmic discretization while still significant if using linear discretization, which means the results converge more quickly if we use logarithmic discretization. This is even more obvious by comparing the convergence speed of $n_d(+\infty)$ shown in Fig. 4(c).

VI. CONCLUSIONS AND OUTLOOK

By studying a benchmark model we demonstrated that the t-DMRG is a very accurate method to calculate real-time dynamics of quantum impurity system with a time-dependent Hamiltonian. To compare with the exact results, the model we studied here is a noninteracting model, but DMRG can also treat interacting problems similarly.

Though t-DMRG cannot calculate arbitrary long times (in contrast to TD-NRG) it can give reliable results in a relatively long time which we expect to be long enough for numerous practical purposes. For example, in quantum information, where fast quantum processes are more useful, the relevant physics happens in a relatively short time scale, which can be simulated by t-DMRG with a high precision. We thus expect t-DMRG to be a powerful tool to study the real-time dynamics of quantum impurity systems, in particular in the context of modeling the dynamics of damped, driven qubits.

ACKNOWLEDGMENTS

We gratefully acknowledge fruitful discussions with Theresa Hecht and Wolfgang Münder, and Barbara Englert for help in editing the text. We also would like to thank Peng Zhang, Shaojing Qin, Gang Yang, and Qiaoni Chen for helpful discussions. This work was supported by the DFG (SFB 631, SFB-TR12, De-730/3-2). Financial support of the German Excellence Initiative via the Nanosystems Initiative Munich (NIM) is gratefully acknowledged.

[1] Y. Nakamura, Y. A. Pashkin, and J. S. Tsai, Nature (London) **398**, 786 (1999).
[2] I. Chiorescu, Y. Nakamura, C. J. P. M. Harmans, and J. E. Mooij, Science **299**, 1869 (2003).
[3] K. G. Wilson, Rev. Mod. Phys. **47**, 773 (1975).
[4] F. B. Anders and A. Schiller, Phys. Rev. Lett. **95**, 196801 (2005).
[5] S. R. White, Phys. Rev. B **48**, 10345 (1993).
[6] A. J. Daley, C. Kollath, U. Schollwöck, and G. Vidal, J. Stat. Mech.: Theor. Exp. (2004) P04005.
[7] S. R. White and A. E. Feiguin, Phys. Rev. Lett. **93**, 076401 (2004).
[8] D. Gobert, C. Kollath, U. Schollwöck, and G. Schütz, Phys. Rev. E **71**, 036102 (2005).
[9] C. Kollath, U. Schollwöck, J. von Delft, and W. Zwerger, Phys. Rev. A **71**, 053606 (2005).
[10] C. Kollath, A. Iucci, T. Giamarchi, W. Hofstetter, and U. Schollwöck, Phys. Rev. Lett. **97**, 050402 (2006).
[11] K. A. Al-Hassanieh, A. E. Feiguin, J. A. Riera, C. A. Büsser, and E. Dagotto, Phys. Rev. B **73**, 195304 (2006).
[12] F. Pellegrini, S. Montangero, G. E. Santoro, and R. Fazio, Phys. Rev. B **77**, 140404 (2008).
[13] C. Kollath, U. Schollwöck, and W. Zwerger, Phys. Rev. Lett. **95**, 176401 (2005).
[14] A. Weichselbaum, F. Verstraete, U. Schollwöck, J. I. Cirac, and J. von Delft, arXiv:cond-mat/0504305v2 (unpublished).
[15] H. Saberi, A. Weichselbaum, and J. von Delft, Phys. Rev. B **78**, 035124 (2008).
[16] S. Nishimoto and E. Jeckelmann, J. Phys.: Condens. Matter **16**, 613 (2004).
[17] L. G. G. V. Dias da Silva, F. Heidrich-Meisner, A. E. Feiguin, C. A. Busser, G. B. Martins, E. V. Anda, and E. Dagotto, Phys. Rev. B **78**, 195317 (2008).
[18] A. J. Leggett, S. Chakravarty, A. T. Dorsey, P. A. Fisher, A. Garg, and W. Zwerger, Rev. Mod. Phys. **59**, 1 (1987).
[19] F. Guinea, V. Hakim, and A. Muramatsu, Phys. Rev. B **32**, 4410 (1985).
[20] H. R. Krishna-murthy, J. W. Wilkins, and K. G. Wilson, Phys. Rev. B **21**, 1003 (1980).
[21] R. Bulla, T. Costi, and T. Pruschke, Rev. Mod. Phys. **80**, 395 (2008).
[22] A. E. Feiguin and S. R. White, Phys. Rev. B **72**, 220401(R) (2005).
[23] U. Schollwöck, J. Phys. Soc. Jpn. **74** (Suppl.), 246 (2005).
[24] M. Wubs, K. Saito, S. Kohler, P. Hänggi, and Y. Kayanuma, Phys. Rev. Lett. **97**, 200404 (2006).
[25] N. A. Sinitsyn, Phys. Rev. B **66**, 205303 (2002).
[26] M. Zwolak, J. Chem. Phys. **129**, 101101 (2008).
[27] A systematic way of optimizing the discretization scheme, base on analyzing the contribution of each level from the discretized band to the reduced density matrix of the local level, was recently proposed by Zwolak (Ref. 26).

Chapter 4

One- and Two-Bath Spin-Boson Models

In this chapter we use the NRG+VMPS scheme to explore the quantum phase diagram and critical properties of two specific quantum dissipative systems, namely the one- and two-bath spin boson models. In contrast to fermionic models, an individual bosonic degree of freedom already contains an infinite-dimensional state space, which posts a challenge to the conventional VMPS method. We introduce a shifted optimal boson basis into VMPS, and thereby extend the occupation of the local bosonic mode, which in the original basis is of order 10^1, to the order of 10^{10}. This is a crucial improvement for VMPS to be able to calculate the correct critical exponents of the quantum phase transition of SBM1; thus it enables us to settled a controversy regarding the quantum-to-classical mapping.

According to the quantum-to-classical mapping, a quantum phase transition in d-dimensional systems can be described as an equivalent classical phase transition in $d + z$ dimensional systems, where z is the dynamical exponent of the QPT [75]. However, there are also quantum phase transitions without such classical counter parts [81, 80, 76], and this specialty has intrigued people's interests in recent years.

The quantum-to-classical mapping relates the standard spin-boson model (called SBM1 below) to a one-dimension Ising model with a long range interaction of the form $1/r^{1+s}$. More specifically, this means that the quantum phase transition of SBM1 and the thermal phase transition of the 1D Ising model with long range interaction belong to the same universality class, which in turns predicts mean-field exponents for $s < 1/2$. However, a detailed NRG calculation gave a different picture: The critical exponents of SBM1 differ from the mean field exponents and satisfy hyperscaling [96, 51, 30] not only for $s > 1/2$ but also for $s < 1/2$, in contrast to the predictions from a quantum-to-classical mapping. However, when SBM1 was later studied with other numerical methods like Quantum Monte Carlo [111] and sparse polynomial space [2], they confirms mean-field prediction. Subsequent NRG calculations also favored the quantum-to-classical mapping [97, 95]. Nevertheless, there are still arguments [45] supporting the NRG result of non-mean-field exponents satisfying hyperscaling, which makes the controversy around the nature of this phase transition even more puzzling.

If one uses VMPS with a local dimension as small as those used in the previous NRG calculation, VMPS will generate the same critical exponents as NRG. However by introducing an optimal boson basis, we enlarge the local dimension that can be handled numerically by many orders of magnitude. This enables us to see the influence of the restricted local dimension to the results of critical exponents. Indeed, we confirm that the quantum-to-classical mapping holds if one use large enough local dimension in SBM1.

Having settled the controversy, we used the new developed method to study the more complicated two-bath spin boson model (SBM2). We find an interesting new critical phase in SBM2. We also do some preliminary study of its critical behavior, and there are also lots of open question left for further investigation.

In the following I will present our publication, complimented by additional studies which we have not included in the paper, while also pointing out further improvements of the algorithm.

4.1 Publication: Critical and Strong-Coupling Phases in One- and Two-Bath Spin-Boson Models

Critical and Strong-Coupling Phases in One- and Two-Bath Spin-Boson Models

Cheng Guo,[1] Andreas Weichselbaum,[1] Jan von Delft,[1] and Matthias Vojta[2]
[1]*Ludwig-Maximilians-Universität München, 80333 Munich, Germany*
[2]*Institut für Theoretische Physik, Technische Universität Dresden, 01062 Dresden, Germany*
(Received 11 November 2011; published 18 April 2012)

For phase transitions in dissipative quantum impurity models, the existence of a quantum-to-classical correspondence has been discussed extensively. We introduce a variational matrix product state approach involving an optimized boson basis, rendering possible high-accuracy numerical studies across the entire phase diagram. For the sub-Ohmic spin-boson model with a power-law bath spectrum $\propto \omega^s$, we confirm classical mean-field behavior for $s < 1/2$, correcting earlier numerical renormalization-group results. We also provide the first results for an XY-symmetric model of a spin coupled to two competing bosonic baths, where we find a rich phase diagram, including both critical and strong-coupling phases for $s < 1$, different from that of classical spin chains. This illustrates that symmetries are decisive for whether or not a quantum-to-classical correspondence exists.

DOI: 10.1103/PhysRevLett.108.160401 PACS numbers: 05.30.Jp, 05.10.Cc

Quantum spins in a bosonic environment are model systems in diverse areas of physics, ranging from dissipative quantum mechanics to impurities in magnets and biological systems [1]. In this Letter we consider the spin-boson model and a generalization thereof to two baths, described by $\mathcal{H}_{\rm sb} = -\vec{h}\cdot\vec{\sigma}/2 + \mathcal{H}_{\rm bath}$, with

$$\mathcal{H}_{\rm bath} = \sum_{i=x,y}\sum_q \left[\omega_q \hat{B}^\dagger_{qi}\hat{B}_{qi} + \lambda_{qi}\frac{\sigma_i}{2}(\hat{B}_{qi} + \hat{B}^\dagger_{qi})\right]. \quad (1)$$

The two-level system (or quantum spin, with $\sigma_{x,y,z}$ being the vector of Pauli matrices) is coupled both to an external field $\vec{h}$ and, via σ_x and σ_y, to two independent bosonic baths, whose spectral densities $J_i(\omega) = \pi\sum_q \lambda^2_{qi}\delta(\omega - \omega_q)$ are assumed to be of power-law form:

$$J_i(\omega) = 2\pi\alpha_i\omega_c^{1-s}\omega^s, \qquad 0 < \omega < \omega_c = 1. \quad (2)$$

Such models are governed by the competition between the local field, which tends to point the spin in the $\vec{h}$ direction, and the dissipative effects of the bosonic baths.

Indeed, the standard one-bath spin-boson model (SBM1), obtained for $\alpha_y = h_y = 0$, exhibits an interesting and much-studied [1–7] quantum phase transition (QPT) from a delocalized to a localized phase, with $\langle\sigma_x\rangle = 0$ or $\neq 0$, respectively, as α_x is increased past a critical coupling $\alpha_{x,c}$. According to statistical-mechanics arguments, this transition is in the same universality class as the thermal phase transition of the one-dimensional (1D) Ising model with $1/r^{1+s}$ interactions. This quantum-to-classical correspondence (QCC) predicts mean-field exponents for $s < 1/2$, where the Ising model is above its upper-critical dimension [8,9].

Checking this prediction numerically turned out to be challenging. Numerical renormalization-group (NRG) studies of SBM1 yielded non-mean-field exponents for $s < 1/2$ [4], thereby seemingly negating the validity of the QCC. However, the authors of Ref. [4] subsequently concluded [10] that those results were not reliable, due to two inherent limitations of the NRG method, which they termed (i) Hilbert-space truncation and (ii) mass flow. Problem (i) causes errors for critical exponents that characterize the flow into the localized phase at zero temperature, since $\langle\sigma_x\rangle \neq 0$ induces shifts in the bosonic displacements $\hat{X}_q = (\hat{B}_q + \hat{B}^\dagger_q)/\sqrt{2}$ of the bath oscillators which diverge in the low-energy limit for $s < 1$ and hence cannot be adequately described in the truncated boson Hilbert space used by the NRG method [11]. Problem (ii) arises for nonzero temperatures, due to the NRG's neglect of low-lying bath modes with energy smaller than temperature [12]. In contrast to the NRG results, two recent numerical studies of SBM1, using Monte Carlo methods [6] or a sparse polynomial basis [5], found mean-field exponents in agreement with the QCC. Nevertheless, other recent works continue to advocate the failure of the QCC [13].

The purpose of this Letter is twofold. First, we show how the problem (i) of Hilbert-space truncation can be controlled systematically by using a variational matrix-product state (VMPS) approach formulated on a Wilson chain. The key idea is to variationally construct an optimized boson basis (OBB) that captures the bosonic shifts induced by $\langle\sigma_x\rangle \neq 0$. The VMPS results confirm the predictions of the QCC for the QPT of SBM1 at $T = 0$. (Problem (ii) is beyond the scope of this work.) Second, we use the VMPS approach to study an XY-symmetric version of the two-bath spin-boson model (SBM2), with $\alpha_x = \alpha_y$. This model arises, e.g., in the contexts of impurities in quantum magnets [14,15] and of noisy qubits [14,16], and displays the phenomenon of "frustration of decoherence" [14]: the two baths compete (rather than cooperate), each tending to localize a different component of the spin. As a result, a nontrivial intermediate-coupling

(i.e., critical) phase has been proposed to emerge for $s < 1$ [15], which has no classical analogue. To date, the existence of this phase could only be established in an expansion in $(1 - s)$, and no numerical results are available. Here we numerically investigate the phase diagram, and, surprisingly, find that the perturbative predictions are valid for a small range of s and α only. We conclusively demonstrate the absence of a QCC for this model.

Wilson chain.—Following Refs. [3,11], which adapted Wilson's NRG to a bosonic bath, we discretize the latter using a logarithmic grid of frequencies $\omega_{ki} \propto \Lambda^{-k}$ (with $\Lambda > 1$ and k a positive integer) and map $\mathcal{H}_{\rm bath}$ onto a so-called Wilson chain of $(L - 1)$ bosonic sites:

$$\mathcal{H}_{\rm bath}^{(L-1)} = \sum_{i=x,y}\Big[\sqrt{\frac{\eta_i}{\pi}}\frac{\sigma_i}{2}(\hat{b}_{1i} + \hat{b}_{1i}^\dagger) + \sum_{k=1}^{L-2} t_{ki}(\hat{b}_{ki}^\dagger \hat{b}_{k+1,i} + \text{H.c.}) + \epsilon_{ki}\hat{n}_{ki}\Big]. \quad (3)$$

Here $\hat{n}_{ki} = \hat{b}_{ki}^\dagger \hat{b}_{ki}$, with eigenvalue n_{ki}, counts the bosons of type i on chain site k; the detailed form of the hopping parameters t_{ki}, on-site energies ϵ_{ki} (both $\propto \Lambda^{-k}$), and the coupling η_i between spin component σ_i and site 1, are obtained following Refs. [17,18]. To render a numerical treatment feasible, the infinite-dimensional bosonic Hilbert space at each site k is truncated by restricting the boson number to $0 \le n_{ki} < d_k$ ($d_k \le 14$ in Refs. [3,11]).

The standard NRG strategy for finding the ground state of $\mathcal{H}_{\rm sb}^{(L)} = -\vec{h}\cdot\vec{\sigma}/2 + \mathcal{H}_{\rm bath}^{(L-1)}$ is to iteratively diagonalize it one site at a time, keeping only the lowest-lying D energy eigenstates at each iteration. This yields an L-site matrix-product state (MPS) [19–21] of the following form (depicted in Fig. 1, dashed boxes):

$$|G\rangle = \sum_{\sigma=\uparrow,\downarrow}\sum_{\{\vec{n}\}} A^0[\sigma]A^1[n_1]\cdots A^{L-1}[n_{L-1}]|\sigma\rangle|\vec{n}\rangle. \quad (4)$$

Here $|\sigma\rangle = |\uparrow\rangle, |\downarrow\rangle$ are eigenstates of σ_x; the states $|\vec{n}\rangle = |n_1, \ldots, n_{L-1}\rangle$ form a basis of boson-number eigenstates within the truncated Fock space, with $\hat{n}_{ki}|\vec{n}\rangle = n_{ki}|\vec{n}\rangle$ and $0 \le n_{ki} < d_k$. For SBM2, $n_k = (n_{kx}, n_{ky})$ labels the states of supersite k representing both chains. Each $A^k[n_k]$ is a matrix (not necessarily square, but of maximal dimension $D \times D$, with A^0 a row matrix and A^{L-1} a column matrix), with matrix elements $(A^k[n_k])_{\alpha\beta}$.

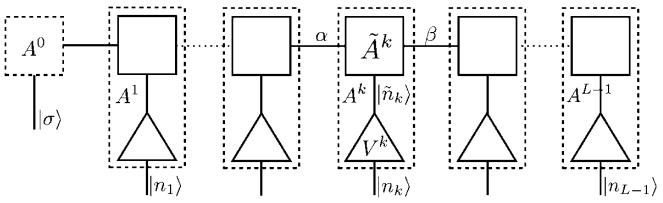

FIG. 1. Depiction of the MPS Eq. (4), with each A-matrix expressed in an optimal boson basis via $A = \tilde{A}V$ [Eq. (5)].

The need for Hilbert-space truncation with small d_k prevents the NRG method from accurately representing the shifts in the displacements $\hat{x}_{ki} = (\hat{b}_{ki} + \hat{b}_{ki}^\dagger)/\sqrt{2}$ that occur in the localized phase. This problem can be avoided, in principle, by using an OBB, chosen such that it optimally represents the quantum fluctuations of *shifted* oscillators, $\hat{x}'_{ki} = \hat{x}_{ki} - \langle\hat{x}_{ki}\rangle$. While attempts to accommodate this strategy within the standard NRG approach were unsuccessful [11], it was shown to work well [5] using an alternative representation of SBM1 using a sparse polynomial basis.

VMPS method.—We now show that an OBB can also be constructed on a Wilson chain. To this end, view the state $|G\rangle$ of Eq. (4) as a MPS ansatz for the ground state of $\mathcal{H}_{\rm sb}^{(L)}$, that is to be optimized *variationally* using standard MPS methods [19–21]. To allow the possibility of large bosonic shifts, we represent the A-matrix elements as [22–24] (Fig. 1, solid lines)

$$(A^k[n_k])_{\alpha\beta} = \sum_{\tilde{n}_k=0}^{d_{\rm opt}-1} (\tilde{A}^k[\tilde{n}_k])_{\alpha\beta} V^k_{\tilde{n}_k n_k} \qquad (k \ge 1). \quad (5)$$

Here V^k in effect implements a transformation to a new boson basis on site k, the OBB, of the form $|\tilde{n}_k\rangle = \sum_{n_k=0}^{d_k-1} V^k_{\tilde{n}_k n_k}|n_k\rangle$ with $0 \le \tilde{n}_k < d_{\rm opt}$. (For SBM2, V^k is a rank-3 tensor.) This ansatz has the advantage that the size of the OBB, $d_{\rm opt}$, can be chosen to be much smaller ($d_{\rm opt} \lesssim 50$) than d_k. Following standard VMPS strategy, we optimize the $\tilde{A}^k$ and V^k matrices one site at a time through a series of variational sweeps through the Wilson chain. As further possible improvement before optimizing a given site, the requisite boson shift can be implemented by hand in the Hamiltonian itself: we first determine the "current" value of the bosonic shift $\langle\hat{x}_{ki}\rangle$ using the current variational state $|G\rangle$, then use it as a starting point to variationally optimize a new $|G'\rangle$ with respect to the shifted Hamiltonian $\mathcal{H}'^{(L)}_{\rm sb}(\hat{b}_{ki}, \hat{b}_{ki}^\dagger) = \mathcal{H}^{(L)}_{\rm sb}(\hat{b}'_{ki}, \hat{b}'^\dagger_{ki})$, with $\hat{b}'_{ki} = \hat{b}_{ki} - \langle\hat{x}_{ki}\rangle/\sqrt{2}$. The shifted OBB protocol, described in detail in Ref. [18], allows shifts that would have required $d_k^{\rm eff} \approx 10^{10}$ states in the original boson basis to be treated using rather small d_k (we used $d_k = 100$).

Spin-boson model.—We applied the VMPS method to SBM1 ($\alpha_y = h_y = 0$), with dissipation strength $\alpha \equiv \alpha_x$ and fixed transverse field $h_z = 0.1$, at $T = 0$. We focussed on the QPT between the delocalized and localized phases in the sub-Ohmic case, $s < 1$. Here, the controversy [4–6,10,13] concerns the order-parameter exponents β and δ, defined via $\langle\sigma_x\rangle \propto (\alpha - \alpha_c)^\beta$ at $h_x = 0$ and $\langle\sigma_x\rangle \propto h_x^{1/\delta}$ at $\alpha = \alpha_c$, respectively. QCC predicts mean-field values $\beta_{\rm MF} = 1/2$, $\delta_{\rm MF} = 3$ for $s < 1/2$ [8], whereas initial NRG results [4] showed s-dependent non-mean-field exponents.

In Fig. 2(a), we show sample VMPS results for $\langle\sigma_x\rangle$ vs $(\alpha - \alpha_c)$ for $s = 0.3$ at $h_x = 0$, where α_c was tuned to yield the best straight line on a log-log plot. The results

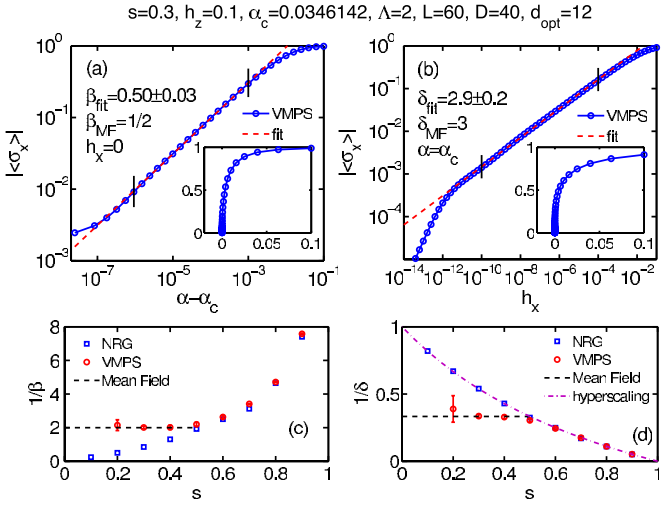

FIG. 2 (color online). VMPS results for the order parameter of SBM1 near criticality. (a) $\langle\sigma_x\rangle$ vs $(\alpha-\alpha_c)$ at $h_x=0$, and (b) $\langle\sigma_x\rangle$ vs h_x at $\alpha=\alpha_c$, on linear plots (insets) or log-log plots (main panels). Dashed lines are power-law fits in the ranges between the vertical marks. (c),(d) Comparison of the exponents β and δ for different s obtained from the VMPS method, NRG studies [4], mean-field theory, and, in (d), the exact hyperscaling result $\delta=(1+s)/(1-s)$ which applies for $s>1/2$. (See also [18], Fig. S7).

display power-law behavior over more than 3 decades, with an exponent $\beta=0.50\pm0.03$. Deviations at small $(\alpha-\alpha_c)$ can be attributed to a combination of finite chain length and numerical errors of the VMPS method. Figure 2(b) shows $\langle\sigma_x\rangle$ vs h_x at $\alpha=\alpha_c$, and a power-law fit over 6 decades results in $\delta=2.9\pm0.2$. Power laws of similar quality can be obtained for all $s\gtrsim0.2$ [18,25] (see [18], Fig. S7).

The exponents β and δ obtained from such fits are summarized in Figs. 2(c) and 2(d). For $s<1/2$ they are consistent with the mean-field values predicted by QCC, also found in Monte Carlo [6] and exact-diagonalization studies [5], but are at variance with the NRG data of Ref. [4]. Since both the NRG and VMPS methods handle the same microscopic model $\mathcal{H}_{\rm sb}^{(L)}$ defined on the Wilson chain, but the VMPS method can deal with much larger $d_k^{\rm eff}$ values ($\lesssim10^{10}$ in Fig. 2) than the NRG method, the incorrect NRG results must originate from Hilbert-space truncation, as anticipated in Ref. [10]. Indeed, artificially restricting d_k to small values in the VMPS approach reproduces the incorrect NRG exponents (see [18], Fig. S6).

Two-bath model.—We now turn to SBM2, a generalization of the spin-boson model. Here, the two baths may represent distinct noise sources [14,16] or XY-symmetric magnetic fluctuations [14,15,26]. Perturbation theory shows that the two baths compete: A straightforward expansion around the free-spin fixed point ($\alpha=h=0$) results in the following one-loop renormalization-group (RG) equations at $\vec{h}=0$:

$$\begin{aligned}\beta(\alpha_x)&=(1-s)\alpha_x-\alpha_x\alpha_y,\\ \beta(\alpha_y)&=(1-s)\alpha_y-\alpha_x\alpha_y.\end{aligned}\tag{6}$$

For $\alpha\equiv\alpha_x=\alpha_y$, these equations predict a stable intermediate-coupling fixed point at $\alpha^*=1-s$, describing a *critical* phase. It is characterized by $\langle\vec{\sigma}\rangle=0$, a *nonlinear* response of $\langle\vec{\sigma}\rangle$ to an applied field $\vec{h}$, and a finite ground-state entropy smaller than ln2, all corresponding to a fluctuating fractional spin [15,27]. This phase is unstable with respect to finite bath asymmetry ($\alpha_x\neq\alpha_y$) and finite field. It had been assumed [15] that this critical phase exists for all $0<s<1$ and is reached for any α.

We have extensively studied SBM2 using the VMPS method; the results are summarized in the $\vec{h}=0$ phase diagram in Fig. 3(a) and the flow diagrams in Fig. 4. Most importantly, we find that the critical phase (CR) indeed exists, but only for $s^*<s<1$, with a universal $s^*=0.75\pm0.01$. Even in this s range, the critical phase is left once α is increased beyond a critical value $\alpha_c(s)$, which marks the location of a continuous QPT into a localized phase (L) with spontaneously broken XY symmetry and finite $\langle\sigma_{x,y}\rangle$. This localized phase exists down to $s=0$, Fig. 3(a). It can be destabilized by applying a transverse field h_z beyond a critical value $h_z^c(\alpha)$, marking the location of a continuous QPT into a delocalized phase (D) with a unique ground state (see Ref. [18], Fig. S9). Finally, for $s\geq1$ we only find weak-coupling behavior; i.e., the impurity behaves as a free (F) spin .

In Fig. 3(b) (and Ref. [18], Fig. S10) we show results for the transverse-field response, $\langle\sigma_z\rangle\propto h_z^{1/\delta'}$, which can be used to characterize the different zero-field phases. $\langle\sigma_z\rangle$ is linear in h_z in L ($\delta'=1$), sublinear in CR ($\delta'>1$), and extrapolates to a finite value in F. For CR, a perturbative calculation gives $1/\delta'=(1-s)+\mathcal{O}([1-s]^2)$ [15] (confirmed numerically in Ref. [18], Fig. S11b), while the

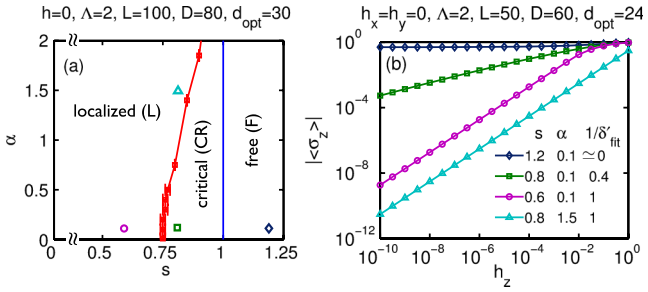

FIG. 3 (color online). (a) Phase diagram of SBM2 in the s-α plane for $\vec{h}=0$, with dissipation strength $\alpha\equiv\alpha_x=\alpha_y$. The critical phase only exists for $s^*<s<1$, and its boundary $\alpha_c\to\infty$ for $s\to1^-$. (Ref. [18] describes the determination of the phase boundary and gives a 3D sketch of the s-α-h_z phase diagram, see Fig. S8.) (b) Tranverse-field response of SBM2, $\langle\sigma_z\rangle\propto h_z^{1/\delta'}$, for four choices of s and α, showing free (diamonds), critical (squares) and localized (triangles, circles) behavior.

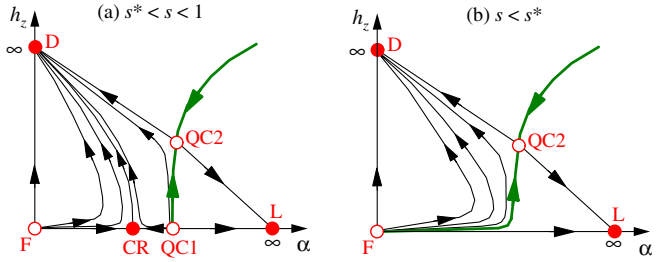

FIG. 4 (color online). Schematic RG flow for SBM2 in the α-h_z plane ($h_x = h_y = 0$). The thick lines correspond to a continuous QPT; the full (open) circles are stable (unstable) fixed points, for labels see text. (a) $s^* < s < 1$: CR is reached for small α and $h_z = 0$, it is separated from L by a QPT controlled by the multicritical QC1 fixed point. Equation (6) implies that CR is located at $\alpha^* = 1 - s + \mathcal{O}[(1-s)^2]$. For finite h_z, a QPT between D and L occurs, controlled by QC2. (b) $0 < s < s^*$: both CR and QC1 have disappeared, such that the only transition is between D and L.

linear response in L corresponds to that of an ordered XY magnet to a field perpendicular to the easy plane.

From the VMPS results, we can schematically construct the RG flow, Fig. 4. There are three stable RG fixed points for $s^* < s < 1$, corresponding to the L, D, and CR phases. From this we deduce the existence of two unstable critical fixed points, QC1 and QC2, controlling the QPTs [Fig. 4(a)]. Equation (6) predicts that, as $s \to 1^-$, CR merges with F; this is consistent with our results for δ' which indicate $\delta' \to \infty$ as $s \to 1^-$ (Ref. [18], Fig. S11b). The behavior of the phase boundary α_c in Fig. 3(a) suggests that QC1 moves towards $\alpha = \infty$ for $s \to 1^-$. Thus, for $s \geq 1$ only F is stable on the $\vec{h} = 0$ axis. Conversely, from Eq. (6) and Fig. 3(a) we extract that, upon lowering s, CR (QC1) moves to larger (smaller) α. From the absence of CR for small s we then conclude that CR and QC1 merge and disappear as $s \to s^{*+}$. Consequently, for $s < s^*$ we have only D and L as stable phases, separated by a transition controlled by QC2, Fig. 4(b). The merger of CR and QC1 at $s = s^*$ also implies that the phase boundary between CR and L in Fig. 3(b) at s^* is vertical at small α (Ref. [18], Sec. V.C), because the merging point on the α axis defines the finite value of α_c at $s \to s^{*+}$.

Taken together, the physics of SBM2 is much richer than that of a classical XY-symmetric spin chain with long-range interactions, which only shows a single thermal phase transition [28]. Given this apparent failure of the QCC for SBM2, it is useful to recall the arguments for QCC for SBM1: A Feynman path-integral representation of Eq. (1), with nonzero h_z, can be written down using eigenstates of both σ_x and σ_z. Integrating out the bath generates a long-range (in time) interaction for σ_x. Subsequently, the σ_z degrees of freedom can be integrated out as well, leaving a model formulated in σ_x only. Reinterpreting the σ_x values for the individual time slices in terms of Ising spins, one arrives at a 1D Ising chain with both short-range and $1/r^{1+s}$ interactions, with the thermodynamic limit corresponding to the $T \to 0$ limit of the quantum model. Repeating this procedure for SBM2 with $\vec{h} = 0$, one obtains a Feynman path integral in terms of eigenstates of σ_x and σ_y. Importantly, both experience long-range interactions and hence neither can be integrated out. This leads to a representation in terms of *two* coupled Ising chains. However, upon reexponentiating the matrix elements, the coupling between the two chains turns out to be imaginary, such that a classical interpretation is *not* possible [29]. In other words, a Feynman path-integral representation of SBM2 leads to negative Boltzmann weights, i.e., a sign problem.

Conclusion.—Our implementation of the OBB-VMPS method on the Wilson chain brings the Hilbert-space truncation problem of the bosonic NRG method under control and allows for efficient ground-state computations of bosonic impurity models. We have used this to verify the QCC in SBM1 and to determine the phase diagram of SBM2, which is shown to violate QCC. This underlines that symmetries are decisive for whether or not a QCC exists. A detailed study of the QPTs of SBM2 is left for future work.

The results for SBM2 also show that the predictions from a weak-coupling RG calculation are *not* valid for all parameters and bath exponents, in contrast to expectations. This implies that studying a *three*-bath version of the spin-boson model, which is related to the physics of a magnetic impurity in a quantum-critical magnet [15,27], is an interesting future subject.

We thank A. Alvermann, S. Florens, S. Kirchner, K. Ingersent, Q. Si, A. Schiller, and T. Vojta for helpful discussions. This research was supported by the Deutsche Forschungsgemeinschaft through SFB/TR12, SFB631, FOR960, by the German-Israeli Foundation through G-1035-36.14, and the NSF through PHY05-51164.

[1] A. J. Leggett *et al.*, Rev. Mod. Phys. **59**, 1 (1987).
[2] S. K. Kehrein and A. Mielke, Phys. Lett. A **219**, 313 (1996).
[3] R. Bulla, N. Tong, and M. Vojta, Phys. Rev. Lett. **91**, 170601 (2003).
[4] M. Vojta, N. Tong, and R. Bulla, Phys. Rev. Lett. **94**, 070604 (2005).
[5] A. Alvermann and H. Fehske, Phys. Rev. Lett. **102**, 150601 (2009).
[6] A. Winter, H. Rieger, M. Vojta, and R. Bulla, Phys. Rev. Lett. **102**, 030601 (2009).
[7] H. Wong and Z. Chen, Phys. Rev. B **77**, 174305 (2008).
[8] M. E. Fisher, S. K. Ma, and B. G. Nickel, Phys. Rev. Lett. **29**, 917 (1972).
[9] E. Luijten and H. W. J. Blöte, Phys. Rev. B **56**, 8945 (1997).

[10] M. Vojta, N. Tong, and R. Bulla, Phys. Rev. Lett. **102**, 249904(E) (2009).
[11] R. Bulla, H. J. Lee, N. H. Tong, and M. Vojta, Phys. Rev. B **71**, 045122 (2005).
[12] M. Vojta, R. Bulla, F. Güttge, and F. Anders, Phys. Rev. B **81**, 075122 (2010).
[13] S. Kirchner, Q. Si, and K. Ingersent, Phys. Rev. Lett. **102**, 166405 (2009).
[14] A. H. Castro Neto, E. Novais, L. Borda, G. Zarand, and I. Affleck, Phys. Rev. Lett. **91**, 096401 (2003); E. Novais, A. H. Castro Neto, L. Borda, I. Affleck, and G. Zarand, Phys. Rev. B **72**, 014417 (2005).
[15] L. Zhu and Q. Si, Phys. Rev. B **66**, 024426 (2002); G. Zarand and E. Demler, Phys. Rev. B **66**, 024427 (2002).
[16] D. V. Khveshchenko, Phys. Rev. B **69**, 153311 (2004).
[17] R. Žitko and T. Pruschke, Phys. Rev. B **79**, 085106 (2009).
[18] See Supplemental Material at http://link.aps.org/supplemental/10.1103/PhysRevLett.108.160401 for a detailed description of our VMPS approach and additional numerical results on SBM1 and SBM2.
[19] A. Weichselbaum, F. Verstraete, U. Schollwöck, J. I. Cirac, and J. von Delft, Phys. Rev. B **80**, 165117 (2009).
[20] H. Saberi, A. Weichselbaum, and J. von Delft, Phys. Rev. B **78**, 035124 (2008).
[21] U. Schollwöck, Ann. Phys. (Leipzig) **326**, 96 (2011).
[22] C. Zhang, E. Jeckelmann, and S. R. White, Phys. Rev. Lett. **80**, 2661 (1998).
[23] A. Weiße, H. Fehske, G. Wellein, and A. R. Bishop, Phys. Rev. B **62**, R747 (2000).
[24] Y. Nishiyama, Eur. Phys. J. B **12**, 547 (1999).
[25] For very small s, high-accuracy numerical calculations inside the localized phase become prohibitively expensive.
[26] S. Kirchner, L. Zhu, Q. Si, and D. Natelson, Proc. Natl. Acad. Sci. U.S.A. **102**, 18 824 (2005).
[27] M. Vojta, C. Buragohain, and S. Sachdev, Phys. Rev. B **61**, 15 152 (2000).
[28] J. M. Kosterlitz, Phys. Rev. Lett. **37**, 1577 (1976).
[29] T. Vojta (private communication).

Supplementary Information for "Critical and strong-coupling phases in one- and two-bath spin-boson models"

Cheng Guo,[1] Andreas Weichselbaum,[1] Jan von Delft,[1] and Matthias Vojta[2]
[1]*Ludwig-Maximilians-Universität München, Germany*
[2]*Institut für Theoretische Physik, Technische Universität Dresden, 01062 Dresden, Germany*
(Dated: April 16, 2012)

I. DISCRETIZATION AND MAPPING TO THE WILSON CHAIN

The spin-boson model represents a prototypical quantum-impurity setup, with the bath consisting of non-interacting particles. As such it is amenable to the concept of energy scale separation present in the NRG[1–3]. For this, the quantum impurity Hamiltonian of the spin-boson model is mapped onto a so-called Wilson chain, which includes two steps: (i) coarse graining of the bath (logarithmic discretization), followed (ii) by a mapping onto a semi-infinite bosonic chain with the spin-impurity connected to its starting point.

The bath spectral function $J_i(\omega)$ of each bosonic bath i is assumed to be non-zero in the interval $\omega \in [0, \omega_c]$, with ω_c an upper cutoff frequency. The bath spectral function $J_i(\omega)$ is discretized then in energy-space into intervals $[\omega_{m+1}, \omega_m]$, marked by the decreasing sequence ω_m $(m = 0, 1, \ldots)$ with $\omega_0 = \omega_c$ and $\lim_{m\to\infty} \omega_m = 0$. Assuming two identical baths $i \in \{x, y\}$ that couple to the Pauli matrices σ_i of the impurity, respectively, the discretized Hamiltonian has the form

$$\mathcal{H}_{\rm bath} = \sum_{i=x,y} \sum_{m=0}^{\infty} \left[\xi_m \hat{B}^\dagger_{mi} \hat{B}_{mi} + \frac{\sigma_i}{2\sqrt{\pi}} \gamma_m (\hat{B}_{mi} + \hat{B}^\dagger_{mi})\right], \tag{S1}$$

Here $\hat{B}^\dagger_{mi}$ $(\hat{B}_{mi})$ is the creation (annihilation) operator, respectively, of a free boson with energy ξ_m, that is coupled to the impurity spin with strength γ_m. Moreover,

$$\xi_m = \frac{\int_{\omega_{m+1}}^{\omega_m} J(x)dx}{\int_{\omega_{m+1}}^{\omega_m} (J(x)/x)dx}$$
$$\gamma_m = \left(\int_{\omega_{m+1}}^{\omega_m} J(x)dx\right)^{1/2}. \tag{S2}$$

We prefer a logarithmic discretization scheme over a linear or power-law discretization, since the study of critical behavior requires very small energy scales to be resolved. This would require too many chain sites for linear and even power-law discretization schemes. Moreover, logarithmic discretization is ideally suited to represent scale-invariant physics near a quantum phase transition, and it has the advantage that characteristic NRG information, such as the energy flow diagram used to analyze the fixed points of the system, can be extracted from our VMPS results, if desired. (This will be elaborated upon in a separate publication[4].)

In this paper we use the improved logarithmic discretization recently proposed by Žitko and Pruschke[5]. As this achieves a more consistent description of the bath, it reduces discretization effects and hence allows to determine phase boundaries such as the critical coupling strength α_c more accurately. Thus we choose the discretization intervals as

$$\begin{aligned} \omega_0^z &= \omega_c, \\ \omega_m^z &= \omega_c \Lambda^{1-m-z}, \quad (m = 1, 2, 3, \ldots) \end{aligned} \tag{S3}$$

with $\Lambda > 1$ Wilson's logarithmic discretization parameter[1], and $z \in]0, 1]$ an arbitrary shift[6]. By solving the differential equation in App. C of Ref. 5 analytically, we obtain the following explicit expressions for the parameters in Eq. (S2):

$$\begin{aligned} \xi_0^z &= \left[\frac{1-\Lambda^{-z(1+s)}}{(1+s)\ln\Lambda} - z + 1\right]^{\frac{1}{1+s}}, \\ \xi_m^z &= \left[\frac{\Lambda^{-(1+s)(m+z)}(\Lambda^{1+s}-1)}{(1+s)\ln\Lambda}\right]^{\frac{1}{1+s}}, \quad (m = 1, 2, 3, \ldots) \end{aligned} \tag{S4}$$

$$\begin{aligned} \gamma_0^z &= \sqrt{\tfrac{2\pi\alpha}{1+s}(1-\Lambda^{-z(1+s)})}, \\ \gamma_m^z &= \sqrt{\tfrac{2\pi\alpha}{1+s}(\Lambda^{1+s}-1)\Lambda^{-(m+z)(1+s)}} \quad (m = 1, 2, 3, \ldots) \end{aligned} \tag{S5}$$

Having discretized the Hamiltonian, the mapping onto the Wilson chain is done numerically using standard Lanzcos tridiagonalization. For the calculations in this paper, we use $z = 1$.

We find that, with the discretization scheme of Žitko and Pruschke,[5] the Λ-dependence of α_c is much weaker than for the traditional discretization scheme[1,3], i.e., α_c converges rapidly as Λ is decreased towards 1. Similar to standard NRG, critical exponents do not dependent on Λ, as shown in Fig. S1 for the exponent β.

II. OBB-VMPS OPTIMIZATION PROCEDURE

As discussed in the main paper, we use a MPS of the following general form:

$$|G\rangle = \sum_{\sigma=\uparrow,\downarrow} \sum_{\{\vec{n}\}} A^0[\sigma] A^1[n_1] \cdots A^{L-1}[n_{L-1}] |\sigma\rangle |\vec{n}\rangle \,. \tag{S6}$$

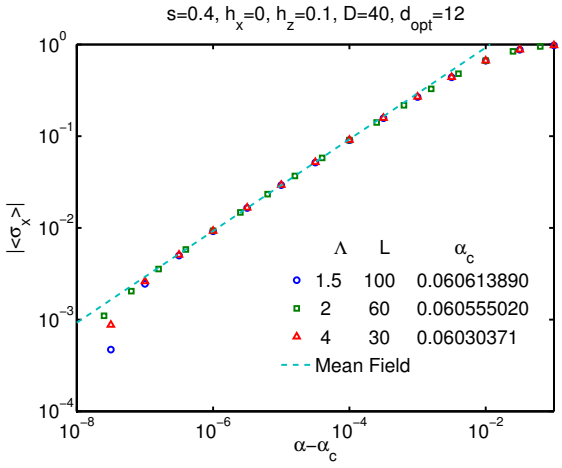

FIG. S1: $\langle\sigma_x\rangle$ as function of $(\alpha-\alpha_c)$ for SBM1, using three different choices of the discretization parameter Λ (and, correspondingly, different chain lengths L). The data illustrate that the critical exponent β, obtained from power-law fits to this data, is essentially independent of Λ. The dashed line represents a power law $\langle\sigma_x\rangle \propto (\alpha-\alpha_c)^{\beta}$ with mean-field exponent $\beta_{\rm MF}=1/2$.

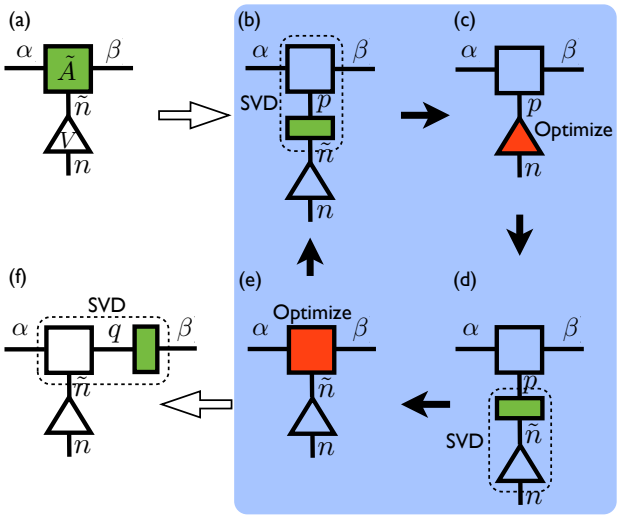

FIG. S2: Update procedure at one site when sweeping from left to right. The matrices surrounded by the dashed lines are the outcome of singular value decomposition (SVD). The filled squares or triangles indicate the "current focus" of each step. Filled arrows indicate the local update loop (highlighted by the shaded area), open arrows indicate its entry and exit.

The A-matrix elements are represented as

$$(A^k[n_k])_{\alpha\beta} = \sum_{\tilde{n}_k=0}^{d_{\rm opt}-1} (\tilde{A}^k[\tilde{n}_k])_{\alpha\beta} V^k_{\tilde{n}_k n_k} \quad (k\geq 1)\,, \qquad \text{(S7)}$$

in order to allow for the construction of an effective optimized boson basis (OBB) on each site k, given by

$$|\tilde{n}_k\rangle = \sum_{n_k=0}^{d_k-1} V^k_{\tilde{n}_k n_k}|n_k\rangle \quad (\tilde{n}_k=0,\ldots,d_{\rm opt}-1)\,. \qquad \text{(S8)}$$

The VMPS ansatz (S6) for the ground state of the Wilson chain is completely analogous to standard finite-size DMRG[7], and the use of an optimized local basis [Eqs. (S7) and (S8)] was pioneered in Ref. 8, finding subsequent applications in, for example, Refs. 9,10. The variational optimization of the resulting MPS with respect to the Hamiltonian $\mathcal{H}_{\rm sb}^{(L)}$ given in the main paper, depicted in Fig. 1 there, proceeds by iteratively updating the $\tilde{A}$- and V-matrices through a series of sweeps through the chain. Given the directed structure of the Wilson chain from large energy scales (left side of the MPS) to small energy scales (right side of the MPS), similar to the NRG, variational energy-lowering updates are performed only when sweeping from left to right. In contrast, during the reverse sweep from right to left the physical state (and its energy expectation value) is left unchanged. Nevertheless, during the reverse sweep the A-matrices are recast into a right-orthonormalized form, to ensure that the right low-energy part of the Wilson chain is described in terms of properly orthonormalized *effective* basis sets.

To get started, the MPS is always initialized randomly, followed by proper orthonormalization. To update the coefficient spaces related to a given site k of the Wilson chain, we perform the following steps, depicted schematically in Fig. S2 (we suppress the index k below):

(a) At a given site, the starting point is a well-defined local setting in terms of orthonormal basis sets $|\alpha\rangle$, $|\beta\rangle$, and $|\tilde{n}\rangle$ of the A-tensor for an effective left, right, and full local state space, respectively, as depicted in Fig. S2(a). The current approximation to the overall ground-state wave function therefore has its focus on the $\tilde{A}$-tensor of site n, and, setting $\tilde{A}_{\alpha\beta\tilde{n}} \equiv (\tilde{A}[\tilde{n}])_{\alpha\beta}$, can be written as

$$|\psi\rangle \equiv \sum_{\alpha\beta\tilde{n}} \tilde{A}_{\alpha\beta\tilde{n}}|\alpha\rangle|\beta\rangle|\tilde{n}\rangle. \qquad \text{(S9)}$$

(b) Downward-orthonormalization of $\tilde{A}$-tensor to move the focus to the V-matrix: combine the left state space α with the right state space β into one index, and use the effective local state space $\tilde{n}$ as another index. Then singular value decomposition (SVD) of the resulting matrix,

$$\tilde{A}_{\alpha\beta\tilde{n}} = \tilde{A}_{(\alpha\beta)\tilde{n}} = \sum_p \tilde{A}'_{(\alpha\beta)p}\lambda_p B_{p\tilde{n}}, \qquad \text{(S10)}$$

generates a new orthonormal tensor $\tilde{A}'$ that describes a combined description of the product space (α,β), such that

$$\sum_{(\alpha\beta)} \tilde{A}'_{(\alpha\beta)p}\tilde{A}'^{*}_{(\alpha\beta)p'} = \delta_{pp'}. \qquad \text{(S11)}$$

The wave function can now be represented as

$$|\psi\rangle = \sum_{p\tilde{n}} \lambda_p B_{p\tilde{n}} |p\rangle|\tilde{n}\rangle. \tag{S12}$$

This description of the rest of the system in terms of an orthonormal effective basis $|p\rangle$ is used to represent operators that connect the rest of the system with the current local state space. Being orthonormal, it also makes the numerics simple and stable.

(c) By contracting the remaining box B from the last step onto the V-matrix, this shifts the focus down to the $\tilde{V}$-matrix

$$\tilde{V}_{pn} = \sum_{\tilde{n}} \lambda_p B_{p\tilde{n}} V_{\tilde{n}n}, \tag{S13}$$

which thus has been altered. Having shifted the focus, the ground state is now represented as

$$|\psi\rangle \equiv \sum_{p,n} \tilde{V}_{pn} |p\rangle|n\rangle, \tag{S14}$$

where the $\tilde{V}$-matrices connect the orthonormal state spaces p and with the local boson space n. So far, the transformation of $|\psi\rangle$ has been exact with Eq. (S14) describing the same state as Eq. (S9). Transform the Hamiltonian and operators into the basis $|p\rangle|n\rangle$ and solve the eigenvalue problem

$$\sum_{(pn)} H_{(p'n')(pn)} \tilde{V}_{(pn)} = E_g \tilde{V}_{(p'n')}, \tag{S15}$$

for the ground state of the system. Thus the resulting $\tilde{V}$-matrix represents the *updated* ground state via Eq. (S14).

(d) Upward-orthonormalization of the $\tilde{V}$-matrix: the singular value decomposition of $\tilde{V}$,

$$\tilde{V}_{np} = \sum_{\tilde{n}} V_{n\tilde{n}} s_{\tilde{n}} C_{\tilde{n}p}\ , \tag{S16}$$

provides a new effective description of the local boson space, such that the transformation matrix V from the original boson basis to the OBB is orthogonal:

$$\sum_{n} V_{n\tilde{n}} V^*_{n\tilde{n}'} = \delta_{\tilde{n}\tilde{n}'}. \tag{S17}$$

Note that the singular values $s_{\tilde{n}}$ indicate the relative importance of the optimal boson bases. We will come back to this point at the end of this section. At this step the wave function is

$$|\psi\rangle = \sum_{\tilde{n}p} s_{\tilde{n}} C_{\tilde{n}p} |\tilde{n}\rangle|p\rangle. \tag{S18}$$

(e) By contracting the remaining box $s_{\tilde{n}}C$ from the previous step onto the $\tilde{A}'$-matrix, similar with step (c), the focus can be shifted to the $\tilde{A}$-matrix again:

$$\tilde{A}_{\alpha\beta\tilde{n}} = \sum_{p} \tilde{A}'_{\alpha\beta p} s_{\tilde{n}} C_{\tilde{n}p}. \tag{S19}$$

The wave function is thus reexpressed in the same form as Eq. (S12). Now transform the local operators to the OBB $|\tilde{n}\rangle$ using V, and optimize the $\tilde{A}_{\alpha\beta\tilde{n}}$ matrix in the same way as done using the traditional VMPS method.

(f) Combine the left and local indices and perform a singular value decomposition of the $\tilde{A}_{\alpha\beta\tilde{n}}$ matrix:

$$\tilde{A}_{\alpha\beta\tilde{n}} = \tilde{A}_{(\alpha\tilde{n})\beta} = \sum_{q} \tilde{A}_{(\alpha\tilde{n})q} r_q F_{q\beta}. \tag{S20}$$

The resulting tensor $\tilde{A}_{\alpha q\tilde{n}}$ is left orthogonal:

$$\sum_{\alpha\tilde{n}} \tilde{A}_{\alpha q\tilde{n}} \tilde{A}^*_{\alpha q'\tilde{n}} = \delta_{qq'}. \tag{S21}$$

Contracting the remaining $r_q F_{q\beta}$ to the $\tilde{A}$ tensor on the right side completes the update of the current site.

The OBB method enables us to increase the number d_k of local states that can be kept in the original basis from a few dozen to $d_k \lesssim 10^4$. (In the next section we shall show that by implementing explicit oscillator shifts, the *effective* number of local boson states that are accounted for in the unshifted basis can be increased to more than 10^{10}.)

The two adjustable VMPS parameters are the dimension D of the VMPS matrices (corresponding to the number of DMRG states kept) and the dimension $d_{\rm opt}$ of the optimal boson basis. To exemplify the influence of D and $d_{\rm opt}$ on physical quantities, Fig. S3 plots the magnetization $\langle\sigma_x\rangle$ for SBM1 as a function of α for different D and $d_{\rm opt}$. Clearly, $\alpha_{\rm c}$ is already well converged throughout. In practice, we chose D and $d_{\rm opt}$ large enough to ensure that all singular values [$s_{\tilde{n}}$ and r_q in Eqs. (S16) and (S20)] larger than 10^{-5} were retained throughout the entire Wilson chain, except possibly at its very end. We will explain this in more detail in the next section, when discussing Fig. S7 below.

For SBM2 with two bosonic baths, on the other hand, the combination of two boson sites into one supersite requires numerical parameters such as D and $d_{\rm opt}$ to be set to larger values than for SBM1. Nevertheless, we find that the number of kept states needed to ensure an accuracy comparable to that of SBM1 is smaller than the D^2 or $d^2_{\rm opt}$ that might have been naively expected from the fact that the local state space now has a direct product structure.

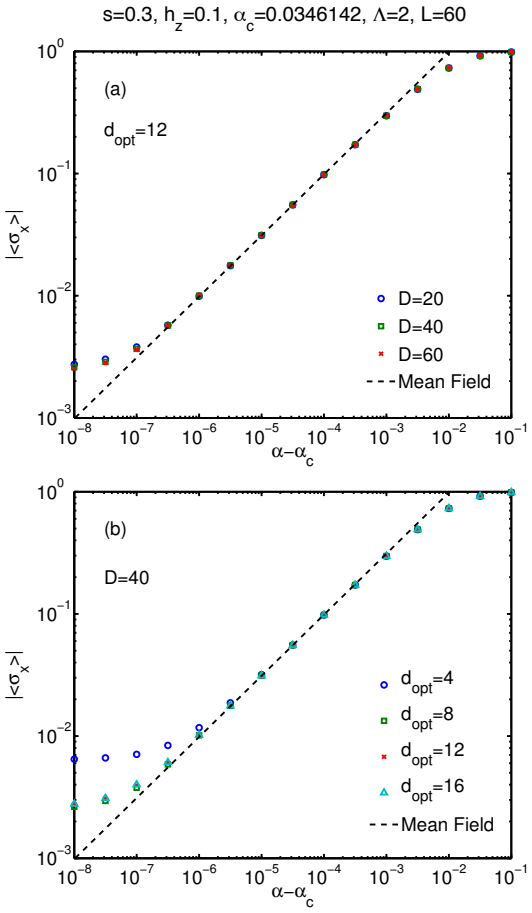

FIG. S3: Convergence check for the VMPS parameters D (a) and $d_{\rm opt}$ (b), for SBM1. The panels show $\langle\sigma_x\rangle$ as function of α_x for different choices of D and $d_{\rm opt}$, respectively. Since critical exponents are obtained from fits to the linear parts of such curves, the resulting exponents are evidently not sensitive to D and $d_{\rm opt}$. As in Fig. S1, the dashed lines show the mean-field power law with $\beta_{\rm MF} = 1/2$.

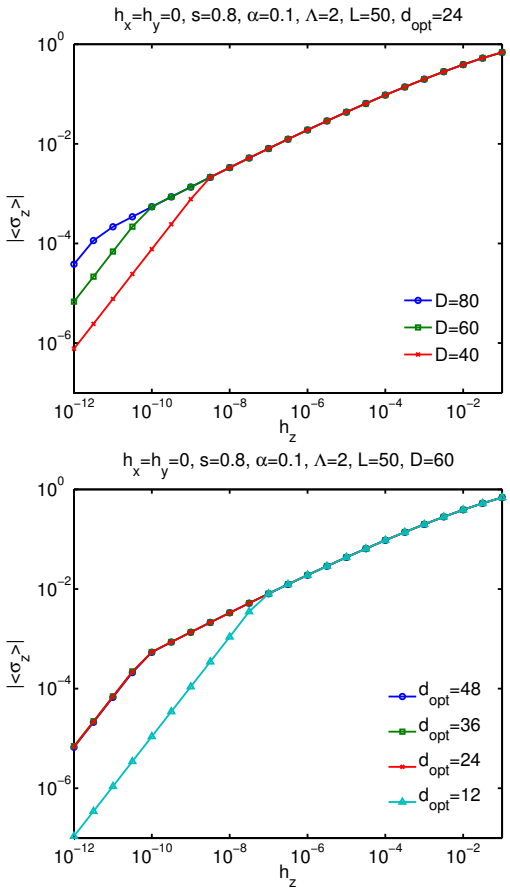

FIG. S4: Convergence check for the VMPS parameters D (a) and $d_{\rm opt}$ (b), for SBM2. The panels show the transverse-field response, $|\langle\sigma_z\rangle|$ vs. h_z in the CR phase, with a robust sublinear power law. The deviations at smallest fields arise from small symmetry-breaking effects in the numerics which cause a linear response akin to an ordered state.

III. OBB WITH EXPLICIT SHIFTS

The OBB scheme described in the preceding section allows us to easily perform calculations on a desktop computer using local boson bases of dimension $d_k \lesssim 10^4$. This can be increased by at least 6 more orders of magnitude by analytically incorporating explicit shifts during the construction of OBB. The idea is to explicitly shift the harmonic oscillator coordinates $\hat{x}_k$ by their equilibrium expectation values $\langle\hat{x}_k\rangle$ (similar in spirit to the procedure used in Ref. 11), such that the OBB can be used to capture the quantum fluctuations of the shifted coordinate

$$\hat{x}'_k = \hat{x}_k - \langle\hat{x}_k\rangle \ . \tag{S22}$$

We now describe explicitly how this is done.

We begin by noting that a shift corresponds to a unitary transformation

$$\hat{U}(\delta_k) = e^{\frac{\delta_k}{\sqrt{2}}(\hat{b}_k^\dagger - \hat{b}_k)} \tag{S23}$$

such that,

$$\hat{b}'_k \ = \ \hat{U}^\dagger(\delta_k)\,\hat{b}_k\,\hat{U}(\delta_k) = \hat{b}_k + \frac{\delta_k}{\sqrt{2}} \tag{S24}$$

on $\hat{b}_k$ (similarly for $\hat{b}_k^\dagger$). Thus the harmonic oscillator displacement $\hat{x}_k \equiv \frac{1}{\sqrt{2}}(\hat{b}_k + \hat{b}_k^\dagger)$ is shifted to $\hat{x}'_k = \hat{x}_k + \delta_k$, and the local boson number operator to

$$\hat{n}'_k \equiv \hat{b}'^\dagger_k \hat{b}'_k \ = \hat{n}_k + \delta_k \hat{x}_k + \tfrac{\delta_k^2}{2}. \tag{S25}$$

The shift can be implemented on the Hamiltonian level, by replacing the original Wilson-chain Hamiltonian by the shifted Hamiltonian

$$\mathcal{H}'^{(L)}_{\rm sb}(\hat{b}_{ki}, \hat{b}^\dagger_{ki}) = \mathcal{H}^{(L)}_{\rm sb}(\hat{b}'_{ki}, \hat{b}'^\dagger_{ki}) \ . \tag{S26}$$

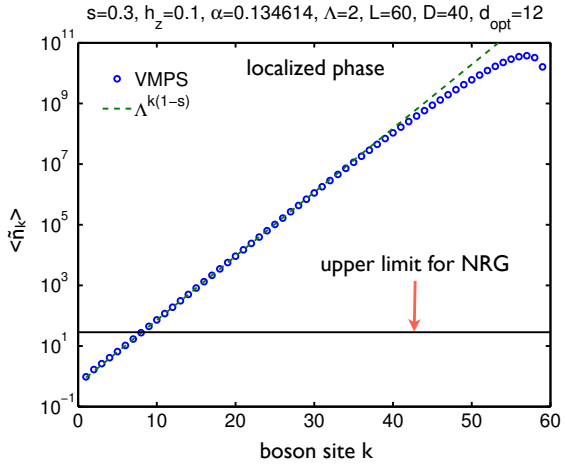

FIG. S5: Effective boson occupation number $\langle \hat{n}_k \rangle$ in the original, unshifted Wilson-chain boson basis, as function of site index k along the Wilson chain, calculated for the localized phase of SBM1. Dashed line indicates the relation $\langle \hat{n}_k \rangle \propto \Lambda^{k(1-s)}$ (see text). The finite size effect causes VMPS result deviate from this exponential relation at the end of the Wilson chain.

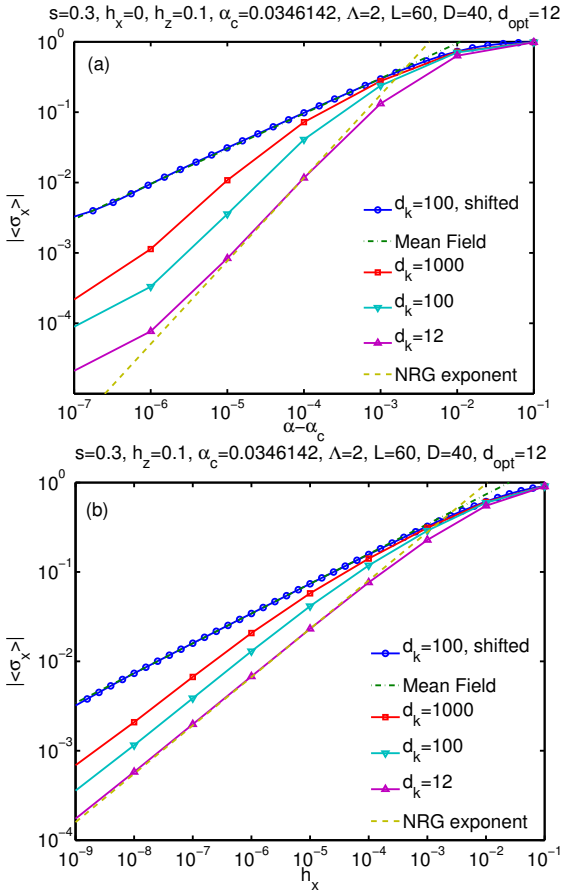

FIG. S6: The effect of Hilbert space truncation on the calculation of the SBM1 critical exponents β in (a) and δ in (b). The calculation labeled "$d_k = 100$, shifted" was performed using the OBB method with explicit shifts, without setting any maximum value for the size of the shifts, i.e. without restricting d_k^{eff}. Dashed straight lines correspond to power laws with exponents $\beta_{\text{NRG}} = 1.18$ and $\delta_{\text{NRG}} = 1.85$ obtained by NRG[13]. δ_{NRG} agrees with the hyperscaling exponent $\delta = (1+s)/(1-s)$ that applies for $s > 1/2$, see Sec. IV C below.[16]

The local states $|n_k\rangle$ in Eq. (S8) now represent Fock states of the shifted oscillators.

To incorporate explicit shifts within the OBB sweeping strategy described in the last section, we calculate the ground state expectation value $\langle \hat{x}_k \rangle$ of the current site after step (e). We then set $\delta_k = -\langle \hat{x}_k \rangle$ in Eqs. (S24) and (S25), thereby ensuring that the shifted coordinate $\hat{x}'_k$ corresponds to Eq. (S22). We subsequently move back to step (b) and implement the shift in the Hamiltonian. (In practice, it is convenient to preserve the form of the Hamiltonian itself, and instead to change the matrix representation of the operators $\hat{b}_k$, $\hat{b}_k^\dagger$ and $\hat{n}_k$ to implement the shift of Eq. (24).) Then we repeat the local update loop of the sequence (b), (c), (d), (e) (Fig. S2) until the shift converges. Finally, we move to step (f) and the next site.

The SBB method allows us to reach boson shifts $\langle \hat{x}_k \rangle$ so large that their description within the unshifted boson basis would require local dimensions of order $d_k^{\text{eff}} \simeq 10^{10}$, while nevertheless keeping the actual number of boson states in the *shifted* basis reasonably small, typically $d_k \lesssim 10^2$. A typical result for the resulting boson occupation numbers $\langle \hat{n}_k \rangle$ in the original, unshifted Wilson-chain boson basis is shown in Fig. S5, calculated in the localized phase. Since the boson shifts for the bosons in the original definition of SBM1 scale as[3] $\langle \hat{x}_k \rangle \simeq \omega_k^{(s-1)/2}$, with $\omega_k \propto \Lambda^{-k}$, we expect and indeed find that $\langle \hat{n}_k \rangle$ increases exponentially with k, as $\Lambda^{k(1-s)}$.

An accurate representation of this exponential rise, as achieved by our VMPS scheme, is essential for obtaining correct results for critical exponents. The detrimental effects of Hilbert space truncation are illustrated vividly in Fig. S6. It shows $\langle \sigma_x \rangle$ vs. $(\alpha - \alpha_c)$ for SBM1, calculated for several upper limits on the size d_k of the local boson basis. While the exponents obtained by NRG[13] (indicated by dashed lines) correspond to $d_k \leq 12$, the curves clearly change strongly as d_k is increased. Indeed, fully converged results are obtained only when the local boson basis can be taken to have "unlimited" size, as is the case for the explicit shifting strategy discussed above.

With the SBB method, the results for chain length $L = 60$ shown in this paper can be obtained within a few hours on a desktop computer. Note, though, that in the localized phase the total time needed for the calculation increases exponentially with L. The reason is that the converged value for the effective shift $\langle \hat{x}_k \rangle$ increases exponentially with k as

$$\langle \hat{x}_k \rangle \sim \Lambda^{k(1-s)/2}, \tag{S27}$$

as explained above. However, the "sweeping step size" for $\langle \hat{x}_k \rangle$, i.e. the change in this quantity from one sweep to the next, is limited, in effect, by the dimension d_k of the shifted local boson basis. Consequently, the number of sweeps needed to achieve convergence for $\langle \hat{x}_k \rangle$ increases exponentially with k (and making an informed initial guess for the requisite shift $\langle \hat{x}_k \rangle$ does not really help in speeding up its accurate determination).

For a given set of convergence criteria, the exponential growth in the shifts $\langle \hat{x}_k \rangle$ is accompanied by a similar growth in the absolute errors in their numerical determination. The consequences of this for SBM1 can be seen in Figs. S7(a) and S7(b), which show examples of the singular values r_q [Eq. (S20)] and $s_{\tilde{n}}$ [Eq. (S16)], respectively, as functions of the Wilson chain k: when k becomes large, the the lower end of the singular value shows an increasing amount of scatter. This implies that these singular values are not yet properly converged, which is directly correlated to the uncertainties in the oscillator shifts. Better convergence *can* be achieved by using stricter convergence criteria, as illustrated by Figs. S7(c) and S7(d), but only at a considerable increase in computation time, essentially using up to several hundreds of sweeps. We have thus adopted a compromise between accuracy and computation time: we chose D, $d_{\rm opt}$ and the shift convergence criteria such that throughout the entire Wilson chain, all discarded singular values were smaller than 10^{-5}, except possibly for an increase in this tolerance at the very end of the chain, of the type seen in Figs. S7(a) and S7(b). We have checked explicitly that not-optimally-converged shifts and singular values towards the end of the Wilson chain do not noticably affect the resulting physical quantities of interest, i.e. that these are already well converged nevertheless.

Interestingly, we have found that for SBM2 it is easier to obtain a well-converged shift in the localized phase than for SBM1, because the competition between the two chains causes the increase in oscillator shifts near the end of the Wilson chain to be much smaller for SBM2 than SBM1, as illustrated in Fig. S8. Near the chain's beginning, in contrast, the singular values for SBM2 were found to be bigger than for SBM1, but we nevertheless ensured throughout that only singular values below the 10^{-5} tolerance were discarded.

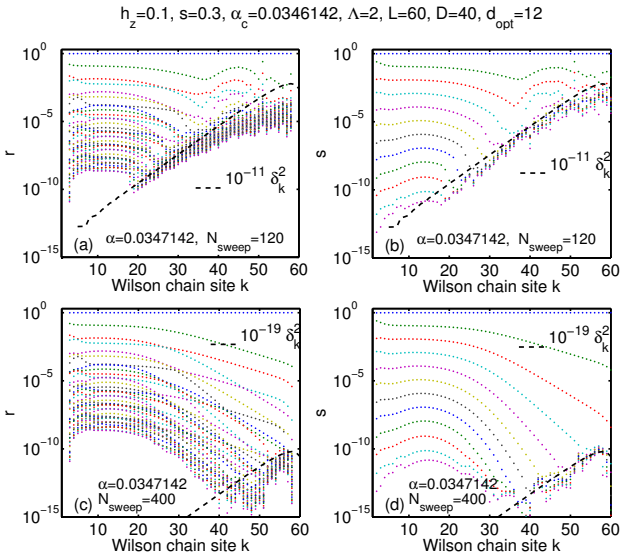

FIG. S7: Panels (a,c) and (b,d) show examples of the singular values r_q [Eq. (S20)] and $s_{\tilde{n}}$ [Eq. (S16)], respectively, as functions of the Wilson chain k, calculated in the localized phase of SBM1. Panels (c,d) show the same quantities as (a,b), but calculated using stricter convergence criteria requiring more sweeps, resulting in better-converged singular values [see discussion after Eq. (S27)]. The maximum value of $\langle \hat{n}_k \rangle$ in this example is of order 10^8, corresponding to a maximum shift $\langle \delta_k \rangle$ is of order 10^4. The diagonal dashed lines show the k-dependence of the shifts δ_k^2, multiplied by a constant prefactor that was chosen by hand in such a way that the dashed lines lie near the onset of noisiness at the lower end of the singular value spectra. This reveals the direct correlation between the exponential increase of δ_k^2, which directly enters the Hamiltonian, and the noise in the smallest singular values.

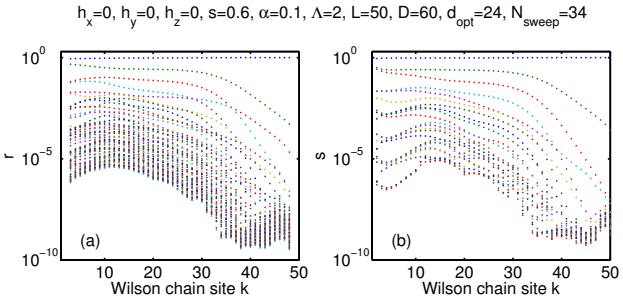

FIG. S8: Panels (a,b) show examples of the singular values r_q [Eq. (S20)] and $s_{\tilde{n}}$ [Eq. (S16)], respectively, as functions of the Wilson chain k, calculated in the localized regime of SBM2. For all the SBM2 parameters studied in this paper, the maximum effective boson occupation number $\langle \hat{n}_k \rangle$ is relatively much smaller than those we found in SBM1 ($\langle \hat{n}_k \rangle < 10^5$), which results a faster convergence of shift $\langle \delta_k \rangle$. In this typical example for SBM2, we get converged singular values already with $N_{\rm sweep} = 34$.

IV. ADDITIONAL RESULTS FOR SBM1

A. Determination of phase boundary

We have explored a number of different methods for determining the phase boundary between the localized and delocalized phases, all of which yield essentially equivalent results. (Fortunately, no oscillator-shift-related convergence problems occur in this context, since the oscillator shifts are essentially zero at the phase boundary.)

1. "Best power law". As mentioned in the main paper, our "standard method" for determining α_c has been

to tune it such that $\langle\sigma_x\rangle$ vs. $(\alpha_x - \alpha_c)$ yields the best straight line on a log-log plot. This turned out to be the most convenient way of getting accurate critical exponents.

2. Energy flow diagrams. In NRG, energy-flow diagrams[1] can be used to accurately determine the phase boundary of a quantum phase transition, since the degeneracies of low-lying levels typically differ for the two phases to be distinguished. It is possible to generate such energy-flow diagrams also within the VMPS approach[12], by calculating the eigenstates of the left block's Hamiltonian at each site when sweeping from left (large energy scales) to right (small energy scales), and then appropriately rescaling and shifting the resulting eigenenergies[1]. Details of this procedure and explicit examples of flow diagrams obtained in this manner will be presented elsewhere[4].

Energy-flow diagrams, however, are sensitive to relevant perturbations in terms of small numerical inaccuracies at large energies, i.e. early Wilson shells. This can lead to the artificial breaking of symmetries. For example, the Hamiltonian of SBM1 at $h_x = 0$ commutes with the parity operator

$$\hat{P} \equiv \sigma_x e^{i\pi\hat{N}}, \tag{S28}$$

where $\hat{N} = \sum_k \hat{b}_k^\dagger \hat{b}_k$ counts the total number of bosons on the entire Wilson chain. The corresponding parity symmetry guarantees that the ground state is two-fold degenerate. However, this degeneracy is typically broken by numerical inaccuracies, unless the symmetry is explicitly implemented in the numerical code. We have done so, and flow-diagrams resulting from a parity-symmetric version of our code yield α_c values in agreement with the "standard method" used in the main paper.

3. Diverging boson number. Another procedure for determining α_c is to plot the boson occupation number for all sites of the Wilson chain: a divergence of $\langle\hat{n}_k\rangle$ with Wilson-chain index k, as seen in Fig. S5, is a signature of the localized phase.

B. Critical exponents

Fig. S9 shows some typical data sets used to extract the critical exponents β and δ for $s < 1$ shown in Figs. 1c,d of the main text. This allows to assess the accuracy of the VMPS method in the quantum critical regime.

To properly describe the critical behavior, the Wilson chain must be long enough to resolve energy scales down to the scale $T_* \propto |\alpha - \alpha_c|^\nu$, which bounds the quantum critical regime[2]; here ν is the correlation-length exponent. Now, the lowest energy scale accessible for a bosonic Wilson chain of length L, i.e. $L-1$ boson sites, is Λ^{-L}. Thus, to determine α_c with an accuracy of, say, 10^{-a}, we need $\Lambda^{-(L-1)} \lesssim T_* \propto 10^{-a\nu}$, implying that the requisite chain length scales as

$$L \sim a\nu \frac{\ln(10)}{\ln\Lambda}\,. \tag{S29}$$

For SBM1, the correlation-length exponent becomes large for small s, see Fig. 5a of Ref. 2, and hence the requisite chain length increases with decreasing s, too. Together with Eq. (S27), according to which the largest shifts at the end of the chain scale as $\Lambda^{L(1-s)/2}$, this implies that in the localized phase, the sweep time needed to reach convergence increases exponentially as s decreases below 1/2.

For the above reasons, the data for $s = 0.2$ is clearly less accurate than for $s \geq 0.3$, as reflected by the error bars shown in Fig. 2c,d of the main text. The two extremal values that define the indicated error bars correspond to the two values of the exponent obtained by using only the upper or lower half of the full fitting interval that is indicated by vertical marks; the uncertainties from the straight power-law fit are somewhat smaller.

For $s = 1/2$, the transition is at its upper critical dimension and logarithmic corrections to the leading power laws are expected. As quantifying these corrections from the VMPS results is difficult, we have restricted ourselves to fits to effective power laws, which then naturally result in exponents slightly deviating from the mean-field values.

C. Hyperscaling

For SBM1, a scaling ansatz for the singular part of the free energy can be used[13] to derive a hyperscaling relation between the critical exponents δ and x, namely $\delta = (1+x)/(1-x)$. Here, x describes the divergence of the static susceptibility as $T \to 0$ at criticality, $\chi(T) \propto T^{-x}$ where $\chi = \partial\langle\sigma_x\rangle/\partial h_x$. Hyperscaling also implies $x = y$, where y characterizes the divergence of the zero-temperature dynamic susceptibility, $\chi(\omega) \propto \omega^{-y}$. Furthermore, $y = s$ is an exact result for the critical long-range Ising chain at all s (Refs. 14,15). This finally yields

$$\delta = \frac{1+s}{1-s} \tag{S30}$$

under the condition that hyperscaling is fulfilled, i.e., that no dangerously irrelevant operators spoils the naive scaling hypothesis. For the Ising chain, this applies below the upper critical dimension, i.e., for $s > 1/2$, while a dangerously irrelevant operator appears for $s < 1/2$. Consistent with the expectations from QCC, our δ-values follow the hyperscaling prediction (S30) for $s > 1/2$ (see Fig. 2d of main text).

V. ADDITIONAL RESULTS FOR SBM2

A. Determination of phase boundaries

Below we describe several approaches that we have found useful for determining the various phase boundaries of SBM2. For convencience, these boundaries are illustrated schematically in Fig. S10.

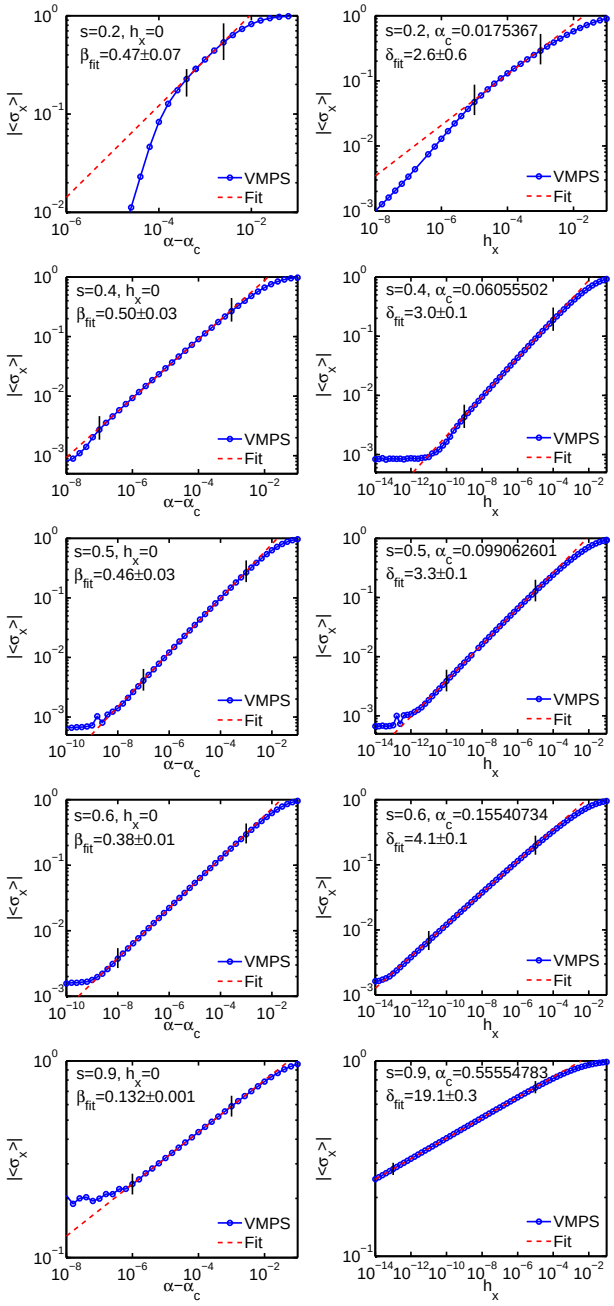

FIG. S9: The left and right columns show some of the VMPS results used to determine the SBM1 exponents β and δ that are shown in Fig. 1c) and 1d) of the main text, respectively. We used $h_z = 0.1$, $\Lambda = 2$, $L = 60$, $D = 40$, $d_{\rm opt} = 12$. The main text (Eq. (S29)) explains why the range of pure power-law behavior is smaller for $s = 0.2$ than for larger s-values.

1. Order parameter. Measurements of the order parameter $\langle\sigma_{x,y}\rangle$ of the localized phase can be used to determine the critical field h_z^α that defines the location of the L-D boundary at finite h_z. This is demonstrated in Fig. S11 for $s = 0.6$ and $\alpha = 0.1$. The method of "best power laws" is then suitable to obtain accurate values for

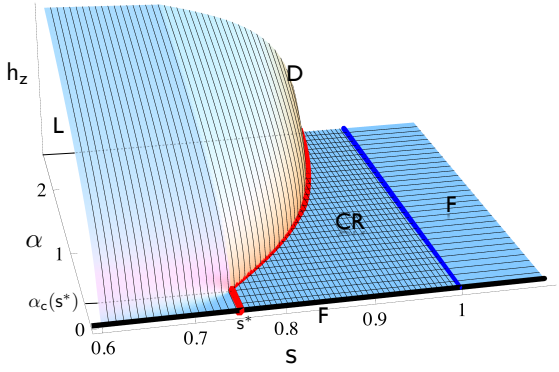

FIG. S10: Schematic sketch of the SBM2 phase diagram as function of s, α and h_z. The localized phase (L) lies below the curved surface representing the critical field $h_z^{\rm c}(s,\alpha)$, the delocalized phase (D) above and to its right. (The curved surface was not calculated, but is an artist's impression.) The cross-hatched area in the $h_z = 0$ plane represents the critical phase (CR). Its phase boundary with the localized phase (L) is marked by the thick red line in the $h_z = 0$ plane (corresponding to the red line in main text, Fig. 3a), consisting of a straight line between the points $(s^*, 0)$ and $(s^*, \alpha_{\rm c}(s^*))$, and a curved portion representing the line $\alpha_{\rm c}(s)$, for $s^* < s < 1$. The thick blue line at $s = 1$ is the CR-F phase boundary to the free phase (F). The thick black line at $\alpha = h_z = 0$ likewise represents a free spin (F).

$h_z^{\rm c}$ as well as corresponding critical exponents – we leave this for a future study.

Notably, the inherent instability of the CR phase, combined with numerical errors of VMPS, renders difficult the accurate determination of the CR-L phase boundary at $\vec{h} = 0$. In particular, a direct observation of the order parameter as function of α or s leads to sizeable uncertainties.

2. Transverse-field response. The zero-field phase boundary CR-L is most accurately extracted via the response to a small transverse field, $\langle\sigma_z\rangle(h_z)$. The stable L phase responds linearly, while the CR phase responds with a non-trivial sublinear power-law, see Eq. (S32) below – those can be easily distinguished, as shown in Fig. 3b of the main paper. Indeed, by studying the transverse-field response for small α and $0.7 \le s \le 0.8$, we are able to determine the value of the universal critical "dimension" s^* to be 0.75 ± 0.01, as shown in Fig. S12.

The accurate determination of s^* requires the numerical results to be reliable down to transverse fields as small as $h_z \simeq 10^{-14}$. Such precision is achievable, in principle, by using sufficiently large D and $d_{\rm opt}$, as follows from Fig. S4. However, such a brute force approach is computationally demanding. A more efficient strategy is to exploit parity symmetry: For $h_x = h_y = 0$ the SBM2 Hamiltonian commutes with the parity operator

$$\hat{P}_z \equiv \sigma_z e^{i\pi\hat{N}}, \tag{S31}$$

where $\hat{N} = \sum_k \hat{b}_{kx}^\dagger \hat{b}_{kx} + \sum_k \hat{b}_{ky}^\dagger \hat{b}_{ky}$ counts the total num-

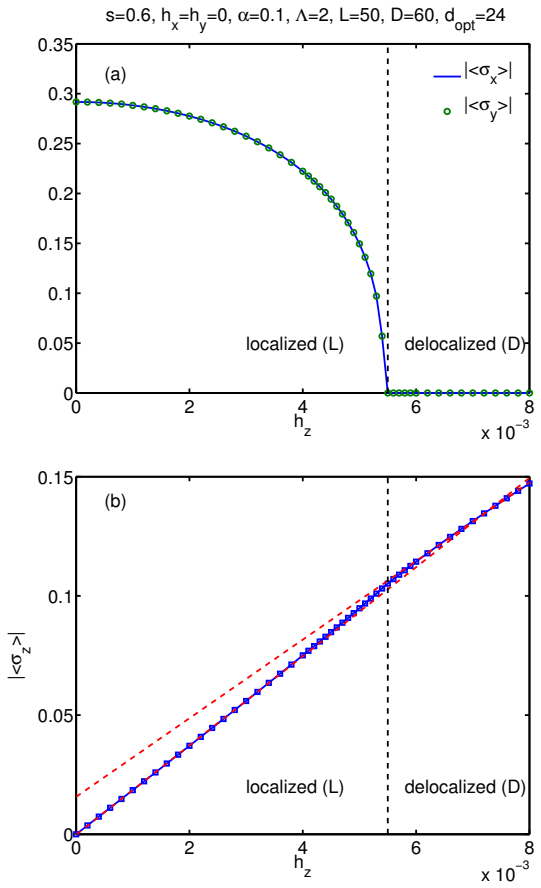

FIG. S11: (a) Order parameter $|\langle\sigma_{x,y}\rangle|$ for the L-D transition, driven to zero by increasing the transverse field h_z past the critical value $h_z^{\rm c}$ (indicated by black dashed line). (b) Correspondingly, the transverse-field response of $|\langle\sigma_z\rangle|$ shows a slight kink, indicating the higher-order singularity expected at the L-D transition. As in Fig. 3 of the main paper, the linear response of the L phase is clearly visible. We observe a small breaking of the XY symmetry of SBM2 in the L phase due to numerical errors, in that the order parameter in panel (a) prefers configurations with $|\langle\sigma_x\rangle| = |\langle\sigma_y\rangle|$, instead of exploring the full rotational symmetry.

ber of bosons on the entire Wilson chain. Thus, the ground state has a parity degeneracy. In fact, this degeneracy is the main source of numerical error for small h_z when using a VMPS code that does not account for parity symmetry, since then the degeneracy is lifted by numerical noise (similarly to the SBM1 case). By implementing this parity symmetry explicitly in the code, we were able to achieve the required precision (much better than in Fig. S4), while using choices for D and $d_{\rm opt}$ that were not unreasonably large, as shown in Fig. S12.

3. Diverging boson number and flow diagram. We have also explored alternative ways for determening the L-CR phase boundary, based on monitoring the the divergence of the boson number per site at the end of the chain,

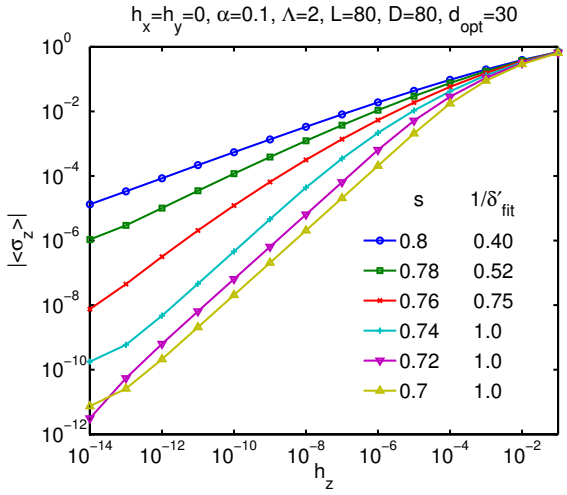

FIG. S12: Transverse-field response for SBM2, $|\langle\sigma_z\rangle|$ vs. h_z, used to determine the L-CR phase boundary. The fitting exponent δ' is defined in Eq. (S33), and the fitting range is $h_z \in [10^{-12}, 10^{-8}]$. From the transition between a linear response for $s < s^*$ and a sublinear power law for $s > s^*$, we estimate s^* to lie between 0.74 and 0.76. To reduce numerical noise, the curves were calculated using a VMPS ground state that also was an odd eigenstate of the parity operator $\hat{P}_z$ of Eq. (S31).

or analyzing NRG-like flow diagrams (as discussed for SBM1). We have found these methods to be computationally much cheaper than studying the transverse-field response, while yielding results of comparable accuracy for the L-CR phase boundary.

B. Properties of the critical phase

The CR phase corresponds to a partially screened (or fractional) spin, with non-trivial power-law autocorrelations of the components of $\vec{\sigma}$. In ground-state calculations, those can be probed by measuring the response to an applied field: The linear-response susceptibility at $T = 0$ is infinite, and the non-linear response is of power-law character,

$$\langle\sigma_{x,y}\rangle \propto h_{x,y}^{1/\delta}, \quad \langle\sigma_z\rangle \propto h_z^{1/\delta'}, \tag{S32}$$

with $\delta, \delta' > 1$. A standard renormalized perturbation expansion around the free-spin fixed point results in[17]

$$\begin{aligned} 1/\delta &= \frac{1-s}{2} + \mathcal{O}([1-s]^2), \\ 1/\delta' &= 1 - s + \mathcal{O}([1-s]^2)\,. \end{aligned} \tag{S33}$$

In Figs. S13 we show numerical VMPS data for the non-linear response for several sets of parameters inside the CR phase. We indeed find the expected power laws over a sizeable range of fields; the power laws are cut off at small fields by the influence of numerical errors, like

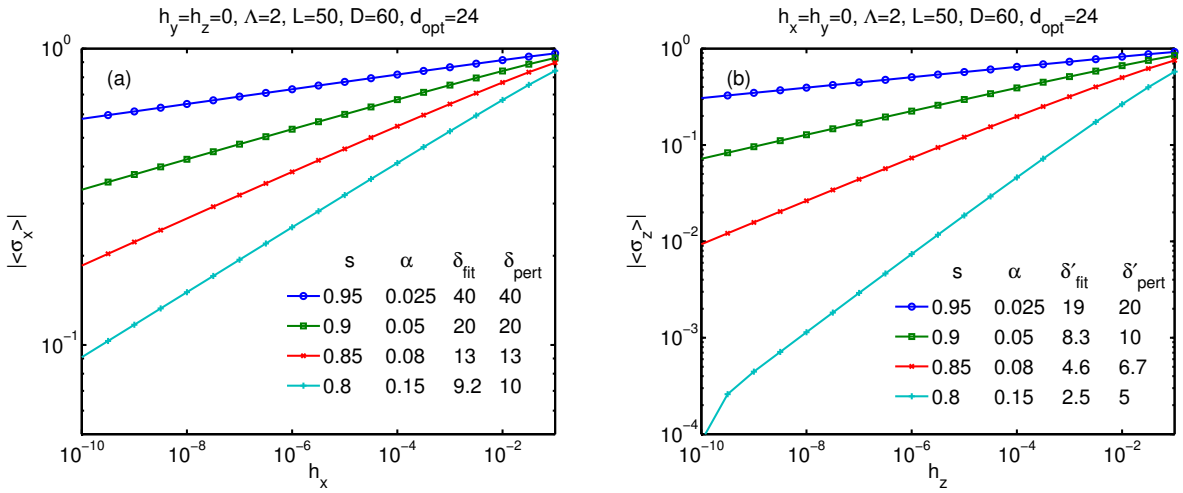

FIG. S13: Non-linear response *inside* the CR phase. We find power law behavior as expected from Eq. (S32). For each s, we chose an α-value close to the α^* fixed-point value, to ensure that the asymptotic power law is reached quickly (i.e. without the need for h_x to become extremely small). Using the fitting range between 10^{-9} and 10^{-2}, we find values for the exponents $\delta_{\rm fit}$ and $\delta'_{\rm fit}$ in excellent agreement with the values $\delta_{\rm pert}$ and $\delta'_{\rm pert}$ expected from Eq. (S33), as indicated in the legends.

the breaking of the XY symmetry of the model or the generation of a small transverse field. From the data we can extract exponents δ and δ' as function of s. Comparing the resulting exponents to the perturbative prediction (S33), we find that the agreement is excellent, considering that (i) for s very close to unity the asymptotic regime is difficult to reach, due to the slow flow of α, and (ii) for larger $(1-s)$ the second-order terms in Eq. (S33) (i.e. two-loop corrections) will become important.

C. RG flow near s^*

Fig. 4 of the main text shows the RG flow of SBM2 in the two cases (a) $s^* < s < 1$ and (b) $0 < s < s^*$. In case (a) the CR phase is stable for small α and $\vec{h} = 0$, whereas this phase is absent in case (b). In the following we briefly discuss the evolution of the RG flow from case (a) to case (b), as this is related to a *discontinuous* jump of the phase boundary upon varying s.

As described in the main text, the fixed points CR and QC1 of case (a) approach each other upon lowering s, such that they meet at $s = s^*$ and both disappear for $s < s^*$. This follows from the absence of the CR phase in case (b) and the fact that both are intermediate-coupling fixed points for $s < 1$ (i.e. they have to meet at finite α). The merger of the two fixed points also implies that the flow lines to the left and right of CR in Fig. 4a merge. As a result, the RG flow line which lead from F via CR to D in case (a) now becomes a flow line from F to QC2 in case (b). For the phase boundary of the L phase (thick line in Fig. 4) this means that its starting point on the $h_z = 0$ axis jumps from a finite value (corresponding to QC1) in (a) to zero in (b) once s is lowered past s^*.

We note that the merger and disappearance of two fixed points upon variation of a "dimension" d is not unusual. For instance, upon approaching the lower critical dimension d_c^- of a magnet from above, the critical fixed point typically approaches the trivial fixed point describing the ordered phase, such that both merge at $d = d_c^-$ and disappear for $d < d_c^-$. Here the evolution of the phase boundary is continuous. What is unusual about SBM2 is that two *intermediate-coupling* fixed points merge and disappear, causing the discontinuous behavior. The only other example with similar physics we are aware of is in the two-channel Anderson/Kondo impurity model with power-law density of states $\propto |\omega|^r$, where a critical fixed point merges with a stable non-Fermi liquid fixed point at some critical dimension $r_{\rm max}$, with a consequent jump in the phase diagram.[18,19]

[1] K. G. Wilson, Rev. Mod. Phys. **47**, 773 (1975); R. Bulla, T. Costi, and T. Pruschke, Rev. Mod. Phys. **80**, 395 (2008).
[2] R. Bulla, N. Tong, and M. Vojta, Phys. Rev. Lett. **91**, 170601 (2003).
[3] R. Bulla, H. Lee, N. Tong, and M. Vojta, Phys. Rev. B **71**, 045122 (2005).
[4] C. Guo, A. Weichselbaum, J. von Delft, and M. Vojta, to be published.
[5] R. Žitko and T. Pruschke, Phys. Rev. B **79**, 085106 (2009).
[6] L. N. Oliveira, Braz. J. Phys **22**, 155 (1992).
[7] S. R. White, Phys. Rev. Lett. **69**, 2863 (1992).
[8] C. Zhang, E. Jeckelmann, and S. R. White, Phys. Rev.

Lett. **80**, 2661 (1998).
[9] A. Weiße *et al.*, Phys. Rev. B **62**, R747 (2000).
[10] Y. Nishiyama, Eur. Phys. J. B **12**, 547 (1999).
[11] A. Alvermann and H. Fehske, Phys. Rev. Lett. **102**, 150601 (2009).
[12] H. Saberi, A. Weichselbaum, and J. von Delft, Phys. Rev. B **78**, 035124 (2008).
[13] M. Vojta, N. Tong, and R. Bulla, Phys. Rev. Lett. **94**, 070604 (2005).
[14] M. E. Fisher, S. K. Ma, and B. G. Nickel, Phys. Rev. Lett. **29**, 917 (1972).
[15] M. Suzuki, Prog. Theor. Phys. **49**, 424 (1973); **49**, 1106 (1973); **49**, 1440 (1973).
[16] M. Vojta, arXiv:1201.4922 (2012).
[17] L. Zhu and Q. Si, Phys. Rev. B **66**, 024426 (2002); G. Zarand and E. Demler, Phys. Rev. B **66**, 024427 (2002).
[18] C. Buxton and K. Ingersent, Phys. Rev. B **57**, 14254 (1998).
[19] I. Schneider, L. Fritz, F. B. Anders, A. Benlagra, and M. Vojta, Phys. Rev. B **84**, 125139 (2011).

4.2 Additional results on determining α_c and critical exponents

As shown in the previous section, using VMPS with an optimal boson basis allows us to calculate the correct critical exponents of SBM1. A prerequisite to obtain a better precision of the critical exponents is an accurate phase boundary α_c. There the number of local boson states is not so crucial as compared to the calculation of the critical exponents. This fact is highlighted in Fig. 4.1 and Fig. 4.2. In these two figures I plot the boson occupation along the Wilson chain for several parameters approaching the phase boundary in the localized phase of SBM1. We can see that the closer to the phase boundary the less local boson states are required. Nevertheless even for $\alpha - \alpha_c = 10^{-7}$, the required local dimension (of $\sim 10^3$) is still out of the capability of NRG, which only allows for a few dozen local states.

The parameters which are important when determining α_c is the VMPS matrix dimension D and the Wilson chain length L. Near the critical point, the entanglement in the system becomes larger, therefore we need VMPS matrices of a higher dimension to represent the system accurately. I will discuss this in more detail in Sec. 4.8.

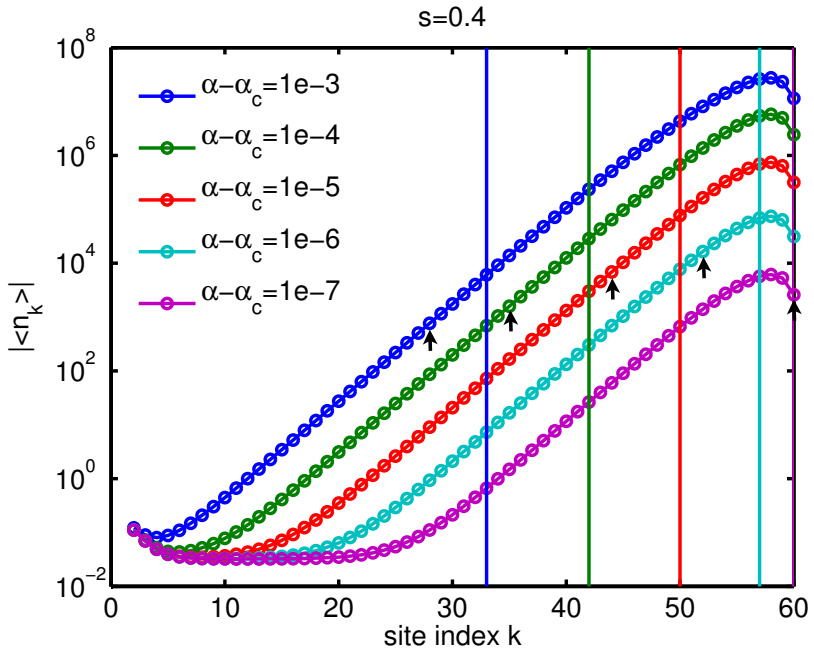

Figure 4.1: The boson occupation $\langle n_k \rangle$ for five values of $\alpha - \alpha_c$ in the localized regime (chosen from the "fitting range" used to extract the exponent β from $\langle \sigma_x \rangle \propto (\alpha - \alpha_c)^\beta$), at $\epsilon = 0$. For each choice of $\alpha - \alpha_c$, the vertical lines of corresponding color indicates the Wilson chain length, L_{min}, needed to get $\langle \sigma_x \rangle$ accurate to within 1%. The arrow at each curve gives $T^* = (\alpha - \alpha_c)^{1/s}$. Other parameters used are $h_z = 0.1$, $\Lambda = 2$, $L = 60$, $D = 40$ and $d_{opt} = 12$.

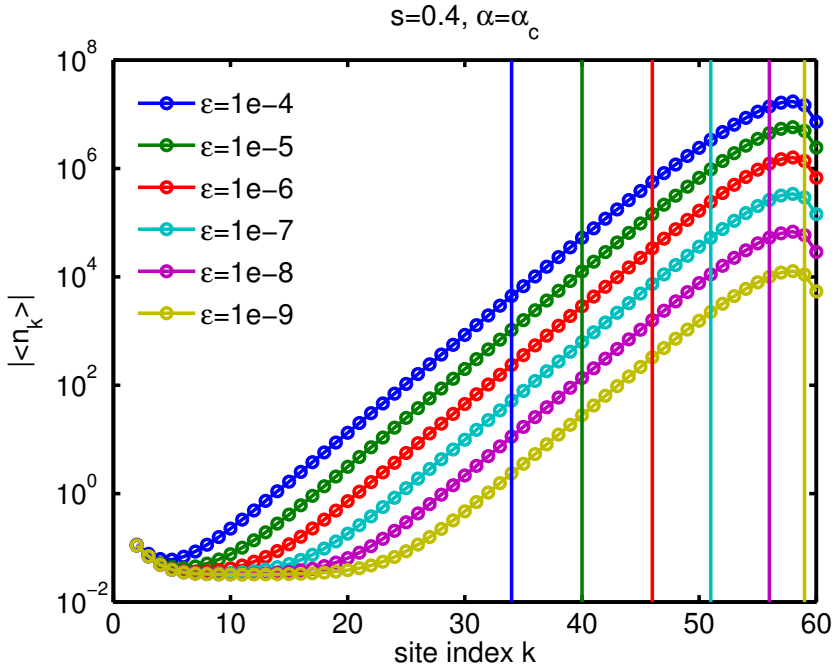

Figure 4.2: Same as Fig. 4.1 except for several different ϵ at $\alpha = \alpha_c$, which is calculated at $\epsilon = 0$.

Fig. 4.1 and Fig. 4.2 also show the importance of L on the accuracy of the phase boundary. Take Fig. 4.1 for example. The vertical lines indicate the shortest possible Wilson chain length L_{min} that one can use to obtain $\langle\sigma_x\rangle$ with no more than 1% error for different $\alpha - \alpha_c$. L_{min} is obtained by varying L and comparing the resulting $\langle\sigma_x\rangle$ with the converged $\langle\sigma_x\rangle$ value. The arrows at each curve give the characteristic energy scale [12]

$$T^* = (\alpha - \alpha_c)^{1/s}. \tag{4.1}$$

Fig. 4.1 shows that L_{min} is closely related to T^* and should be larger than T^* to capture the correct physics. We can also see that for $\alpha - \alpha_c = 10^{-7}$ the chain length $L = 60$ is not long enough anymore. To calculate a more accurate α_c one needs a longer Wilson chain. Also note that at $L = 60$, given $\Lambda = 2$ the energy scale of the last Wilson chain site is around machine precision 10^{-16}. Therefore, an arbitrary precision tri-diagonalization algorithm is required to generate the Wilson chain Hamiltonian parameters. Table. 4.1 shows values for α_c we calculated with different L for several s.

4.3 Exploration of the power-law discretization

Besides the optimal boson basis, we have also investigated the power-law discretization to solve the diverging boson problem in the localized phase of sub-Ohmic spin-boson model. Though this approach was not successful, it sheds some light on the nature of the problem

s	α_c (L=100)	α_c (L=50)
0.2	0.017530557(1)	0.01752(2)
0.3	0.0346138682(1)	0.034611(2)
0.4	0.06055502016(1)	0.0605550(3)
0.5	0.09906260074(1)	0.0990626(1)
0.6	0.15540734375(5)	0.15540735(5)
0.7	0.2376563245(5)	0.2376563(1)
0.8	0.3600551395(1)	0.3600551(1)
0.9	0.5555478304(1)	0.555546(2)

Table 4.1: α_c of SBM1 obtained with $L = 100$ and $L = 50$ for several different s. Other parameters used here are $h_z = 1$, $\Lambda = 2$, $D = 40$ and $d_{opt} = 12$. For some s one can still get better precision with L=100 than those listed above. I just did not push to the limit.

and eventually led us to the optimal boson basis approach. Therefore I will include some results here.

The Hamiltonian of SBM1 is:

$$H_{SBM1} = H^{loc} + \sum_q \left[\omega_q \hat{B}_q^\dagger \hat{B}_q + \lambda_q \frac{\sigma_x}{2}(\hat{B}_q^\dagger + \hat{B}_q)\right], \tag{4.2}$$

where

$$H^{loc} = -\frac{h_x}{2}\sigma_x - \frac{h_z}{2}\sigma_z. \tag{4.3}$$

The standard power-law spectral function of the bosonic bath is

$$J(\omega) = 2\pi\alpha\omega_c^{1-s}\omega^s \qquad \text{with} \quad s \geq 0\ , \tag{4.4}$$

where ω_c is the energy cutoff. We set $\omega_c = 1$ in this thesis. The definition of the spectral density is:

$$J(\omega) = \sum_j \lambda_j^2 \delta(\omega - \omega_j)\ , \tag{4.5}$$

$$= \int \frac{d\omega'}{\Delta(\omega')}\lambda^2(\omega')\delta(\omega - \omega') = \frac{\lambda^2(\omega)}{\Delta(\omega)}\ , \tag{4.6}$$

where $\Delta(\omega_j) = \omega_j - \omega_{j+1}$ is the spacing between subsequent frequencies. (Following NRG-convention, ω_j decreases with increasing j). We take $\Delta(\omega) \sim \omega^\beta$. When $\beta = 1$, it describes the logarithmic discretization used in NRG, with $\beta > 0$ the power-law discretization.

To achieve the standard power-law spectral function Eq. (4.4), we evidently need to choose $\lambda^2(\omega) \sim \omega^{s+\beta}$. Now, for a given spin state, an oscillator with frequency ω is shifted by (e.g. see Eq. (37) of Ref.[11]):

$$\delta(\omega) \sim \frac{\lambda(\omega)}{\omega}\langle\sigma_z\rangle \sim \omega^{(s+\beta-2)/2}\ . \tag{4.7}$$

Note here δ is the shift not the $\delta-$function. For the sub-Ohmic SBM1 ($s < 1$) and logarithmic discretization ($\beta = 1$), this shift diverges as $\omega \to 0$ which causes the breakdown of NRG calculation in the localized regime.

To contain the diverging shift, we may choose

$$\beta = 2 - s, \tag{4.8}$$

which results in a constant shift δ even for $\omega \to 0$. As we only consider the sub-ohmic/ohmic regime where $0 < s < 1$, this implies $\beta > 1$. On the other hand, for Ohmic case, $s = 1$, we need $\beta = 1$, as in standard NRG.

To find the discretization points $\{\omega_i\}$, we solve the following equations iteratively

$$\omega_i - \omega_{i+1} = (\frac{\omega_i + \omega_{i+1}}{2})^\beta \tag{4.9}$$

with $\omega_0 = \omega_c$. After we get ω_i, we use Eq. (S2) in the supplementary information in the previous section to evaluate the terms in the star Hamiltonian, followed by the numerical mapping onto the chain Hamiltonian.

Since the characteristic energy scale at iteration j decreases more slowly for power law discretization than for standard NRG, the NRG truncation scheme will presumably not be reliable. However, DMRG-truncation can be expected to work as it is a variational method.

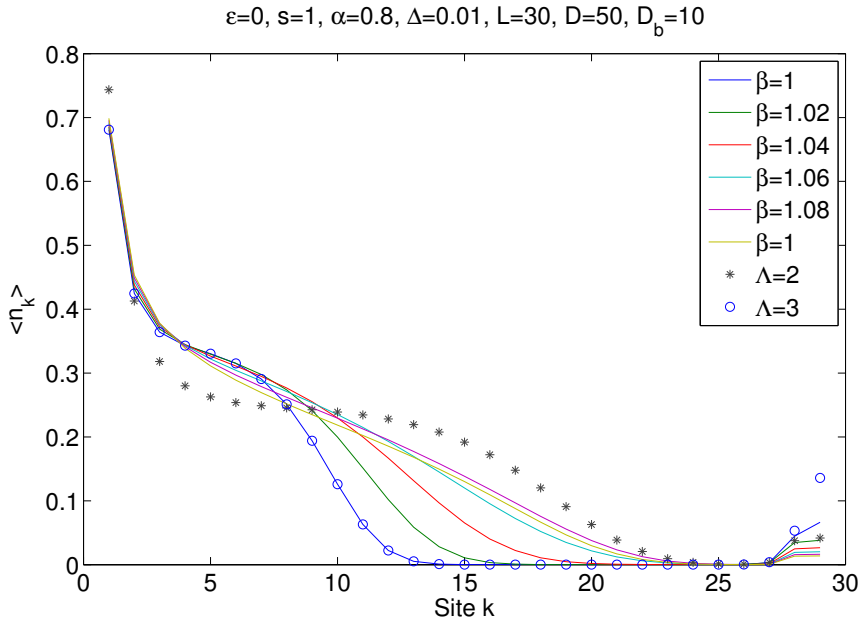

Figure 4.3: Boson number expectation values for Ohmic SBM1 calculated with power and logarithmic discretization. The power law discretization with $\beta = 2 - s = 1$ is equivalent to the logarithmic discretization with $\Lambda = 3$.

We first compare the power discretization with logarithmic discretization for the Ohmic case $s = 1$. Using Eq. (4.8), $\beta = 1$ and Eq. (4.9) becomes

$$\omega_{i+1} = \frac{1}{3}\omega_i. \tag{4.10}$$

which is exactly a logarithmic discretization with $\Lambda = 3$. Fig. 4.3 confirms this.

Fig. 4.4 shows $\langle n_k \rangle$ in the localized phase ($\alpha > \alpha_c$) and delocalized phase ($\alpha < \alpha_c$). Compared to logarithmic discretization, we no longer have the boson number divergence problem, so we can use a small local boson basis. For the parameter used in Fig. 4.4, with $d_k \equiv D_b = 10$ the data is already converged. Furthermore $\langle n_k \rangle \to 0$ when $k \to \infty$ for power discretization which is compatible with the boundary condition $\langle n_{end} \rangle = 0$.

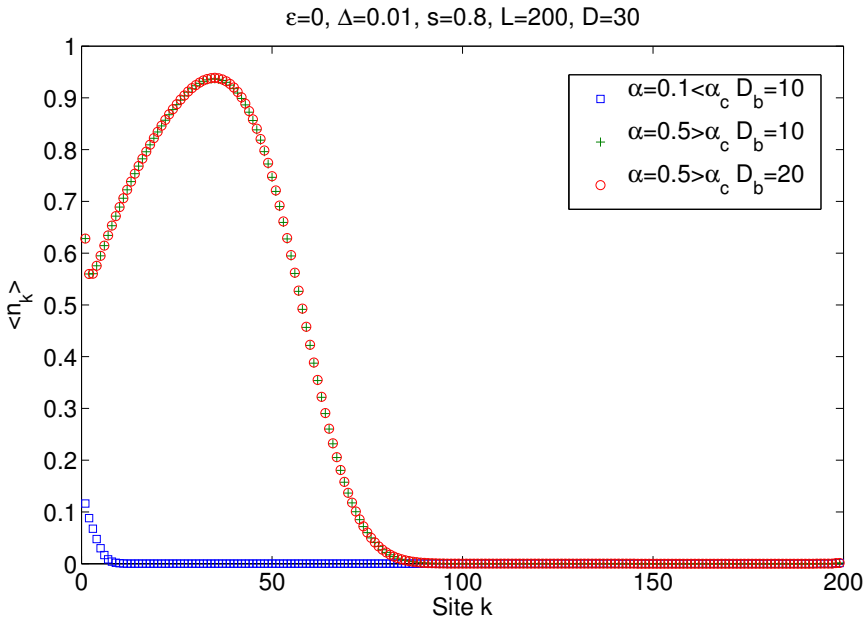

Figure 4.4: Boson number expectation value $n_k = \left\langle b_k^\dagger b_k \right\rangle$ on site k of localized and delocalized phases using power law discretization using Eq. (4.3). (Note that in this plot D_b is the symbol for the local boson dimension.)

Like Λ for the logarithmic discretization, β in the power discretization is the parameter that describe how we discretize the band. Any physical results should be stable with respect to β. Fig. 4.5 analyzes the dependence of the critical coupling α_c around $\beta = 2 - s$. The plots here show that the phase boundary α_c depends on the discretization around $\beta = 2 - s$. Also note that α_c here is slightly different with NRG results.

More importantly, as the relevant physical energy scales can be extremely small near the phase boundary, in the case of power-law discretization, one has to use extremely long chain to resolve these. Therefore power-law discretization does not solve the divergence of local boson degree of freedom problem, but rather transforms it to the divergence of chain length problem. This led us to believe that the divergence problem could not be

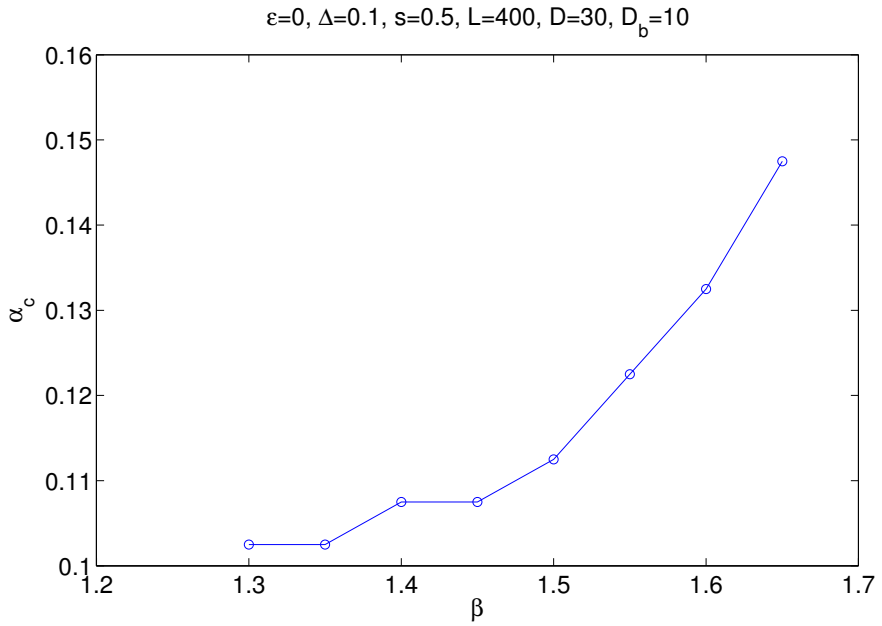

Figure 4.5: The dependence of Critical coupling α_c on β for $s = 0.5$.

circumvented by using some special discretization scheme, and one has to deal with the divergence directly (for example using the optimal boson basis).

4.4 Dynamical determination of the local dimension

Another scheme we have tried before we use the shift basis scheme is to solve the diverging boson basis problem with brute force. Diverging boson basis requires larger and larger d_k for sites with lower and lower energy scale. We do not have any prior knowledge about the relation of the energy scale and the boson occupation of a site. (Indeed for SBM we could use mean field prediction and obtain the relation like Eq. (4.7). There are two reasons why we did not use this relation. First, the main aim of the project is that we want to compare VMPS results with mean field results therefore we should not use any mean field assumption in our calculation. Second, we want the method to be general and behave like a black box algorithm. Therefore we should not include any model specific property into the algorithm.) To find the appropriate d_k one could perform several test runs with different d_k, then find the proper d_k by checking on convergence. However, a more efficient way is to adjust the number of local states of each boson site dynamically during the sweep. This only uses big d_k on those sites towards the end of the Wilson chain where it is necessary. Thus dynamical determination of the local dimensions is much faster than using the same big d_k for all sites.

Even though this brute force approach does not work as efficient as the shift basis scheme, it still works and can generate good enough results to reach the same conclusion

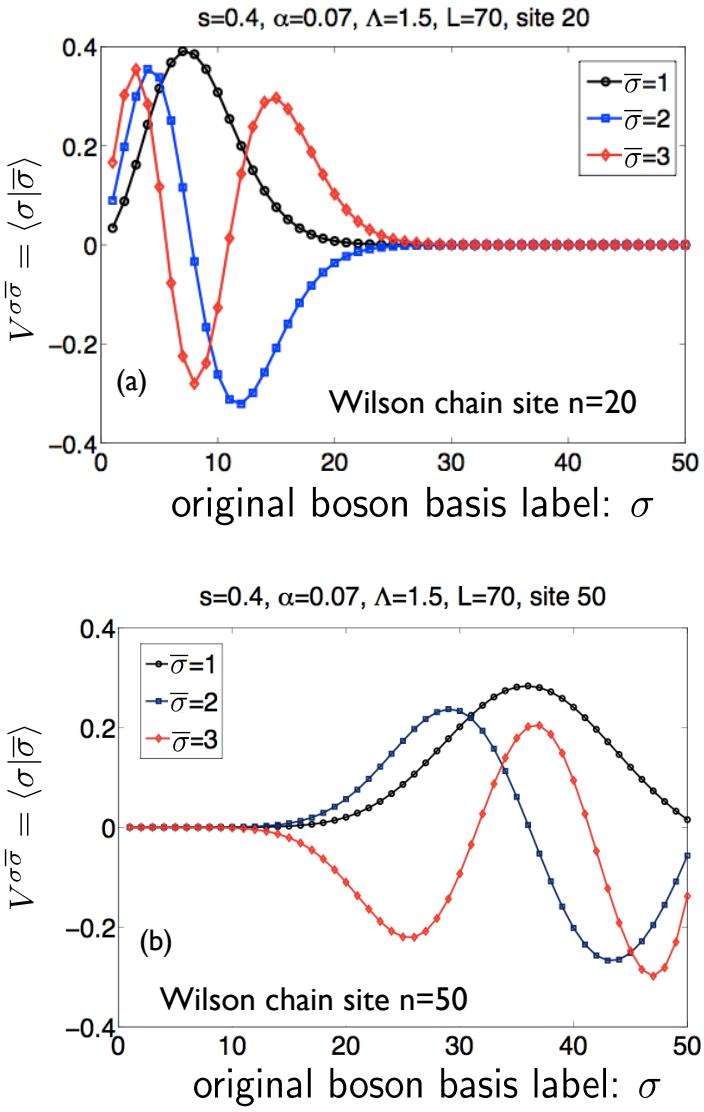

Figure 4.6: The wave function of the optimal boson states represented in the original boson basis $|\bar{\sigma}\rangle = \sum_{\sigma=1}^{50} V^{\sigma\bar{\sigma}}|\sigma\rangle$, where $|\sigma\rangle$ and $|\bar{\sigma}\rangle$ are the original and optimal boson basis respectively. We plot the first three optimal boson states for site: (a) $k = 20$, (b) $k = 50$. The results is obtained in the localized regime of SBM1.

about the SBM1 critical point as in our paper. On the other hand, sometimes the main reason to use big local basis is not due to a large oscillator shift (big $\langle x\rangle^2$) but because the variance of x ($\langle x^2\rangle - \langle x\rangle^2$) is big. In this case, the big local basis cannot be significantly reduced by just using a shifted basis, and one has to represent the basis directly with brute force as discussed in the following.

The procedure I choose is inspired by observing the wave function of the optimal boson states on different sites as shown in Fig. 4.6. For some sites like the one showed in Fig. 4.6(a), $d_k = 50$ is already large enough to cover the span of the first three optimal

orbits. For other sites like the one shown in Fig. 4.6(b), most weight of the optimal wave functions are distributed on high boson occupation Fock states indicating that we need a larger d_k to cover the whole optimal boson states.

By balancing simplicity and accuracy, I choose the "relative" position of the peak of the first optimal boson state p_k to indicate whether or not d_k should be increased. The definition of p_k is

$$p_k \equiv \frac{a_{peak}}{d_k}, \tag{4.11}$$

where a_{peak} is the position of the peak of the first optimal boson state. If p_k is larger than a certain threshold, say 25%, I will increase d_k. The number of states we need to add should increase with both p_k and d_k, so we simply add a_{peak} more states to d_k. Numerically this is done by expanding the dimension of V-matrix by adding a_{peak} rows of zeros.

Fig. 4.7 shows the boson occupation and the dynamically determined d_k on the boson sites. We choose a point in the delocalized regime not far from the phase boundary. Still the maximum of d_k is above 10000 in the explicit absence of bosonic shifts, which is impossible to calculate in NRG. Also note that 10^4 is about the largest d_k I can calculate on a typical PC. We can increase the effective maximum d_k to 10^{10} if we use the shift boson basis scheme.

4.5 The folded chain setup of SBM2

One way to represent SBM2 as a one-dimensional chain is to put the two Wilson chains on the left and right side of the spin respectively, as shown in Fig 4.8.

This setup is not valid in NRG as it is not compatible with energy scale separation. For VMPS, in principle, this is not a problem. The VMPS sweeping procedure would simply first start from one tail of one Wilson chain (say from the very left side) and sweep to the spin, then continue to the tail of the other Wilson chain (the very right side) and sweep back to the starting tail.

However there is a problem with the setup in Fig 4.8 when we want to calculate the ground state properties for the symmetrical coupling case $\eta_x = \eta_y = \eta$. The screening of the spin is frustrated, and the ground state becomes very sensitive to a small asymmetry of the couplings. Therefore the symmetry should be perfectly preserved during VMPS calculation. If we put the two chains on different sides of the spin and sweep from one side to the other, the sweeping procedure itself will introduce a small numerical asymmetry which prevents the algorithm to converge to the actual ground state.

In order to perfectly preserve the $\eta_x = \eta_y = \eta$ symmetry, we must follow the NRG prescription: we fold the two chains to one side and combine two bosons on each chain into a super site, then we define a new set of local boson operators

$$A_k = b_{kx} \otimes I, \tag{4.12}$$
$$B_k = I \otimes b_{ky}, \tag{4.13}$$

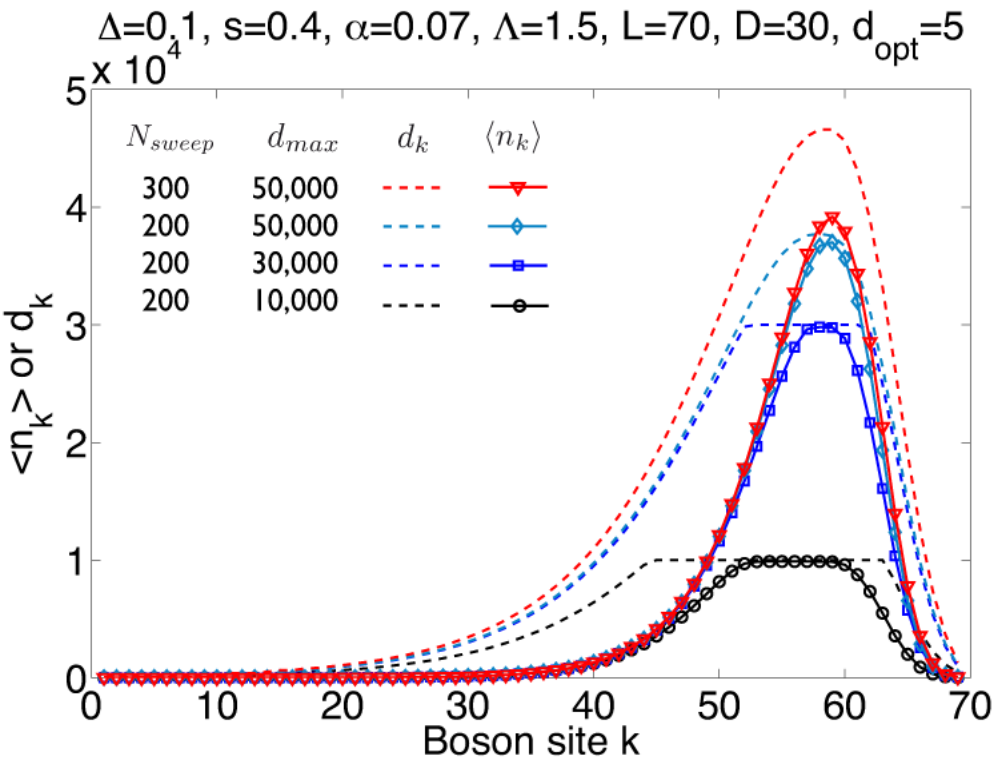

Figure 4.7: The boson occupation (solid lines with symbols) and dynamically determined d_k (dashed lines) of the boson sites. d_{max} is the upper limit of d_k set by hand to show the effect of limiting d_k. N_{sweep} is the number of VMPS sweeps. The results is obtained in the localized regime of SBM1.

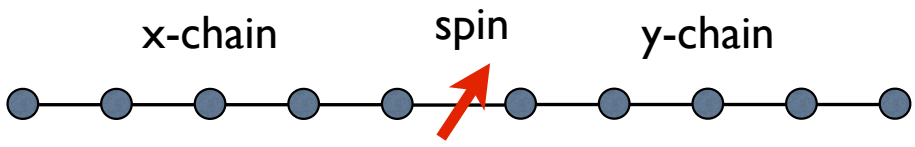

Figure 4.8: Two channel setup for SBM2 with the Wilson chains positioned left and right of the spin. The symmetry of the two chains cannot be perfectly kept when we sweep from one side to the other.

where I is the identity matrix of the same size as a_k and b_k. Now the Hamiltonian is

$$H_{folded} = H^{loc} + \sqrt{\frac{\eta}{\pi}}\left[\frac{\sigma_x}{2}(A_1 + A_1^\dagger) + \frac{\sigma_y}{2}(B_1 + B_1^\dagger)\right] + \sum_{k=1}^{L-2}\epsilon_k(A_k^\dagger A_k + B_k^\dagger B_k) + \sum_{k=1}^{L-2} t_k(A_k^\dagger A_{k+1} + B_k^\dagger B_{k+1} + h.c.). \quad (4.14)$$

Note that the difference between Eq. (4.14) and Eq. (4.22) below is that A_k and B_k are defined in the same Hilbert space while b_{kx} and b_{ky} are not. The transformation is illustrated in Fig. 4.9. The price for this transformation is that the local state space dimension is squared. For example if for one chain the local number of degree is d_k then for the super site it is d_k^2. In practice, we found that the number of local states one needs to keep is still within the control of our method.

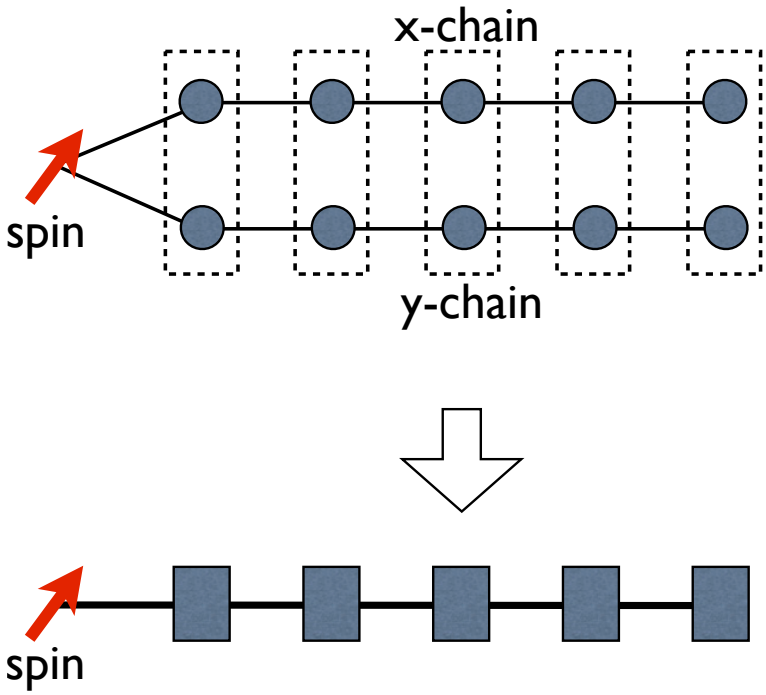

Figure 4.9: Preferred two-channel setup in the presence of channel symmetry: two Wilson chains lie on the same side of the spin. Each site in the x-chain is combined with the corresponding site in the y-chain to make a super site. The geometry is the same with SBM1 after this transformation. The symmetry of the two chains can be preserved with this folded chain setup.

4.6 Symmetries

4.6.1 Parity symmetry

Both SBM1 and SBM2 can have parity symmetries with proper aligned external field. This can be verified with both the original Hamiltonians or the Wilson chain form Hamiltonians. The Wilson chain form Hamiltonian of SBM1 is

$$H^c_{SBM1} = -\frac{h_x}{2}\sigma_x - \frac{h_z}{2}\sigma_z + \sqrt{\frac{\eta}{\pi}}\frac{\sigma_x}{2}(b_1 + b_1^\dagger) + \sum_{k=1}^{L-2} t_k(b_k^\dagger b_{k+1} + h.c.) + \epsilon_k \hat{n}_k \ , \quad (4.15)$$

where $\hat{n}_k = b_k^\dagger b_k$, with eigenvalue n_k, counts the number of bosons on site k. The parity operator is defined as

$$P_z = \sigma_z e^{i\pi \hat{N}}, \quad (4.16)$$

where $\hat{N} = \sum_k b_k^\dagger b_k$ is the total boson number operator of the Wilson chain. It is straightforward to verify the following relations:

$$P_z^\dagger P_z = P_z P_z^\dagger = 1, \quad (4.17)$$

$$P_z^\dagger \sigma_x P_z = -\sigma_x, \quad (4.18)$$

$$P_z^\dagger b_k P_z = -b_k, \quad (4.19)$$

Therefore when $h_x = 0$ we have

$$P_z^\dagger H^c_{SBM1} P_z = H^c_{SBM1}, \quad (4.20)$$

This implies that the Hamiltonian in Eq. (4.15) commutes with the parity operator P_z:

$$[P_z, H^c_{SBM1}] = 0, \ (h_x = 0). \quad (4.21)$$

There are two independent parity symmetries in SBM2. The SBM2 Wilson chain Hamiltonian is

$$\begin{aligned} H^c_{SBM2} = & -\frac{h_x}{2}\sigma_x - \frac{h_y}{2}\sigma_y - \frac{h_z}{2}\sigma_z \\ & + \sqrt{\frac{\eta_x}{\pi}}\frac{\sigma_x}{2}(b_{1x} + b_{1x}^\dagger) + \sum_{k=1}^{L-2} t_{kx}(b_{kx}^\dagger b_{k+1,x} + h.c.) + \epsilon_{kx}\hat{n}_{kx} \\ & + \sqrt{\frac{\eta_y}{\pi}}\frac{\sigma_y}{2}(b_{1y} + b_{1y}^\dagger) + \sum_{k=1}^{L-2} t_{ky}(b_{ky}^\dagger b_{k+1,y} + h.c.) + \epsilon_{ky}\hat{n}_{ky} \ . \end{aligned} \quad (4.22)$$

We can define the following parity operators:

$$P_z = \sigma_z e^{i\pi \hat{N}} = \sigma_z e^{i\pi \hat{N}_x + \hat{N}_y}, \quad (4.23)$$

$$P_x = \sigma_x e^{i\pi \hat{N}_y}, \tag{4.24}$$

$$P_y = \sigma_y e^{i\pi \hat{N}_x}, \tag{4.25}$$

where $\hat{N}_x = \sum_k b_{kx}^\dagger b_{kx}$ and $\hat{N}_y = \sum_k b_{ky}^\dagger b_{ky}$. Note that only two of these three parity operators are independent as

$$P_z = -iP_xP_y. \tag{4.26}$$

Similar with SBM1 the following commutation relation can be verified:

$$[P_z, H_{SBM2}^c] = 0, \ (h_x = h_y = 0) \tag{4.27}$$

$$[P_x, H_{SBM2}^c] = 0, \ (h_y = h_z = 0) \tag{4.28}$$

$$[P_y, H_{SBM2}^c] = 0, \ (h_x = h_z = 0) \tag{4.29}$$

4.6.2 Symmetry breaking in VMPS ground state

Even though SBM Hamiltonians have certain symmetries such as parity, the ground state we obtained from VMPS does not necessarily preserve it. Let's take the parity symmetry in SBM1 for example. P_z commuting with H_{SBM1} means that for any ground state $|G\rangle$, $P_z|G\rangle$ is also a ground state. Therefore the ground state of H_{SBM1} will be either a eigenstate of P_z or it is two-fold degenerate and any linear combination of these two states is a ground state too.

If the ground state $|G\rangle$ is not degenerate then it will be parity eigenstate satisfying

$$P_z|G\rangle = p_z|G\rangle \tag{4.30}$$

$p_z = \pm 1$ is the eigenvalue. The expectation value of σ_x (and σ_y) with respect to any parity eigenstates are 0. This can be easily proved as

$$\begin{aligned} \langle G|\sigma_x|G\rangle &= \langle G| - P_z^\dagger \sigma_x P_z|G\rangle \\ &= -p^2\langle G|\sigma_x|G\rangle \\ &= -\langle G|\sigma_x|G\rangle, \end{aligned} \tag{4.31}$$

therefore

$$\langle G|\sigma_x|G\rangle = 0. \tag{4.32}$$

According to definition the system is in the delocalized regime. Consequently, the localized phase must be double degenerate.

When the ground state is double degenerate, within the ground state subspace there are two special sets of states. One set of ground states $|G_+\rangle$ and $|G_-\rangle$ are the eigenstates of the parity operator P_z:

$$P_z|G_\pm\rangle = \pm|G_\pm\rangle \tag{4.33}$$
$$H_{SBM1}|G_\pm\rangle = E_g|G_\pm\rangle \tag{4.34}$$

Another set of ground states are

$$|G_\uparrow\rangle \equiv \frac{\sqrt{2}}{2}(|G_+\rangle + |G_-\rangle) \tag{4.35}$$
$$|G_\downarrow\rangle \equiv \frac{\sqrt{2}}{2}(|G_+\rangle - |G_-\rangle) \tag{4.36}$$

The special property about this set of ground states is that they have the largest possible expectation value of $\langle\sigma_x\rangle$. This can be verified by VMPS calculations. A rigorous analytical proof is left for future study. A curious fact about this set of ground states is that the VMPS code without explicit implementing parity symmetry always yields these ground states. Based on the nature of VMPS we expect these ground states have the least internal entanglement. The symmetry breaking is most strongly seen also in the energy flow diagram, where at some specific energy scale the finite size spectrum changes drastically. Analytical verification of this fact is still lacking.

It is also intriguing to ask which ground state exists in nature. If we do a measurement of σ_x we will always result in $|G_{\uparrow\downarrow}\rangle$. However, this does not mean the ground state before the measurement is $|G_{\uparrow\downarrow}\rangle$ because a wave function collapse may have happened during the measurement. Then the interesting question is why the wave function collapse prefers the states with least internal entanglement. Even if there is no wave function collapse, it is still a question why nature prefers the states with least internal entanglement. This should not be confused with environment-caused decoherence. We treat the spin and the boson bath as a whole system, and the entanglement in concern include the entanglement between the spin and the bath and the entanglement between different parts of the bath. Therefore, the ground state we get in nature is the least entangled state and cannot be explained as a results of environment-caused decoherence. Understanding this in more detail would be an interesting topic for further studies.

4.6.3 Implementation of parity symmetry

In the previous section I explained that the ground state obtained from VMPS is not a parity eigenstate in the localized regime. However one can implement parity symmetry explicitly in the VMPS algorithm to obtain the ground state which is also the parity eigenstate in the localized regime. This is useful when one wants to generate a clean flow diagram.

Parity symmetry is a special case of the Abelian symmetry, so one can use the same method of implementing Abelian symmetry to implement parity symmetry. Two points

are worth to mention here. First, the parity for the local boson basis is the parity of its occupation number. To define the parity for the spin basis one should use the eigenstates of the spin operator in the parity operator. For example for SBM1, the eigenstates of σ_z are used as the basis and the two parities are assigned to the two states respectively. After having defined the parity of each local state, the states of the same parity are combined, therefore all operators will be 2×2 block matrices. Second, one can define the right vacuum state as even parity then the parity of the wave function is defined by the left vacuum state. The rest of the implementation is along the lines as described for example in the Section 5.1 of Ref. [57].

The expectation value $\langle\sigma_x\rangle$ of P_z parity eigenstates is always 0. If one wants to recover the expectation value of the non-parity eigenstates in the localized regime, one can simply calculate

$$\begin{aligned}\langle G_\uparrow|\sigma_x|G_\uparrow\rangle &= \frac{1}{2}(\langle G_+|\sigma_x|G_+\rangle + \langle G_-|\sigma_x|G_-\rangle + \langle G_+|\sigma_x|G_-\rangle + \langle G_-|\sigma_x|G_+\rangle) \\ &= Re(\langle G_+|\sigma_x|G_-\rangle) \end{aligned} \tag{4.37}$$

4.6.4 U(1) symmetry in SBM2

For SBM2, besides the parity symmetry, there is also an Abelian U(1) symmetry. The generator is

$$S = \frac{1}{2}\sigma_z + i\sum_k (b^\dagger_{y,k} b_{x,k} - b^\dagger_{x,k} b_{y,k}) \tag{4.38}$$

It is straight forward to verify that

$$[H, S] = 0 \tag{4.39}$$

At the moment when the thesis was written we were still investigating the influence of U(1) symmetry to the VMPS numerics. We have indications that the numerics breaks the U(1) symmetry in the critical regime where the ground states should preserve the U(1) symmetry. This results in the nonzero $\langle\sigma_x\rangle$ and $\langle\sigma_y\rangle$ in the critical regime for both non-parity code (Fig. 4.10) and parity code (Fig. 4.11) results of SBM2. Explicitly implementing of U(1) symmetry in the VMPS code appears necessary to get improved results. Work along those lines is currently in progress.

4.7 Energy flow diagrams

In NRG, the energy flow diagram provides lots of information about an impurity system. For example, the phase boundary of the quantum phase transition can be fixed accurately with the flow diagram. This is very important when calculating the critical exponents at the phase boundary.

We can generate something similar to the flow diagram with VMPS by calculating the eigenstates of the left block's Hamiltonian at each site when we sweep from left to right

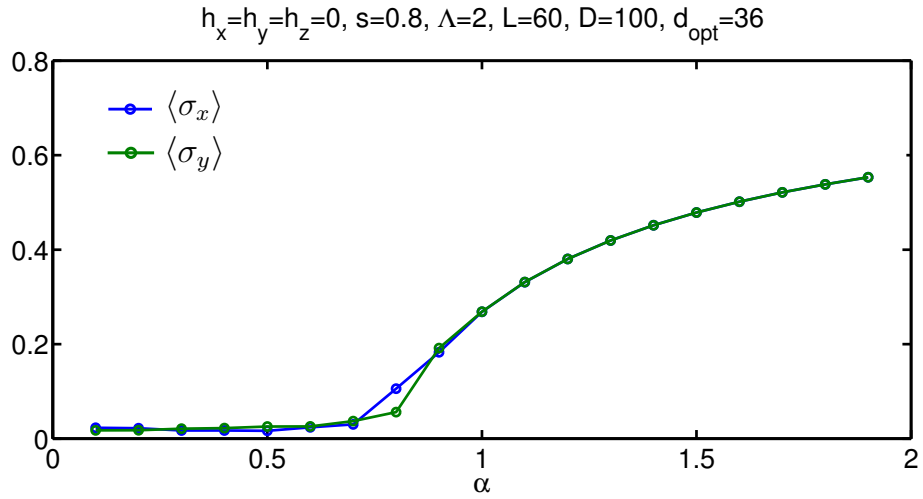

Figure 4.10: $\langle\sigma_x\rangle$ and $\langle\sigma_y\rangle$ calculated with the SBM2 non-parity code. The system is in the critical regime for $\alpha < 0.8$ however we still see small non-zero values which is probably caused by the fact that the VMPS code breaks the U(1) symmetry. (Another possible reason is the finite size effect.)

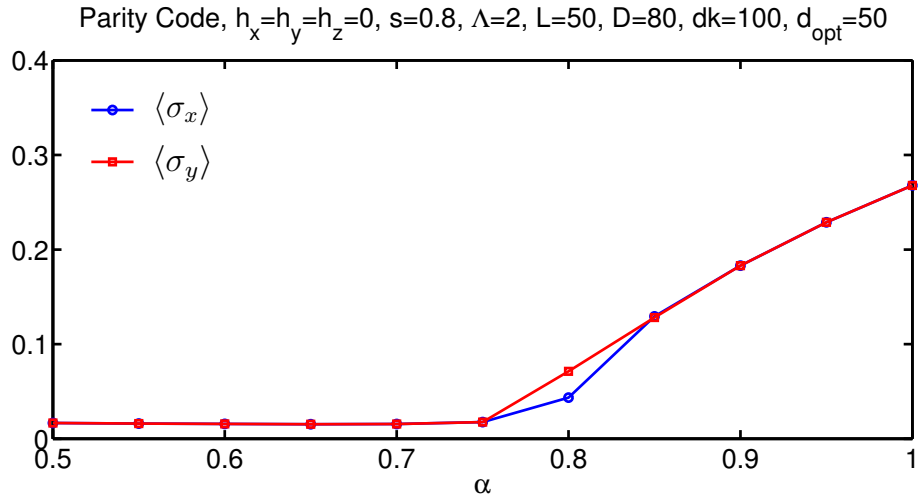

Figure 4.11: Same as Fig. 4.10 except using the parity code and a bit larger D and shorter L. We still see the non-zero $\langle\sigma_x\rangle$ and $\langle\sigma_y\rangle$ in the critical regime. This indicates that it is caused by symmetry breaking other than the parity symmetry.

[74, 70]. I call it "the quasi flow diagram". By comparison, we find the quasi-flow diagram is very close to the flow diagram in the delocalized regime and near the phase boundary, especially at the lower part of the energy spectrum. The larger D we use, the better the quasi-flow diagram we get before we reach the machine precision. To fix the phase boundary a few low lying states are already sufficient.

Fig. 4.12 shows the quasi flow diagram in the delocalized regime, on the phase boundary and in the localized regime. One can compare them with the flow diagram in Ref. [12].

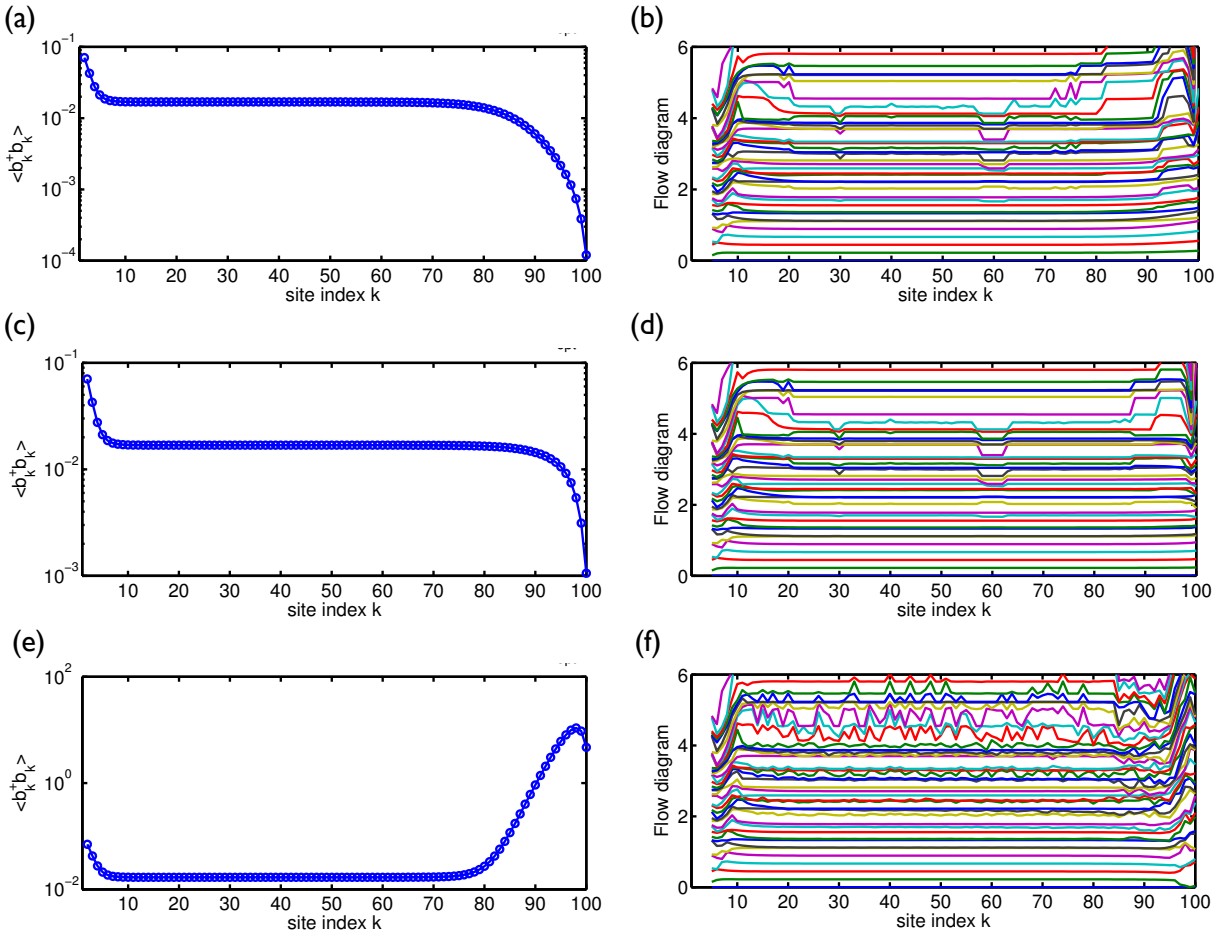

Figure 4.12: The boson occupation number (a),(c), (e) and flow diagrams (b),(d),(f) generated after we implemented the parity symmetry in our program. The results are calculated at $s = 0.3$ for SBM1. (a), (b) In the delocalized regime close to the phase boundary where $\alpha = 0.0346138680$; (c), (d) On the phase boundary $\alpha = \alpha_c = 0.0346138682$; (e),(f) In the localized regime close to the phase boundary where $\alpha = 0.0346138683$.

With these quasi flow diagrams we can fix the critical α_c for a given s with a relative accuracy better than 10^{-8}. If one wants to improve the accuracy one needs a longer Wilson chain as explained in Sec.4.2.

There is another very tricky problem to use VMPS to generate flow diagram, due to the degeneracy from the parity symmetry of the spin-boson model. Unlike NRG, the variational nature of VMPS does not preserve parity symmetry, and the degeneracy of the ground states will sometimes cause unstable "jumps" in the flow diagram. To eliminate this instability, one has to implement parity symmetry explicitly in the VMPS program as described in the previous section.

4.8 MPS block entropy

With the singular values defined in Eq. (S16) and Eq. (S20) in Section 4.1 we can define two von Neumann entropies S_A and S_V to describe the entanglement in the system:

$$S_A = -\sum_q r_q^2 \ln r_q^2, \tag{4.40}$$

$$S_V = -\sum_{\tilde{n}} s_{\tilde{n}}^2 \ln s_{\tilde{n}}^2, \tag{4.41}$$

where r_q and $s_{\tilde{n}}$ are normalized singular values satisfying

$$\sum_{\tilde{n}} s_{\tilde{n}}^2 = 1, \tag{4.42}$$

and

$$\sum_q r_q^2 = 1. \tag{4.43}$$

S_A is the block entropy that describes the entanglement between the left and right part of the chain. S_V is the local entropy of the optimal boson basis.

The MPS block entropy can tell us whether the bond dimension D and the dimension of optimal boson basis d_{opt} are large enough. More specifically, if these dimensions are big enough to account for the entanglement in the system, S_A and S_V will change negligibly with increasing D and d_{opt} as the entropies are already converged. On the other hand, if we see substantial reduction of the entropies after increasing the dimensions we know that the number of dimensions used before is not big enough.

Even with fixed matrix dimensions, the MPS block entropies can be used as a local convergence indicator in addition to global convergence criterion like the variance of the ground state energies calculated at each site during one sweep.

Fig. 4.13 shows examples of S_A of SBM1. As expected, we see the biggest entanglement entropy with α near the phase boundary. Since only global convergence criterion with respect to energy was used local convergence on every site cannot be guaranteed. This accounts for the numerical noise in the localized regime though the influence on the physical properties of the spin is negligible. In the next section I will describe further improvement of the algorithm which not only provides a more sensible convergence criterion, but also runs several times faster.

4.9 Convergence criterion and further improvement of the algorithm

Like standard VMPS, the VMPS convergence criterion I used to generate results in our paper were based on the variance of the global ground state energy E_k calculated at each

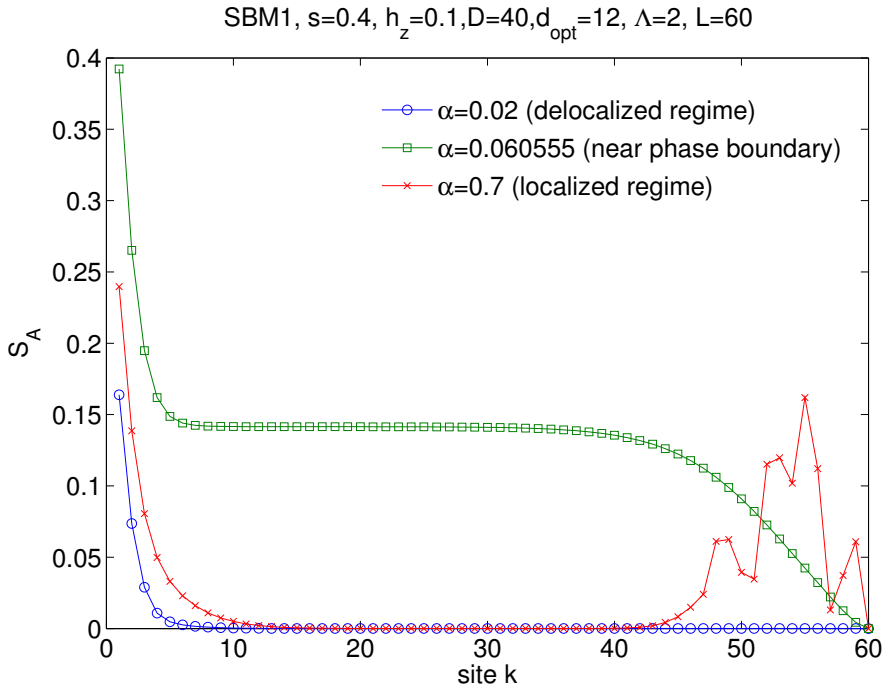

Figure 4.13: The MPS block entropy S_A of the delocalized regime with α near the phase boundary. The convergence criterion used here only requires the variance of the ground state energy calculated at each site during one sweep $var(E)$ is smaller than 10^{-14} which corresponds to a Wilson chain length of $k \propto 45$. This is why we still see not fully converged data for $k > 45$ at the end of the chain for the localized case though its influence on the calculated physical properties of the spin is negligible.

site $k \in [0, L]$ in unrescaled units during one sweep.

$$var(E_k) = \frac{std(E_k)}{|\frac{1}{L}\sum_k E_k|}. \tag{4.44}$$

Here L is the Wilson chain length, and $std(E_k)$ is the standard deviation

$$std(E_k) = \sqrt{\frac{1}{L-1}\sum_k (E_k - \bar{E})^2}. \tag{4.45}$$

where $\bar{E}$ is the average of E_k. If $var(E_k)$ is smaller than $\epsilon_E = 10^{-14}$ the sweeping will be stopped. Nevertheless, such a convergence criterion is not exactly compatible with the Wilson chain setting when the chain length corresponds to an energy scale that is much smaller than ϵ_E (e.g. see Fig 4.13 and Fig 4.14). The following improvement of the algorithm incorporates local convergence criterion which solves this problem.

From Fig. 4.13 we can see that except near the phase boundary the entanglement varies a lot along the Wilson chain. Therefore, instead of using fixed D and d_{dop} for all boson

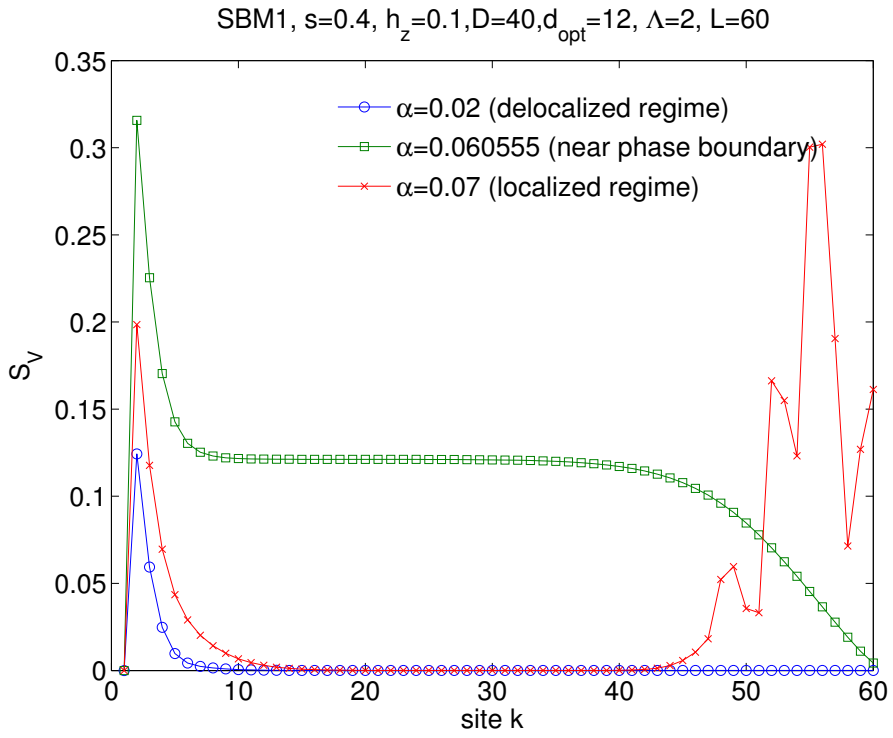

Figure 4.14: The MPS block entropy S_V (same otherwise as Fig. 4.13).

sites, one should adopt D_k and d_{opt}^k for each site. For the deep localized and delocalized case shown in Fig. 4.13, for example, we just need very small matrix dimensions except at the beginning of the Wilson chain. This indeed speeds up the calculation which becomes several times faster than the previous implementation as described in Sec. 4.1.

The criterion that one can use to determine what is a proper D_k and d_{opt}^k is to check the converged singular values. If the smallest singular value s_{min}^k or r_{min}^k is larger than a certain maximum threshold (λ_{max}) then one should increase the dimension, on the other hand if it is smaller than the minimum threshold (λ_{min}) one should reduce the dimension D_k and d_{opt}^k. Also note that there are more systematic and more complicated generic DMRG procedures for truncation [107], but what is described here turns out sufficient.

For a given set of fixed D and d_{opt} if one sweeps enough times, the converged MPS block entropy on all sites will be obtained. However this is also time-consuming and not necessary. The reason is if the dimension at the beginning of the Wilson chain is too small then the error caused by this insufficient dimension will be large compare to the energy scale of the remaining sites in the Wilson chain. Therefore I use a scheme which expand the dimension gradually from the beginning of the Wilson chain to the end.

I call the site after which I stop adjusting the dimensions k_l, thus l is the length of the part of the Wilson chain in which the singular values of the site are converged. Another related site $k_{l'}$ is the site after which the energy scale is much smaller than $var(E_k)$ of the last sweep and therefore the information of these sites should not be used. In other words,

the Wilson chain sites after l' does not need to be include in the optimization.

k_l is determined by examining the relative change of the MPS block entropy from two consecutive sweeps for the sites before $k_{l'}$. When the relative change is less than 1%, the singular values of the site is considered as converged, and the furthest such site from the beginning of the Wilson chain is k_l. The dimension D_k and d^k_{opt} of all sites $k \leq k_l$ will be adjusted to adapt to the MPS block entropy S^k_A and S^k_V. The improved algorithm is summarized as follows:

1. At the beginning of the calculation a random starting VMPS with small dimensions like $D = 10$ and $d_{opt} = 6$ for all sites is generated.

2. After each sweep calculate k_l and pause sweeping when k_l is no longer changing.

3. Check the singular values of each site with $k \leq k_l$. If the smallest singular value s^k_{min} or r^k_{min} is larger than λ_{max}(e.g. 10^{-6}), the dimension of D_k or d^k_{opt} is increased by 20% (or based on the ratio between the smallest singular value and λ_{max}). The states associated with those singular values smaller than the threshold λ_{min} (e.g. 10^{-8}) are discarded. Note that when expanding or truncating the matrices, old matrix elements (or part of, in the case of truncation) are still kept. This will generate a good starting point for the variational method in the next sweep.

4. Go to step 2 until k_l moves to the end of the Wilson chain.

5. Some more sweeps until fully converged based on $var(E)$.

4.10 Follow up study of SBM2

There are still many open questions about the quantum phase transition in SBM2 and its generalization. Some of which are discussed in the following.

The quantum transition QC1, which is the transition between the localized and critical phase, is expected to be non-classical. However there is still no solid argument yet. There are a few critical exponents which can tell the nature of the transition, namely β, δ, δ' and ν defined as

$$\langle\sigma_x\rangle \propto (\alpha - \alpha_c)^{\beta}, \text{ for } \vec{h} = 0 \text{ and } \alpha > \alpha_c \tag{4.46}$$

$$\langle\sigma_x\rangle \propto h_x^{1/\delta}, \text{ for } \alpha = \alpha_c \tag{4.47}$$

$$\langle\sigma_z\rangle \propto h_x^{1/\delta'}, \text{ for } \alpha = \alpha_c \tag{4.48}$$

$$\xi \propto (\alpha_c - \alpha)^{-\nu}, \text{ for } \alpha < \alpha_c \tag{4.49}$$

with ξ the correlation length. The current numerics breaks the U(1) symmetry of SBM2 and prevents us to determine the accurate phase boundary and the critical exponents (Fig. 4.10

for example). Therefore explicit implementation of the U(1) symmetry is necessary before further investigating QC1 of SBM2.

The transition QC2, which is between the localized and delocalized phase, is probably equivalent to the transition of a classical long-range XY model. The predicted exponents based on this argument are

$$\beta = 1/2, \delta = 3, 1/\nu = s, \text{ for } s < 1/2 \tag{4.50}$$

$$\delta = (1+s)/(1-s) \text{ for } s > 1/2 \tag{4.51}$$

$$1/\beta = 2 + (12/5)\epsilon, 1/\nu = 1/2 - (3/5)\epsilon \text{ for } s = 1/2 + \epsilon, \epsilon \ll 1 \tag{4.52}$$

$$1/\beta = 2 + o(\epsilon'^2), 1/\nu = \epsilon' \text{ for } s = 1 - \epsilon', \epsilon' \ll 1 \tag{4.53}$$

Exponents are defined the same with those in SBM1 except β is defined as

$$\langle \sigma_x \rangle \propto (h_z^c - h_z)^\beta. \tag{4.54}$$

Compared to SBM1, β and ν behave differently for $1/2 < s < 1$. Fig. 4.15 shows first results of the QC2 phase boundary. I have also calculated the β exponent for $s < 0.5$ (Table. 4.2) and it agrees with the predicted one.

s	α	h_z^c	β
0.3	0.1	0.3500	0.52
0.4	0.1	0.14835	0.48

Table 4.2: The phase boundary and fitted β exponent of QC2.

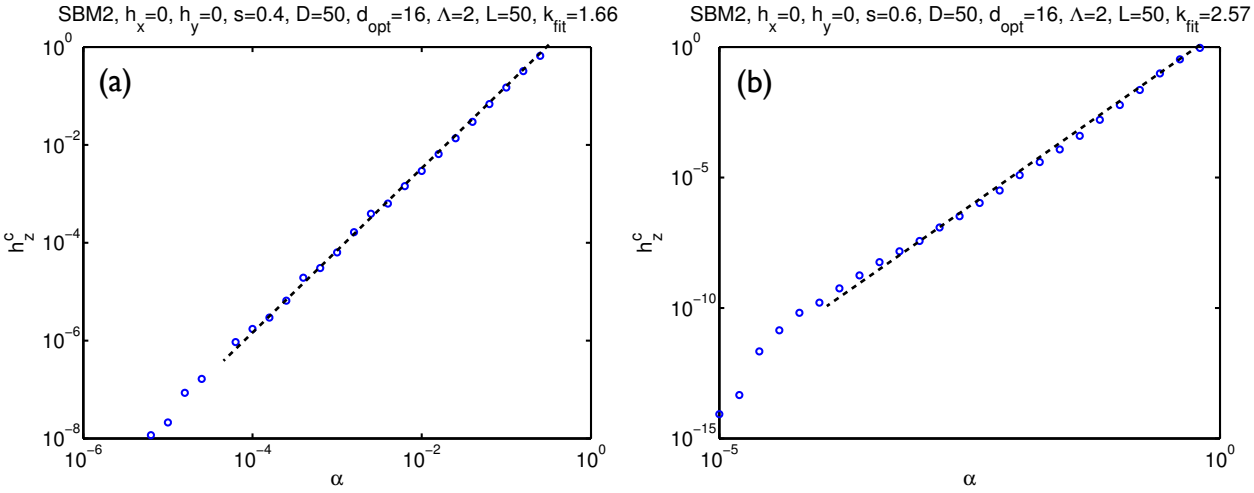

Figure 4.15: QC2 phase boundary h_z^c as a function of α for $s = 0.4$ (a) and $s = 0.6$ (b). The VMPS results confirm the weak-coupling RG prediction that there is a power law relation $h_z^c \propto \alpha^k$ with $k = 1/(1-s)$. The dashed lines are linear fitting, and the fitted exponents are shown in the caption and it agrees with the RG prediction.

Chapter 5

Quantum Telegraph Noise Model

The most studied type of bath of quantum dissipative systems is a collection of harmonic oscillators or electrons in the conduction band. These kinds of baths consist of many particles and display Gaussian-distributed fluctuations to a good approximation. However this approximation will break down when the quantum system is coupled to only a few noise sources. Some nanoscale quantum coherent systems recently proposed as candidates for quantum information processing [46, 7, 83] belong to this category. One of the simplest models with non-Gaussian type noise is the quantum telegraph noise model (QTNM) [67, 31, 1, 35]. In this chapter I explore the feasibility and performance of DMRG and t-DMRG to study the QTNM.

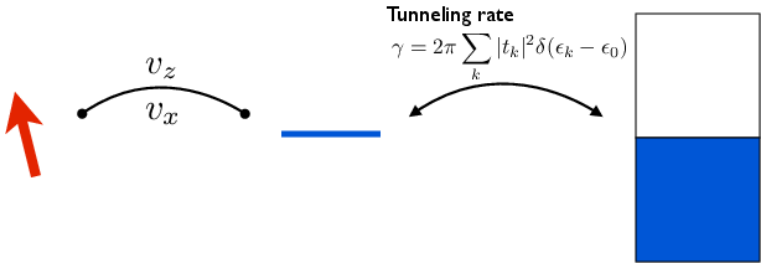

Figure 5.1: The quantum telegraph noise model.

5.1 Decoherence

The static quantum telegraph noise model describes a single, spin-polarized impurity level, tunnel-coupled to a non-interacting spinless fermion reservoir as illustrated in Fig. 5.1. The Hamiltonian is

$$H = \frac{\Delta}{2}\sigma_z + \left(\frac{v_x}{2}\sigma_x + \frac{v_z}{2}\sigma_z\right) d^\dagger d + H_B, \tag{5.1}$$

where H_B is the bath Hamiltonian

$$H_B = \epsilon_0 d^\dagger d + \sum_k (t_k c_k^\dagger d + h.c.) + \sum_k \epsilon_k c_k^\dagger c_k. \tag{5.2}$$

To facilitate the DMRG study of this model, we transform the bath to the 1D Wilson chain form:

$$H_B = \epsilon_0 d^\dagger d + \sqrt{\frac{\gamma D}{\pi}}(f_0^\dagger d + d^\dagger f_0) + \frac{D}{2}(1+\Lambda^{-1})\sum_{n=0}^{\infty}\Lambda^{-n/2}\xi_n(f_n^\dagger f_{n+1} + f_{n+1}^\dagger f_n), \tag{5.3}$$

where γ is the tunneling rate

$$\gamma = 2\pi\sum_k |t_k|^2\delta(\epsilon_k - \epsilon_0). \tag{5.4}$$

Note that here the definition of γ has a factor of 2 difference with the "hybridization parameter" $\Gamma = \pi\sum_k |t_k|^2\delta(\epsilon_k - \epsilon_0)$ usually used by the NRG community.

First we study the decoherence of the qubit under telegraph noise. The starting state is

$$|\psi(0)\rangle = \frac{\sqrt{2}}{2}(|\uparrow\rangle + |\downarrow\rangle)|\phi(0)\rangle, \tag{5.5}$$

where $|\phi(0)\rangle$ is the state of the bath at $t = 0$. At zero temperature, we use the ground state of the bath as $|\phi(0)\rangle$. $|\psi(0)\rangle$ can be generated by calculating the ground state of the following engineered Hamiltonian

$$H_0 = \sigma_x + H_B, \tag{5.6}$$

with $\epsilon_0 = 0$ in H_B.

We then use t-DMRG to calculate $|\psi(t)\rangle$ with the original Hamiltonian (5.1). The reduced density matrix of the spin is

$$\rho^s(t) = Tr_B|\psi(t)\rangle\langle\psi(t)|, \tag{5.7}$$

and the visibility is defined as

$$|D(t)| \equiv 2|\rho^s_{\uparrow\downarrow}(t)|. \tag{5.8}$$

The visibility of the free decoherence process can also be calculated analytically [1], and it can serve as a benchmark for the performance of t-DMRG to study the QTNM. There are several sources of error in our t-DMRG treatment: the DMRG truncation dimension χ, Trotter decomposition error, band discretization. I found that among the three sources of error the first two are not as important as the third one. With relatively small χ and typical Trotter step size (Fig. 5.2) the results is already well converged. Therefore I focus on the influence of different discretization scheme to the visibility result. More specifically I recalculate Fig. 2 in Ref. [1] at $T = 0$ with two different types of discretization schemes: linear and logarithmic discretization.

The energy resolution of linear discretization is the same throughout the band and is proportional to the inverse of the number of levels representing the band $1/L$. Fig. 5.3 shows the visibility with different linear discretization parameter L. We can see that we need a very long chain length L to reach a converged results if we use linear discretization which reflects the fact that the relevant energy scale of this problem is smaller than 10^{-3}.

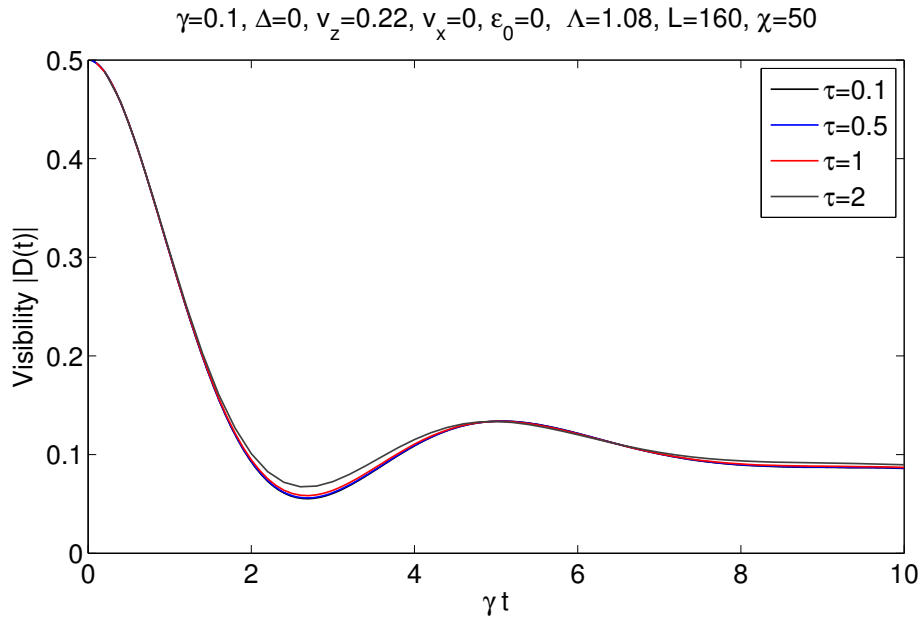

Figure 5.2: Visibility for different tDMRG time step τ. The result is already converged at $\tau = 0.5$.

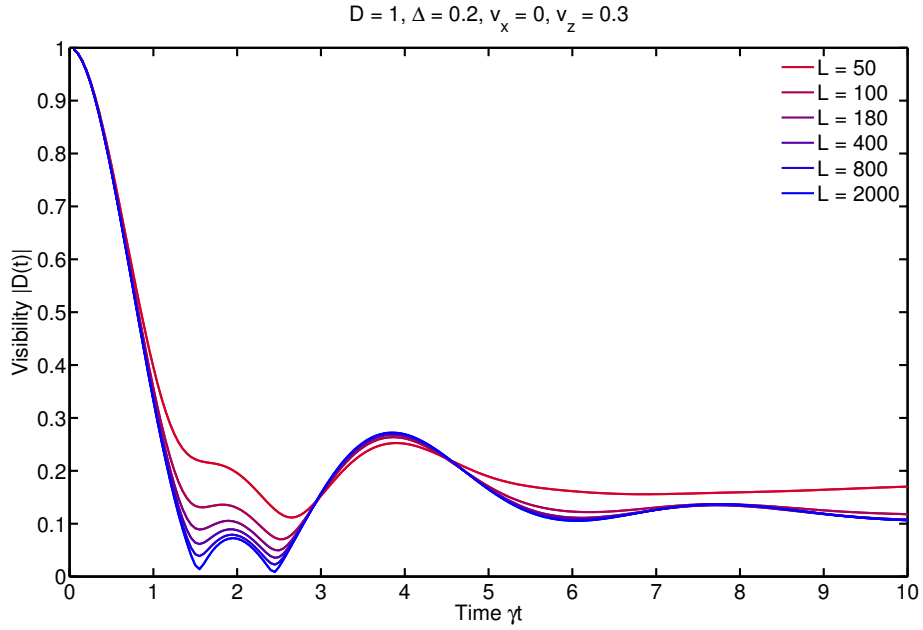

Figure 5.3: Visibility for different chain lengths L with linear discretization in energy space. We need a very long chain length to reach a converged result, which reflects the fact that the relevant energy scale of this problem is smaller than 10^{-3}.

Next we will try different logarithmic discretization schemes. Fig. 5.4 shows the visibility calculated with different Wilson chain lengths. The result has converged with $L = 160$. Unlike linear discretization the result converges very fast with respect to the Wilson chain length L. This is simple to understand as the logarithmic discretization reaches small energy scales much faster. The smallest energy scale with the parameters used in Fig. 5.4 for $L = 160$ is smaller than 10^{-5} already which would require $L > 100000$ if we used linear discretization. Note the model parameter I used is different with those in Fig. 5.3 but the numerical behavior in response to discretization is the same.

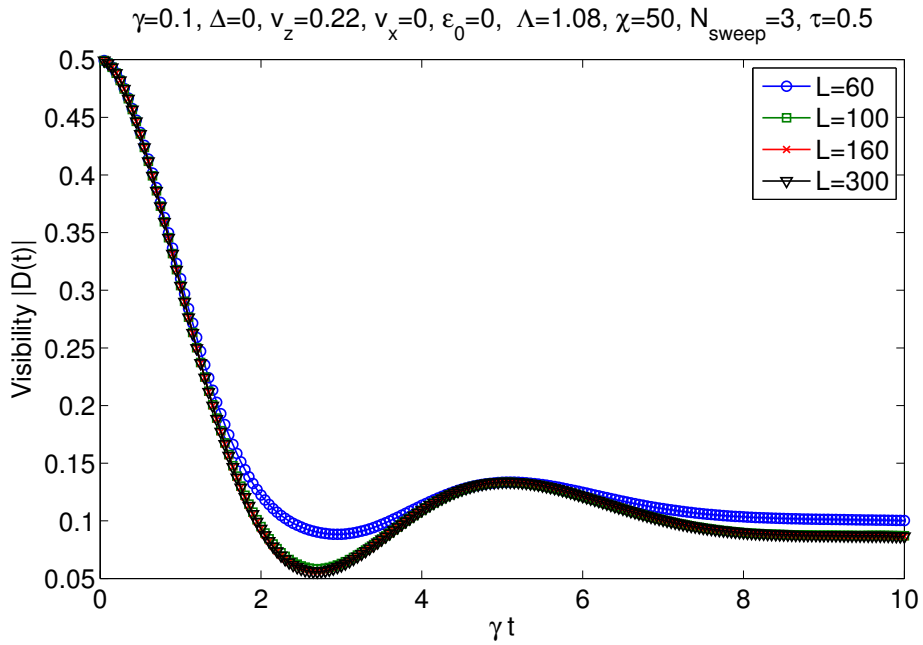

Figure 5.4: Visibility for different Wilson chain length L with logarithmic discretization scheme. The result converges much faster than in the linear discretization case, and it already converges at $L = 160$.

Fig. 5.5 shows the influence of different set logarithmic discretization parameter Λ with a long enough L. The oscillations for bigger Λ is a typical discretization artifact. It is caused by the insufficient number of levels of the logarithmic discretization to represent the high energy part of the band. More levels in the high energy part will average out those oscillations. Based on the same reasoning these oscillations could be suppressed significantly by using z-averaging [29, 116, 64, 14] as shown in Fig. 5.6. We need to calculate several different z-values to obtain the averaged curve while we need only one calculation if we use linear or logarithmic discretization with small Λ. However, the advantage of z-averaging is that one can use a relatively large Λ and a very short Wilson chain length therefore each calculation is very fast and it is very straight forward to harness the power of multiple CPUs.

We use t-DMRG and logarithmic discretization to calculate the visibility result as shown in Fig. 2 in Ref. [1]. The t-DMRG results agree the analytical results very well as shown

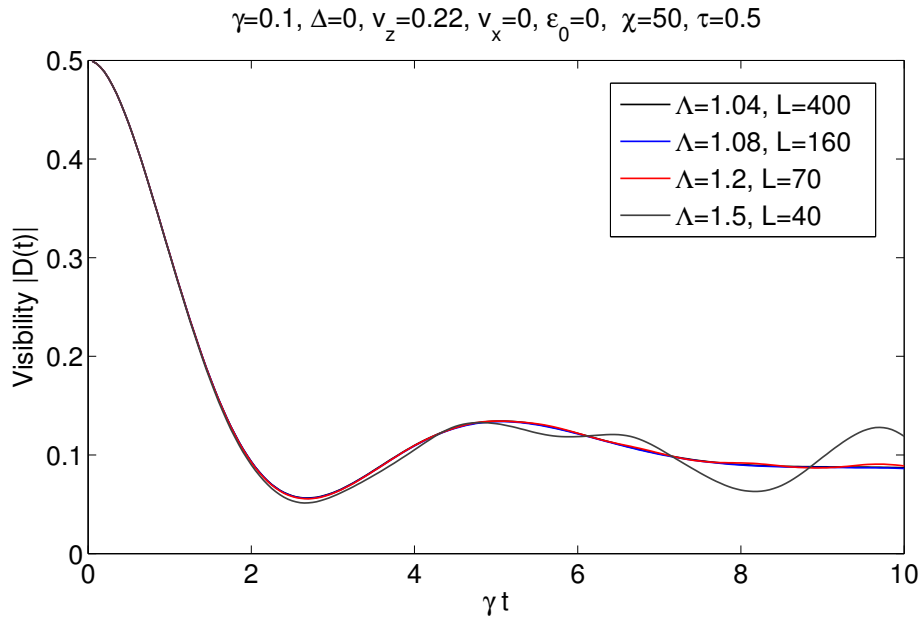

Figure 5.5: Visibility using different logarithmic discretization parameters Λ. L is chosen so that the result has already converged. The insufficient number of levels representing the high energy part of the band will causes "artificial" oscillations like those seen in this plot for $\Lambda = 1.5$.

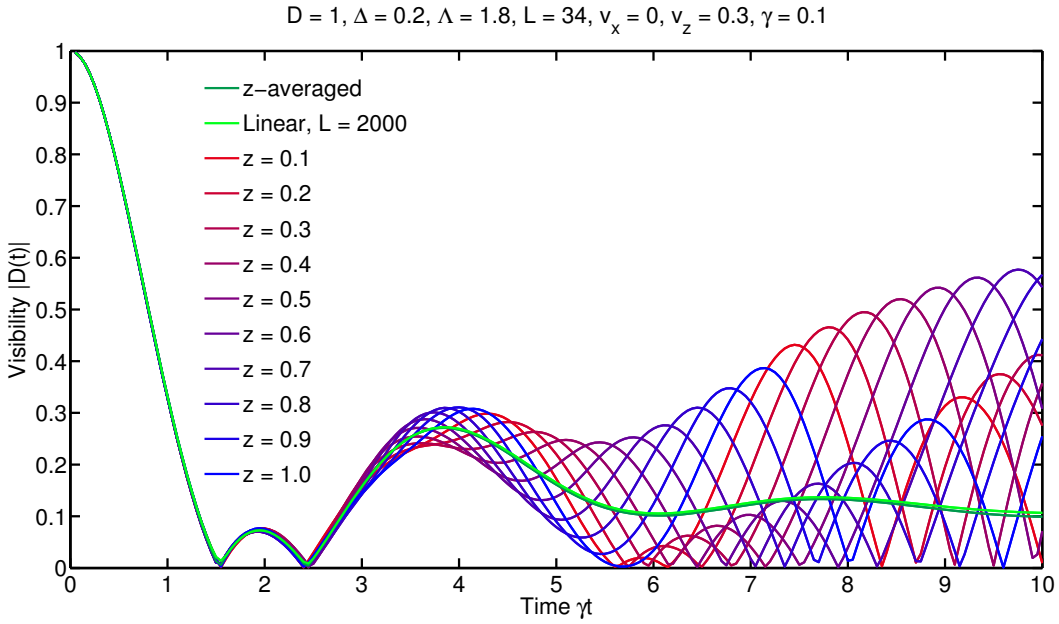

Figure 5.6: Using z-averaging to reduce the artificial oscillations caused by imprecise representation of the high energy part of the band. We used $\Lambda = 1.8$ and $L = 34$ for the logarithmic discretization. 10 equally spaced z values in (0,1] are used here.

in Fig. 5.7.

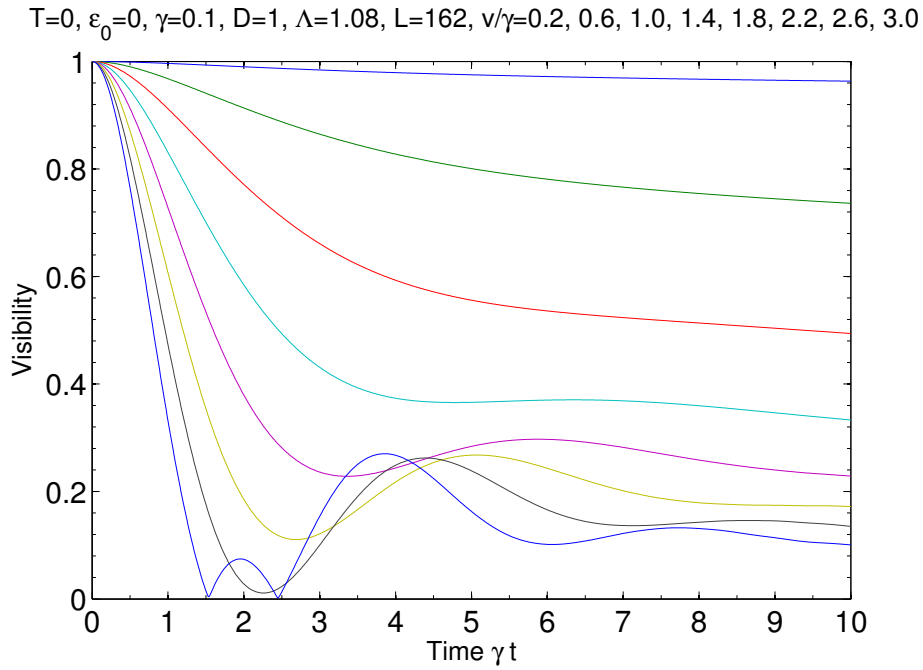

Figure 5.7: Visibility calculated with t-DMRG for $v_x = 0$ and several different v_z as Fig. 2 in [1]. t-DMRG results agree with the analytical results very well.

5.2 Spin echo

Spin echo is originally a technique used in nuclear magnetic resonance to refocus spin magnetization. Now it is also widely adapted to solid state qubit experiments to reduce the influence of 1/f noise [60]. Ref. [1] studied the effectiveness of spin echo to reduce the influence of telegraph noise analytically and found spin-echo has very limited effect.

We simulate the application of spin-echo on QTNM at $T = 0$ with t-DMRG, and the result is shown in Fig. 5.8. Unlike the visibility curve without pulse, which serves as a comparison here, the spin-echo curve is not from one t-DMRG calculation but from independent calculations for each data point in the curve. For example the data point at time t is obtained by applying a π pulse $e^{i\pi\sigma_x/2}$ at $t/2$ and just take the visibility at t. The result agrees very well with the results shown in Fig. 5(d) of Ref. [1]. (Note that the curve without pulse in Ref. [1] is not correct.)

5.3 Spectroscopy of periodic drive

Next we want to study the time-dependent driving spectroscopy under the driving term

$$H_{dri} = \Omega \cos(\omega t)\sigma_x \tag{5.9}$$

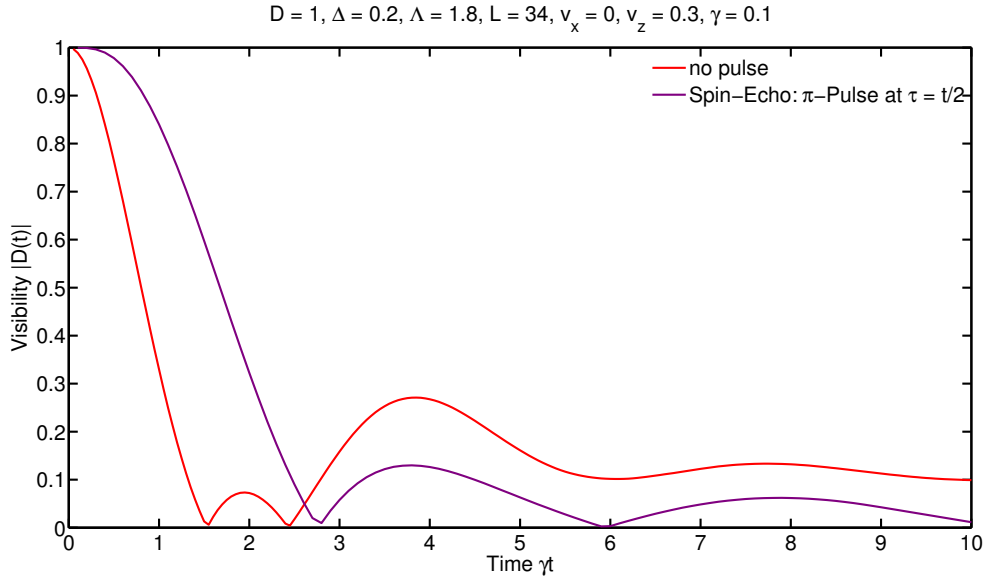

Figure 5.8: Visibility with a π pulse applied at $t/2$ simulated with t-DMRG for $T = 0$. This result agrees very well with those in Ref. [1]. The result shows that the effect of spin-echo to increase the decoherence time is very limited for the telegraph noise model.

Even though the Hamiltonian is now time-dependent it gives no extra difficulty for t-DMRG to simulate. Fig. 5.9 shows some examples of the magnetization as a function of time calculated with t-DMRG. The calculation time of each curve takes less than one hour on a single CPU core.

We can see from Fig. 5.9 that the amplitude of the low frequency oscillations decays due to the influence of the bath. The high frequency oscillations directly caused by the periodic drive do not decay over time as shown in Fig. 5.10. The reason is that with just one level coupled to the spin it is very difficult for the bath to damp the fast oscillations.

With different driving strength Ω and frequency ω the finial $\sigma_z(t)$ as $t \to \infty$ will oscillate around different values. The final average $\langle\sigma_z\rangle$ (or equivalently the probability for the spin to be in the up state P_{up}) as a function of driving frequency ω is referred to as the spectroscopy.

As we can see from Fig. 5.9 the time scale of the low frequency decay is much longer than the typical time scale of the telegraph noise $(1/\gamma)$ for the parameter range we studied. Therefore one would expect that any prior information of the spin which passed to the resonant level will dissipated immediately by the fermionic bath and thus has no influence to the current state of the spin through the resonant level. This justifies the Markovian approximation, and the spectroscopy can be calculated with the following master equation:

$$\frac{d\hat{\rho}(t)}{dt} = -i\left[\hat{H}_s(t), \hat{\rho}(t)\right] + \Gamma\mathcal{L}\left[\hat{R}_\Gamma\right]\hat{\rho}(t) + \Gamma_\psi\mathcal{L}\left[\hat{R}_{\Gamma_\psi}\right]\hat{\rho}(t), \tag{5.10}$$

where $\hat{\rho}(t)$ is the density matrix of the spin at time t. $H_s(t)$ is the time-dependent Hamil-

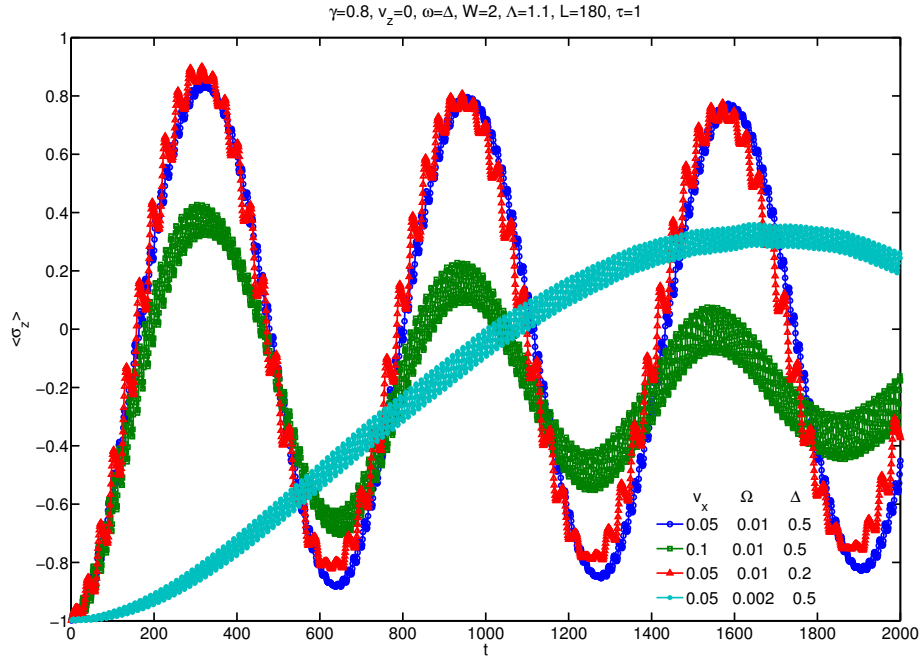

Figure 5.9: t-DMRG simulation of the quantum telegraph noise model under a periodic driving for several different model parameters. We keep 50 DMRG states which already gives converged results.

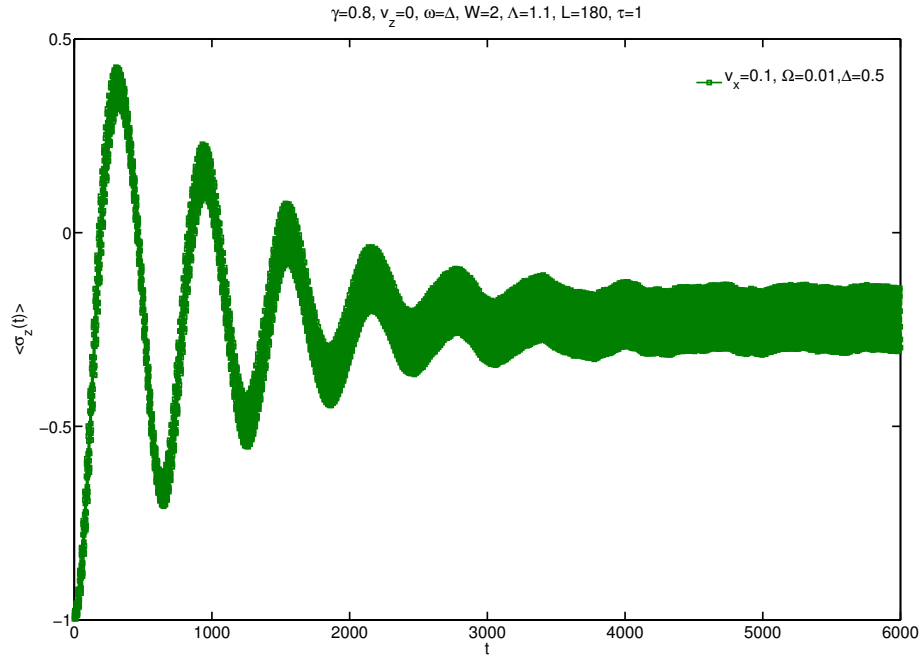

Figure 5.10: Same as the green curve in Fig. 5.9 but showing longer time range.

tonian of the spin

$$H_s(t) = \Omega\cos(\omega t)\sigma_x + \frac{\Delta}{2}\sigma_z. \tag{5.11}$$

$\mathcal{L}\left[\hat{R}\right]$ is a Lindblad superoperator that depends on a relaxation operator $\hat{R}$ and acts, with a rate Γ (or Γ_ψ), as follows:

$$\mathcal{L}\left[\hat{R}\right]\hat{\rho} = \hat{R}\hat{\rho}\hat{R}^\dagger - \frac{1}{2}(\hat{R}^\dagger\hat{R}\hat{\rho} + \hat{\rho}\hat{R}^\dagger\hat{R}), \tag{5.12}$$

with

$$\hat{R}_\Gamma = |\downarrow\rangle\langle\uparrow|, \tag{5.13}$$

$$\hat{R}_{\Gamma_\psi} = \sqrt{2}\,|\uparrow\rangle\langle\uparrow| \tag{5.14}$$

respectively describes the decay from the spin-up state to the spin-down state and the fluctuation of the level splitting due to the influence of the environment. Fig. 5.11 shows the meaning of parameters in the master equation.

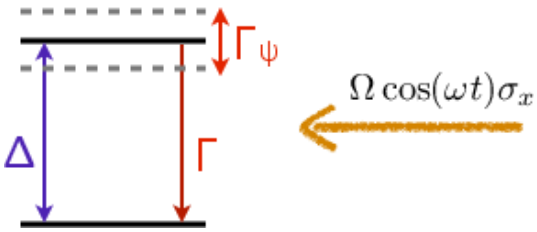

Figure 5.11: Illustration of how the master equation deals with the driven dissipative two level system. Δ is the level splitting (energy difference), Γ is decay rate from the upper level to the lower level and Γ_ψ is the fluctuation of the energy splitting.

This master equation can be solved numerically and some well known results are shown in Fig. 5.12 (left two plots) together with results from t-DMRG simulations of the telegraph noise model (right two plots). In Fig. 5.12(a) where the driving amplitude is relatively weak the system is in its linear regime according to master equation. The characteristics of the linear regime is that the peak height P_{max} is proportional to the intensity of the external driving field Ω^2. With the same weak driving field, the t-DMRG results of QTNM are shown in Fig. 5.12(b). Though the data looks similar, it does not give such a linear relation, even after we subtract the offset of P_{up} from 0 seen in these curves. This deviation from linear behavior may derive from the Markovian approximation which is not always a good approximation for the whole parameter regime in this plot. The offset itself is simply due to how the spin is coupled to the bath. As I set $v_z = 0$, the coupling term is

$$H_{couple} = \frac{v_x}{2}\sigma_x d^\dagger d. \tag{5.15}$$

When the resonant level is not empty this term makes the instantaneous ground state no longer the spin-down state. This is the reason why we see an offset of P_{up}. The offset of ω/Δ (that is the peak is not at $\omega/\Delta = 1$) is due to the same reason.

If the driving field is strong enough we will see multi-photon resonance signaled by the side peaks shown in Fig. 5.12(d). In this plot the biggest side peak is at the position $\omega/\Delta = 1/3$ caused by the three-phonon resonance. We see some similar multi-phonon resonance in the t-DMRG result Fig. 5.12(c). Interestingly, the position of the three-phonon peak is not at $\omega/\Delta = 1/3$ as seen in the analytical data but is shifted by three times the amount the main peak is shifted.

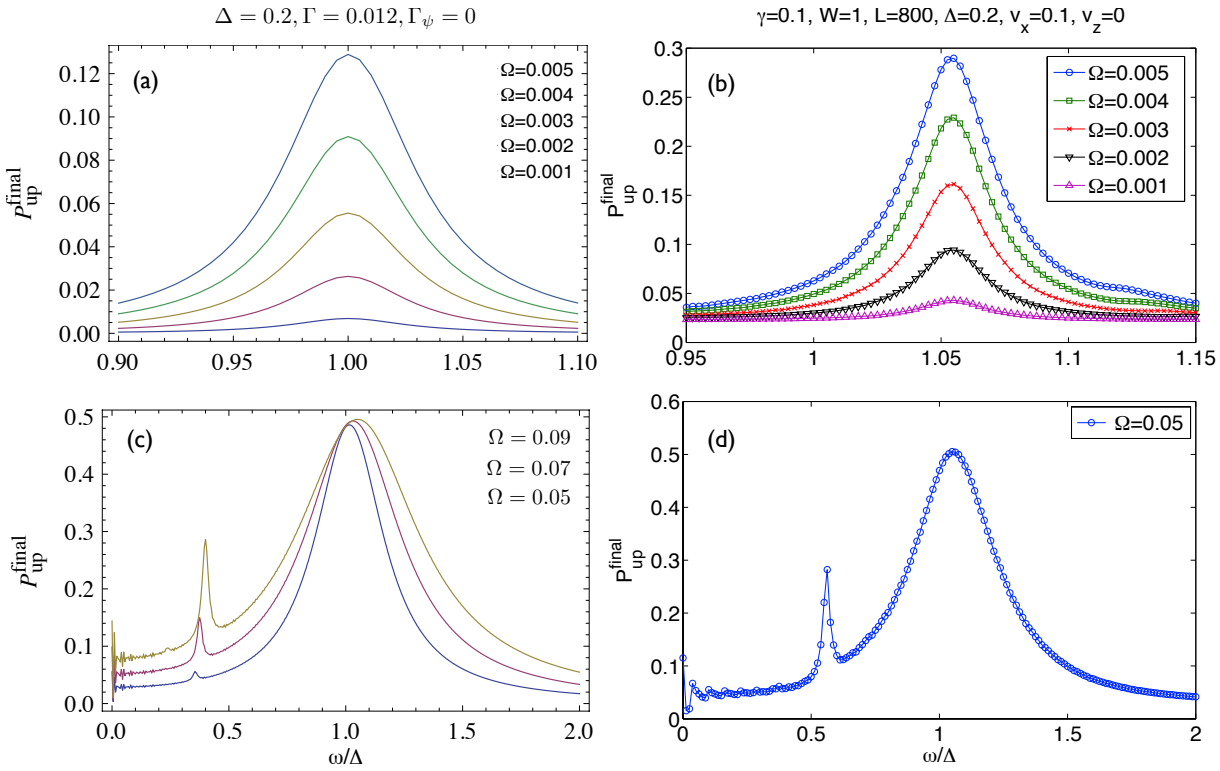

Figure 5.12: Spectroscopy from master equation (a), (c) and t-DMRG (b), (d). (a) and (b) is the week driving case; (c) and (d) are the strong driving case. The master equation uses the Markov approximation and represents the influence of the bath on the spin simply by two decay rate parameters. The t-DMRG results are numerical simulations of the quantum telegraph noise model by solving the full Schrödinger equation directly. Even though the results of t-DMRG look qualitatively similar to the master equation solution, there are some clear quantitative differences as explained in the main text.

Appendix A

Žitko-Pruschke logarithmic discretization of boson bath

Rok Žitko and Thomas Pruschke proposed a slightly modified and more accurate scheme of logarithmic discretization [98] which "removes the band-edge discretization artifacts of the conventional approach and significantly improves the convergence to the continuum $\Lambda \to 1$ limit". It should always be used instead of the conventional logarithmic discretization. In this appendix I will describe how to use this new scheme to discretize the bosonic bath.

The discretization mesh of the logarithmic discretization is defined by ϵ_m^z, where z is used for the "z-averaging" [14] and

$$\epsilon_0^z = \omega_c \tag{A.1}$$
$$\epsilon_m^z = \omega_c \Lambda^{2-j-z},\ (m = 1, 2, 3, ...) \tag{A.2}$$

After we define the mesh, we need to calculate the energy of each slice of the band ξ_m^z defined in Eq. (S2) in Section 4.1. In the conventional logarithmic discretization scheme it is calculated as

$$\xi_m^z = \frac{\int_{I_m} d\epsilon}{\int_{I_m} d\epsilon/\epsilon} = \frac{\epsilon_m^z - \epsilon_{m+1}^z}{\ln(\epsilon_m^z/\epsilon_{m+1}^z)} \tag{A.3}$$

with $I_m = [\epsilon_m^z, \epsilon_{m+1}^z]$. This will result in discretization artifacts especially near the band edge as explained by Žitko's paper. In the modified scheme, ξ_m^z are calculated by solving the differential equation

$$\xi(0) = \omega_c \tag{A.4}$$
$$\frac{d\xi(x)}{dx} = \frac{\int_{\epsilon(x)}^{\epsilon(x+1)} J(\omega) d\omega}{J[\xi(x)]} \tag{A.5}$$

where $x = m + z$ and $x \in [0, +\infty)$. Thus, $\epsilon(x)$ and $\xi(x)$ are the continuous form of ϵ_m^z and

ξ_m^z. We need two steps to solve the whole problem. First we need to solve ξ_0^z with

$$\begin{aligned}\int_{\epsilon(x)}^{\epsilon(x+1)} J(\omega)d\omega &= \int_1^{\epsilon_2^z} J(\omega)d\omega \\ &= \frac{\alpha}{1+s}[\Lambda^{-z(1+s)}-1] \end{aligned} \tag{A.6}$$

and

$$\xi_0^0 = \omega_c = 1 \tag{A.7}$$

After we have ξ_0^z, ξ_m^z is solved by using

$$\begin{aligned}\int_{\epsilon(x)}^{\epsilon(x+1)} J(\omega)d\omega &= \int_{\epsilon_m^z}^{\epsilon_{m+1}^z} J(\omega)d\omega \\ &= \frac{\alpha}{1+s}[\Lambda^{(1-m-z)(1+s)}-\Lambda^{(2-m-z)(1+s)}] \end{aligned} \tag{A.8}$$

and

$$\xi_1^0 = \xi_0^1 \tag{A.9}$$

The final results are Eq. (S2) in Section 4.1.

Appendix B

Overlap of two VMPS wave functions with different shifts

Sometimes we need to calculate the overlap of two different wave functions when verifying the numerics or when we study the fidelity. Without bosonic shift it is very straightforward to calculate the overlap: one just contracts the local dimension of the two wave functions. When oscillator shifts are used, the local basis is different if the shifts are not exactly the same. Therefore to calculate the overlap of different VMPS states with shifts $|\psi(\delta_1, \delta_2, \cdots, \delta_L)\rangle$, $|\psi'(\delta'_1, \delta'_2, \cdots, \delta'_L)\rangle$ one needs to "unshift" the wave functions first:

$$\begin{aligned}\langle\psi'(\delta'_1, \delta'_2, \cdots, \delta'_L)|\psi(\delta_1, \delta_2, \cdots, \delta_L)\rangle &= \langle\psi'(\delta'_1, \delta'_2, \cdots, \delta'_L)|U(\delta'_1)U(\delta'_2), \cdots, U(\delta'_L) \\ &\quad \times U^\dagger(\delta_1)U^\dagger(\delta_2), \cdots, U^\dagger(\delta_L)|\psi(\delta_1, \delta_2, \cdots, \delta_L)\rangle \quad \text{(B.1)} \\ &= \langle\psi'(\delta'_1, \delta'_2, \cdots, \delta'_L)|\prod_k U(\delta'_k)U^\dagger(\delta_k)|\psi(\delta_1, \delta_2, \cdots, \delta_L)\rangle\end{aligned}$$

By definition the local unshift operator $S = U(\delta')U^\dagger(\delta)$ (for simplicity I omit the subscript k) is

$$\begin{aligned}S &= U(\delta')U^\dagger(\delta) \\ &= e^{\frac{\delta'}{\sqrt{2}}(b^\dagger - b)}e^{-\frac{\delta}{\sqrt{2}}(b^\dagger - b)} \\ &= e^{\frac{(\delta' - \delta)}{\sqrt{2}}(b^\dagger - b)} \\ &= e^{\frac{(\delta' - \delta)}{\sqrt{2}}(b^\dagger - b)} \\ &\equiv e^{t(b^\dagger - b)} \quad \text{(B.2)}\end{aligned}$$

S operator is infinitely large if represented in the full, infinite boson basis, so numerically we need to truncate it. One should be cautious that S should only be truncated after having been evaluated with infinite large b, $b^\dagger$ operators. If one calculates S with truncated b, $b^\dagger$ the results is incorrect. To evaluate S, we first expand it with the Zassenhaus relation

$$e^{t(X+Y)} = e^{tX}e^{tY}e^{-\frac{t^2}{2}[X,Y]}e^{\frac{t^3}{6}(2[Y,[X,Y]]+[X,[X,Y]])}\cdots \quad \text{(B.3)}$$

and we have

$$\begin{aligned} S &= e^{tb^\dagger} e^{-tb} e^{\frac{t^2}{2}[b^\dagger, b]} \\ &= e^{tb^\dagger} e^{-tb} e^{-\frac{t^2}{2}} \\ &= e^{-\frac{t^2}{2}} \sum_{n=0}^{\infty} \frac{(tb^\dagger)^n}{n!} \sum_{m=0}^{\infty} \frac{(-tb)^m}{m!} \end{aligned} \tag{B.4}$$

The matrix elements of S are

$$\begin{aligned} \langle\alpha|S|\beta\rangle &= e^{-\frac{t^2}{2}} \sum_{n,m=0}^{\infty} \frac{(-1)^m t^{n+m}}{n!m!} \langle\alpha|(b^\dagger)^n b^m|\beta\rangle \\ &= e^{-\frac{t^2}{2}} \sum_{n,m=0}^{\infty} \frac{(-1)^m t^{n+m}}{n!m!} \langle\alpha| \frac{1}{\sqrt{\alpha!}} b^\alpha (b^\dagger)^n b^m (b^\dagger)^\beta \frac{1}{\sqrt{\beta!}} |0\rangle \\ &= \frac{e^{-\frac{t^2}{2}}}{\sqrt{\alpha!\beta!}} \sum_{n,m=0}^{\infty} \frac{(-1)^m t^{n+m}}{n!m!} \langle\alpha| b^\alpha (b^\dagger)^n b^m (b^\dagger)^\beta |0\rangle \end{aligned} \tag{B.5}$$

inside the summation only terms which satisfy $m \leq \beta$, $n \leq \alpha$ and $\alpha + m = \beta + n$ are non zero. When $m \leq \beta$ we have

$$\begin{aligned} b^m (b^\dagger)^\beta |0\rangle &= \beta b^{m-1} (b^\dagger)^{\beta-1} |0\rangle \\ &= \frac{\beta!}{m!} (b^\dagger)^{\beta-m} |0\rangle, \end{aligned} \tag{B.6}$$

and similar for the conjugate part. It can be easily verified that the finial result is

$$\langle\alpha|S|\beta\rangle = e^{-\frac{t^2}{2}} \sqrt{\alpha!\beta!} \sum_{m=0}^{\beta} \frac{(-1)^m t^{\alpha-\beta+2m}}{[m!(\alpha-\beta+m)!]^2} (\beta - m)! \tag{B.7}$$

This formula can be numerically calculated for

$$\alpha = 1, 2, \cdots, d'_k \tag{B.8}$$

$$\beta = 1, 2, \cdots, d_k \tag{B.9}$$

Appendix C

Snake - a DMRG program

Snake is an open-source DMRG program I developed using c++ and Matlab. The choice of the name is because of the 1D nature of DMRG. It includes infinite DMRG, finite DMRG, t-DMRG and finite temperature DMRG. The code can be found here: `http://code.google.com/p/snake-dmrg/` The calculations in Chap. 3 and Chap. 5 are calculated with Snake.

Some key feature of Snake are:

- A simple Matlab file to define the Hamiltonian, and the c++ DMRG code can be used as a black box.
- Main part of the code is written in c++. It is object oriented and highly optimized.
- Most time consuming operations are reduced to matrix operations, and standard linear algebra routines like BLAS, LAPACK and ARPACK are called by the c++ code to speed up the calculation.
- Multiple Abelian symmetries.

The following classes are defined in the program:

GQN The good quantum number class. A vector is used to store all good quantum numbers (multiple Abelian symmetries). Common operators are overloaded for the good quantum number calculations.

GQNBase The class which describes the basis organized according to good quantum numbers. It contains information like the number of good quantum numbers and dimension of each good quantum numbers. Functions used by DMRG like Kronecker product and basis truncation are implemented here. Comparison operations are overloaded.

GQNMat Class of a partitioned matrix according to good quantum number with GQNBase being the basis of the matrix. Only non-zero blocks are stored to save space. Common matrix operations are redefined so that the GQNMat can be used like a normal matrix without caring about internal operations.

Site DMRG site class. Contains DMRG site information and DMRG operations on one site such as site operator renormalization, adding a site to a block and read/write site information from/to files etc.

BlocHam Class of the Hamiltonian of a block.

DTMat Class of the reduced density matrix of the system/environment block and the transformation matrix.

Block Class about all information of a DMRG block such as the number of sites information of each site in the block (stored as Site object), block Hamiltonian (stored as BlocHam object), block basis (stored as GQNBase object) etc. DMRG block operations like adding a site to a block and renormalize block are defined here.

SupBlock This class contains information related to the super block. High level DMRG operations like sweeping, calculating the ground state, t-DMRG etc.

DMRG Highest level interface of the program. Defines the problem, reads operators and writes the finial results to files.

To use Snake, one can simply define the program with a Matlab script called “gen_model.m”. The following is an example for studying the telegraph noise model. It will generate a folder called “model” containing the information of the problem. Then one can run the Snake program to read files inside this folder and start the DMRG calculation.

```
function gen_model(Omega,omegaratio,Lambda,BathL,z,discr,vx,vz)

%%%%%%%%%%%%%%%%----------MODEL INFO--------%%%%%%%%%%%%%%%%%%%%%%

%%%%%----------Model Parameters
FlorianGamma=0.1;
D=1;
Delta=0.2;
%vz=0;
%vx=0.1;
epsilon0=0;
%Field applied on the first site of the chain--the spin site
ed0=100;
%Driven parameters
w=omegaratio*Delta; %driving frequesncy

%%%%%---------Discretization Parameters
%Lambda=2;
%BathL=20;
switch discr
        case 'log'
                [a,b]=roklogdiscr(FlorianGamma/2,D,Lambda,BathL,z);
        otherwise
```

```
                    inter=D*2/BathL;
                    [a,b]=lindiscr(FlorianGamma/2,inter,D);
end

para.TGQN=BathL/2
para.L=BathL+2

folder=sprintf('omega%gratio%gLambda%gBathL%gz%g%svx%gvz%g',Omega,omegaratio,Lambda,BathL,z,discr,vx,vz);
mkdir(folder);
system(['cp␣./cppsrc/Snake␣' folder]);
para.folder=[folder,'/model'];
mkdir(para.folder);


%%%%------Time evolution Parameters
%%Trotter step of real time
rt_tau=0.5;
%Stating time
t_start=0;
%Ending time
t_end=2000;
%Time span
T=t_end-t_start;
%Time step number
para.t_num=T/rt_tau;


%%%%%%%%%%%%%%%%%-------SITE INFO-------%%%%%%%%%%%%%%%%%%%%%
%The first type of site is spin
para.site{1}=genspinsite('fermion');
%The second type of site is spinless fermion
para.site{2}=genspinlessfermionsite('fermion');


%%%%%%%%%%%%%-----STARTING STATE HAMILTONIAN-----%%%%%%%%%%%%%%%
para.onesiteE=zeros(para.L,1);
para.onesiteE(1)=ed0;
para.twositesV=zeros(para.L-1,1);
para.hopT=zeros(para.L-1,1);
para.hopT(1)=0;
for i=2:para.L-1
    para.hopT(i)=b(i-1);
end

%para.h0{1}=ed0*kron(para.site{1}.sigmax,eye(2));
para.h0first=ed0*para.site{1}.sigmaz;
para.h0{1}=kron(para.h0first,eye(2));
for i=2:para.L-1
para.h0{i}=para.hopT(i)*(kron(para.site{2}.cm,para.site{2}.cp)+kron(para.site{2}.cp,para.site{2}.cm));
```

```
73  end
74
75
76  %%%%%%%%%%%%———TIME EVOLVING HAMILTONIAN————%%%%%%%%%%%%%%%
77
78  %%%%%————constat Wilson chain part
79  para.h{1}=eye(para.site{1}.sitedim*para.site{2}.sitedim); %Useless term
80  para.h{2}=epsilon0*kron(para.site{2}.n,eye(2))+para.hopT(2)*(kron(para.site
        {2}.cm,para.site{2}.cp)+kron(para.site{2}.cp,para.site{2}.cm));
81  for i=3:para.L-1
82  para.h{i}=para.hopT(i)*(kron(para.site{2}.cm,para.site{2}.cp)+kron(para.site
        {2}.cp,para.site{2}.cm));
83  end
84
85  for i=1:para.L-1
86  para.U{i}=expm(-1i*(rt_tau/2)*para.h{i});
87  end
88
89  %%%%%————Time-dependent impurity term
90  for i=1:para.t_num
91      t=(i-0.5)*rt_tau+t_start;
92      %para.h_imp_t{i}=(Delta/2)*kron(para.site{1}.sigmaz,eye(2))+(vz/2)*kron(
            para.site{1}.sigmaz,para.site{2}.n)+(vx/2)*kron(para.site{1}.sigmax,
            para.site{2}.n);
93      para.h_imp_t{i}=Omega*cos(w*t)*kron(para.site{1}.sigmax,eye(2))+(Delta
        /2)*kron(para.site{1}.sigmaz,eye(2))+(vz/2)*kron(para.site{1}.sigmaz,
            para.site{2}.n)+(vx/2)*kron(para.site{1}.sigmax,para.site{2}.n);
94      para.U_imp{i}=expm(-1i*(rt_tau/2)*para.h_imp_t{i});
95  end
96
97  %Save parameters to file for c++ program to read
98  savepara(para)
99
100 end
```

Line 5 to 15 define the model parameters. Line 17 to 26 generate Wilson chain Hamiltonian parameters. DMRG parameters are stored in the “para” structure. “para.TGQN” is the targeted good quantum number. For the telegraph noise model we use a half filled conduction band therefore “para.TGQN=BathL/2”. Line 31 to 35 generate the folder to store model information and move the complied Snake program to the folder. Line 38 to 48 define t-DMRG parameters. There are two kinds of site in this problem: the spin impurity site and spinless fermion site. The operators of these site are stored in para.site generated in Line 51 to 55. Line 58 to 73 is used to define the engineered Hamiltonian whose ground state is the starting state for t-DMRG calculation. Line 76 to 95 is used to generate the time-dependent Hamiltonian for the t-DMRG calculation. Line 98 saves the para structure to files so that the Snake program can read it.

Appendix D

Bosonic VMPS program

Bosonic VMPS is the Matlab program I developed to study the spin-boson model in Chap. 4. Its original form is based on the code by Verstraete et al. published on Ref. [90]. However, I have changed the code substantially to adapt it to the spin-boson model and to optimize the performance. It can be downloaded from `http://code.google.com/p/bosonic-vmps/`

In the following I group the scripts according to their functions:

The main program

- VMPS.m (define problem)

Generating operators and Hamiltonian

- bosonop.m (generate single site boson operators)
- spinop.m (generate single site spin operators)
- genh1h2term_onesite.m (define the Hamiltonian)
- genh1h2term.m
- SBM_genpara.m (generate parameters of Wilson chain Hamiltonian)
- star2tridiag.m
- paritykron.m (this the next two scripts is used for the parity version code)
- parityop.m
- parityorderOP.m

Initialization

- initCstorage.m
- initresults.m

- initstorage.m
- gennonzeroindex.m
- createrandomVmat.m
- createrandommps.m
- loadsaved.m

Optimization

- minimizeE.m
- optimizesite.m (optimize the A and V matrices of a certain site)
- minimizeE_onesiteA.m
- minimizeE_onesiteVmat.m
- HmultA.m ($H|\psi_A\rangle$)
- HmultVmat.m ($H|\psi_V\rangle$)

Basis update, orthogonalization and truncation during sweeping

- gen_sitej_h1h2.m (rescaling the local Hamiltonian terms)
- gen_sitej_op.m (rescaling operators)
- prepare.m (left- and right-orthogonalize the basis before the first sweep starts)
- prepare_onesite.m (left- or right-orthogonalize the basis of one site)
- prepare_onesiteAmat.m (SVD of A-matrix)
- prepare_onesiteVmat.m (SVD of V-matrix)
- prepare_onesite_truncate.m (Dynamical adjust the dimension of A-matrix D)
- rightnormA.m (right normalize the wave function)
- update_sitej_h1h2.m (update single site Hamiltonian terms after updated A- and V-matrix at each site)
- updateop.m (update block operators after updated A- and V-matrix at each site)
- adjustdopt.m (dynamically adjust the dimension of the optimal boson basis d_{opt})
- maxshift.m

- trustsite.m

Manipulation of wave function and calculating expectation values

- applyOP.m (apply any operator on a MPS)
- calbosonocc.m (calculate boson occupation)
- calbosonshift.m (calculate boson shift)
- calspin.m (calculate σ_x, σ_y, σ_z)
- expectationvalue.m
- expectation_allsites.m
- vonNeumannEntropy.m
- parity.m (calculate the parity of a MPS)

Basic VMPS functions and auxiliary functions

- updateCleft.m
- updateCright.m
- updateHleft.m
- updateHright.m
- contracttensors.m
- svd2.m

Appendix E

List of Abbreviation and Frequently Used Symbols

E.1 List of Abbreviation

Abbreviation	Full Name
1D/2D/3D	one/two/three-dimensional
DMRG	Density Matrix Renormalization Group method
fDMRG	finite DMRG
H.C.	Hermite conjugate term
iDMRG	infinite DMRG
LZ	Landau-Zener
MPS	Matrix Product State
NRG	Numerical Renormalization Group method
OBB	Optimal Boson Basis
QCC	Quantum Classical Correspondence
QTNM	Quantum Telegraph Noise Model
QPT	Quantum Phase Transition
SBM	Spin-Boson Model
SBM1/SBM2	One-/Two- Bath Spin-Boson Model
SVD	Singular Value Decomposition
t-DMRG	Adaptive time-dependent DMRG
TEBD	time-evolving block decimation algorithm
VMPS	Variational Matrix Product State method

E.2 List of Frequently Used Symbols

Symbol	Meaning
D	matrix dimension of MPS or half band width
d_{opt}	dimension of optimal local boson basis
d_k	dimension of local boson basis of the site k
Λ	logarithmic discretization parameter
σ_x, σ_y, σ_z	Pauli matrices
$J(\omega)$	spectral function
ω_c	cutoff frequency
$\langle n_k \rangle$, $\langle x_k \rangle$	the occupation and shift of the k-th oscillator
L	chain length
T^*	characteristic energy scale in NRG
h_x, h_y, h_z	components of external field on the spin
$\lvert D(t) \rvert$	Visibility at time t
Ω	amplitude of the periodic drive

Bibliography

[1] Benjamin Abel and Florian Marquardt. Decoherence by quantum telegraph noise: A numerical evaluation. *Physical Review B*, 78(20), November 2008.

[2] A. Alvermann and H. Fehske. Sparse polynomial space approach to dissipative quantum systems: Application to the sub-ohmic spin-boson model. *Physical Review Letters*, 102(15):150601, April 2009.

[3] Frithjof B. Anders and Avraham Schiller. *Phys. Rev. Lett.*, 95:196801, 2005.

[4] Frithjof B. Anders and Avraham Schiller. Real-time dynamics in quantum-impurity systems: A time-dependent numerical renormalization-group approach. *Physical Review Letters*, 95(19):196801–4, November 2005.

[5] P. W. Anderson. Localized magnetic states in metals. *Phys. Rev.*, 124(1):41–53, Oct 1961.

[6] Joachim Ankerhold and Hermann Grabert. Enhancement of macroscopic quantum tunneling by landau-zener transitions. *Physical Review Letters*, 91(1):016803, July 2003.

[7] O. Astafiev, Yu. A. Pashkin, Y. Nakamura, T. Yamamoto, and J. S. Tsai. Quantum noise in the josephson charge qubit. *Physical Review Letters*, 93(26):267007, December 2004.

[8] C. D. Batista, K. Hallberg, and A. A. Aligia. Specific heat of defects in the haldane system Y_2BaNiO_5. *Physical Review B*, 58(14):9248–9251, October 1998.

[9] Ralf Bulla, Theo Costi, and Thomas Pruschke. *Rev. Mod. Phys.*, 80:395, 2008.

[10] Ralf Bulla, Hyun-Jung Lee, Ning-Hua Tong, and Matthias Vojta. Numerical renormalization group for quantum impurities in a bosonic bath. *Phys. Rev. B*, 71:045122, 2005.

[11] Ralf Bulla, Hyun-Jung Lee, Ning-Hua Tong, and Matthias Vojta. Numerical renormalization group for quantum impurities in a bosonic bath. *Physical Review B*, 71(4):045122, January 2005.

[12] Ralf Bulla, Ning-Hua Tong, and Matthias Vojta. Numerical renormalization group for bosonic systems and application to the sub-ohmic spin-boson model. *Physical Review Letters*, 91(17):170601, October 2003.

[13] R. J. Bursill, T. Xiang, and G. A. Gehring. *J. Phys.: Condens. Matter*, 8:L583, 1996.

[14] Vivaldo L. Campo and Luiz N. Oliveira. Alternative discretization in the numerical renormalization-group method. *Physical Review B*, 72(10), 2005.

[15] M. A. Cazalilla and J. B. Maston. *Phys. Rev. Lett.*, 88:256403, 2002.

[16] M. S. Child. *Molecular Collision Theory*. Courier Dover Publications, July 2010.

[17] I. Chiorescu, Y. Nakamura, C. J. P. M. Harmans, and J. E. Mooij. Choherent quantum dynamics of a superconducting flux qubit. *Science*, 299:1869, 2003.

[18] T. A. Costi and A. C. Hewson. Resistivity cross-over for the non-degenerate anderson model. *Philosophical Magazine Part B*, 65(6):1165–1170, 1992.

[19] D M Cragg, P Lloyd, and P Nozieres. On the ground states of some s-d exchange kondo hamiltonians. *Journal of Physics C: Solid State Physics*, 13(5):803–817, February 1980.

[20] A J Daley, C Kollath, U Schollwöck, and G Vidal. *J. Stat. Mech.*, page 04005, 2004.

[21] S. Daul, I. Ciofini, C. Daul, and S. R. White. *Int. J. Quantum Chem.*, 79:331, 2000.

[22] W.J. De Haas and G.J. Van Den Berg. The electrical resistance of gold and silver at low temperatures. *Physica*, 3(6):440–449, June 1936.

[23] D. Deutsch. Quantum theory, the church-turing principle and the universal quantum computer. *Proceedings of the Royal Society of London. A. Mathematical and Physical Sciences*, 400(1818):97, 1985.

[24] J. Eisert, M. Cramer, and M. B. Plenio. Colloquium: Area laws for the entanglement entropy. *Reviews of Modern Physics*, 82(1):277–306, February 2010.

[25] G. Evenbly and G. Vidal. Entanglement renormalization in two spatial dimensions. *Physical Review Letters*, 102(18):180406, May 2009.

[26] G. Fano, F. Ortolani, and L. Ziosi. *Chem. Phys.*, 108:9246, 1998.

[27] Richard Feynman. Simulating physics with computers. *International Journal of Theoretical Physics*, 21(6):467–488, 1982.

[28] H. O. Frota and L. N. Oliveira. Photoemission spectroscopy for the spin-degenerate anderson model. *Phys. Rev. B*, 33(11):7871–7874, Jun 1986.

[29] H. O. Frota and L. N. Oliveira. Photoemission spectroscopy for the spin-degenerate anderson model. *Physical Review B*, 33(11):7871–7874, June 1986.

[30] Matthew T. Glossop and Kevin Ingersent. Numerical renormalization-group study of the bose-fermi kondo model. *Physical Review Letters*, 95(6):067202, August 2005.

[31] Alex Grishin, Igor V. Yurkevich, and Igor V. Lerner. Low-temperature decoherence of qubit coupled to background charges. *Physical Review B*, 72(6):060509, August 2005.

[32] Zheng-Cheng Gu, Michael Levin, and Xiao-Gang Wen. Tensor-entanglement renormalization group approach as a unified method for symmetry breaking and topological phase transitions. *Physical Review B*, 78(20):205116, November 2008.

[33] F. Guinea, V. Hakim, and A. Muramatsu. Bosonization of a two-level system with dissipation. *Phys. Rev. B*, 32(7):4410–4418, Oct 1985.

[34] Karen A. Hallberg, Peter Horsch, and Gerardo Martinéz. Numerical renormalization-group study of the correlation functions of the antiferromagnetic spin-1/2 heisenberg chain. *Phys. Rev. B*, 52(2):R719–R722, Jul 1995.

[35] F. Hassler, G. Lesovik, and G. Blatter. Influence of a random telegraph process on the transport through a point contact. *The European Physical Journal B - Condensed Matter and Complex Systems*, 83(3):349–356, 2011.

[36] Patrik Henelius. Two-dimensional infinite-system density-matrix renormalization-group algorithm. *Phys. Rev. B*, 60(13):9561–9565, Oct 1999.

[37] Walter Hofstetter. Generalized numerical renormalization group for dynamical quantities. *Physical Review Letters*, 85(7):1508–1511, August 2000.

[38] S. Iblisdir, R. Orús, and J. I. Latorre. Matrix product states algorithms and continuous systems. *Physical Review B (Condensed Matter and Materials Physics)*, 75(10):104305, 2007.

[39] G. Ithier, E. Collin, P. Joyez, D. Vion, D. Esteve, J. Ankerhold, and H. Grabert. Zener enhancement of quantum tunneling in a two-level superconducting circuit. *Physical Review Letters*, 94(5):057004, February 2005.

[40] Eric Jeckelmann. Dynamical density-matrix renormalization-group method. *Phys. Rev. B*, 66(4):045114, Jul 2002.

[41] Eric Jeckelmann. Ground-state phase diagram of a half-filled one-dimensional extended hubbard model. *Physical Review Letters*, 89(23):236401, November 2002.

[42] H. C. Jiang, Z. Y. Weng, and T. Xiang. Accurate determination of tensor network state of quantum lattice models in two dimensions. *Physical Review Letters*, 101(9):090603, August 2008.

[43] B. A. Jones and C. M. Varma. Study of two magnetic impurities in a fermi gas. *Physical Review Letters*, 58(9):843–846, March 1987.

[44] J. Jordan, R. Orús, G. Vidal, F. Verstraete, and J. I. Cirac. Classical simulation of infinite-size quantum lattice systems in two spatial dimensions. *Physical Review Letters*, 101(25):250602, December 2008.

[45] Stefan Kirchner, Qimiao Si, and Kevin Ingersent. Finite-size scaling of classical long-ranged ising chains and the criticality of dissipative quantum impurity models. *Physical Review Letters*, 102(16):166405, April 2009.

[46] Roger H. Koch, David P. DiVincenzo, and John Clarke. Model for 1/f flux noise in SQUIDs and qubits. *Physical Review Letters*, 98(26):267003, June 2007.

[47] Jun Kondo. Resistance minimum in dilute magnetic alloys. *Progress of Theoretical Physics*, 32(1):37–49, 1964.

[48] H. R. Krishna-murthy, J. W. Wilkins, and K. G. Wilson. *Phys. Rev. B*, 21:1003, 1980.

[49] Till D. Kühner and Steven R. White. Dynamical correlation functions using the density matrix renormalization group. *Phys. Rev. B*, 60(1):335–343, Jul 1999.

[50] L. D. Landau. *Phys. Z. Sowjetunion*, 2:46, 1932.

[51] Karyn Le Hur, Philippe Doucet-Beaupré, and Walter Hofstetter. Entanglement and criticality in quantum impurity systems. *Physical Review Letters*, 99(12):126801, September 2007.

[52] A. J. Leggett, S. Chakravarty, A. T. Dorsey, Matthew P. A. Fisher, Anupam Garg, and W. Zwerger. Dynamics of the dissipative two-state system. *Rev. Mod. Phys.*, 59(1):1–85, Jan 1987.

[53] Michael Levin and Cody P. Nave. Tensor renormalization group approach to two-dimensional classical lattice models. *Physical Review Letters*, 99(12):120601, September 2007.

[54] Wei Li, Shi-Ju Ran, Shou-Shu Gong, Yang Zhao, Bin Xi, Fei Ye, and Gang Su. Linearized tensor renormalization group algorithm for the calculation of thermodynamic properties of quantum lattice models. *Physical Review Letters*, 106(12):127202, March 2011.

[55] H. G. Luo, T. Xiang, and X. Q. Wang. *Phys. Rev. Lett.*, 91:049701, 2003.

[56] Nobuya Maeshima, Yasuhiro Hieida, Yasuhiro Akutsu, Tomotoshi Nishino, and Kouichi Okunishi. Vertical density matrix algorithm: A higher-dimensional numerical renormalization scheme based on the tensor product state ansatz. *Physical Review E*, 64(1):016705, June 2001.

[57] Ian P. McCulloch. From density-matix renormalization group to matrix product stetes. *arXiv:cond-mat/0701428v3*.

[58] V. Meden, W. Metzner, U. Schollwöck, O. Schneider, T. Stauber, and K. Schönhammer. Luttinger liquids with boundaries: Power-laws and energy scales. *The European Physical Journal B*, 16(4):631–646, August 2000.

[59] Walter Metzner and Dieter Vollhardt. Correlated lattice fermions in $d = \infty$ dimensions. *Physical Review Letters*, 62(3):324–327, January 1989.

[60] Y. Nakamura, Yu. A. Pashkin, T. Yamamoto, and J. S. Tsai. Charge echo in a cooper-pair box. *Physical Review Letters*, 88(4):047901, January 2002.

[61] Satoshi Nishimoto, Eric Jeckelmann, Florian Gebhard, and Reinhard M. Noack. Application of the density matrix renormalization group in momentum space. *Phys. Rev. B*, 65(16):165114, Apr 2002.

[62] R. M. Noack, S. R. White, and D. J. Scalapino. Correlations in a two-chain hubbard model. *Phys. Rev. Lett.*, 73(6):882–885, Aug 1994.

[63] Luiz N. Oliveira and John W. Wilkins. New approach to the x-ray-absorption problem. *Physical Review B*, 24(8):4863–4866, October 1981.

[64] Wanda C. Oliveira and Luiz N. Oliveira. Generalized numerical renormalization-group method to calculate the thermodynamical properties of impurities in metals. *Physical Review B*, 49(17):11986–11994, May 1994.

[65] William D. Oliver, Yang Yu, Janice C. Lee, Karl K. Berggren, Leonid S. Levitov, and Terry P. Orlando. Mach-zehnder interferometry in a strongly driven superconducting qubit. *Science*, 310(5754):1653–1657, December 2005.

[66] Stellan Östlund and Stefan Rommer. Thermodynamic limit of density matrix renormalization. *Phys. Rev. Lett.*, 75(19):3537–3540, Nov 1995.

[67] E. Paladino, L. Faoro, G. Falci, and Rosario Fazio. Decoherence and 1/f noise in josephson qubits. *Physical Review Letters*, 88(22):228304, May 2002.

[68] Karlo Penc, Karen Hallberg, Frederic Mila, and Hiroyuki Shiba. Shadow band in the one-dimensional infinite- u hubbard model. *Physical Review Letters*, 77(7):1390–1393, August 1996.

[69] D. Perez-Garcia, F. Verstraete, M. M. Wolf, and J. I. Cirac. Matrix product state representations. *Quantum Inf. Comput.*, 7:401, 2007.

[70] Iztok PiÅŸorn and Frank Verstraete. Variational numerical renormalization group: Bridging the gap between NRG and density matrix renormalization group. *Physical Review Letters*, 108(6):067202, February 2012.

[71] E. Polizzi, F. Mila, and E. S. Sørensen. S=1/2 chain-boundary excitations in the haldane phase of one-dimensional s=1 systems. *Physical Review B*, 58(5):2407–2410, August 1998.

[72] S. Ramasesha, S. K. Pati, H. R. Krishnamurthy, Z. Shuai, and J. L. Brédas. *Synth. Met.*, 85:1019, 1997.

[73] Shinsei Ryu and Tadashi Takayanagi. Holographic derivation of entanglement entropy from the anti de sitter space conformal field theory correspondence. *Physical Review Letters*, 96(18):181602, May 2006.

[74] Hamed Saberi, Andress Weichselbaum, and Jan von Delft. *arXiv:0804.0193*, 2008.

[75] S. Sachdev. *Quantum Phase Transitions*. Cambridge University Press, 1999.

[76] Subir Sachdev. Quantum magnetism and criticality. *Nature Physics*, 4(3):173–185, 2008.

[77] Keiji Saito and Yosuke Kayanuma. Nonadiabatic electron manipulation in quantum dot arrays. *Physical Review B*, 70(20):201304, November 2004.

[78] A. W. Sandvik and G. Vidal. Variational quantum monte carlo simulations with tensor-network states. *Phys. Rev. Lett.*, 99:220602, 2007.

[79] P. Schmitteckert. *Phys. Rev. B*, 70:121302, 2004.

[80] T. Senthil, Ashvin Vishwanath, Leon Balents, Subir Sachdev, and Matthew P. A. Fisher. Deconfined quantum critical points. *Science*, 303(5663):1490–1494, March 2004.

[81] Qimiao Si, Silvio Rabello, Kevin Ingersent, and J. Lleweilun Smith. Locally critical quantum phase transitions in strongly correlated metals. *Nature*, 413(6858):804–808, October 2001.

[82] Mika Sillanpää, Teijo Lehtinen, Antti Paila, Yuriy Makhlin, and Pertti Hakonen. Continuous-time monitoring of landau-zener interference in a cooper-pair box. *Physical Review Letters*, 96(18):187002, May 2006.

[83] R. W. Simmonds, K. M. Lang, D. A. Hite, S. Nam, D. P. Pappas, and John M. Martinis. Decoherence in josephson phase qubits from junction resonators. *Physical Review Letters*, 93(7):077003, 2004.

[84] Erik S. So/rensen and Ian Affleck. S(k) for haldane-gap antiferromagnets: Large-scale numerical results versus field theory and experiment. *Physical Review B*, 49(18):13235–13238, May 1994.

[85] Masuo Suzuki. Fractal decomposition of exponential operators with applications to many-body theories and monte carlo simulations. *Physics Letters A*, 146(6):319–323, June 1990.

[86] Brian Swingle. Entanglement renormalization and holography. *arXiv:0905.1317*, May 2009.

[87] L. Thomas, F. Lionti, R. Ballou, D. Gatteschi, R. Sessoli, and B. Barbara. Macroscopic quantum tunnelling of magnetization in a single crystal of nanomagnets. *, Published online: 12 September 1996; | doi:10.1038/383145a0*, 383(6596):145–147, September 1996.

[88] F. Verstraete and J. I. Cirac. Renormalization algorithms for quantum-many body systems in two and higher dimensions. *arXiv:cond-mat/0407066*, July 2004.

[89] F. Verstraete and J. I. Cirac. Matrix product states represent ground states faithfully. *Physical Review B (Condensed Matter and Materials Physics)*, 73(9):094423, 2006.

[90] F. Verstraete, V. Murg, and J.I. Cirac. Matrix product states, projected entangled pair states, and variational renormalization group methods for quantum spin systems. *Advances in Physics*, 57(2):143–224, March 2008.

[91] F. Verstraete, D. Porras, and J. I. Cirac. Density matrix renormalization group and periodic boundary conditions: A quantum information perspective. *Phys. Rev. Lett.*, 93(22):227205, Nov 2004.

[92] G. Vidal. Classical simulation of infinite-size quantum lattice systems in one spatial dimension. *Physical Review Letters*, 98(7):070201, 2007.

[93] G. Vidal. Entanglement renormalization. *Physical Review Letters*, 99(22):220405, November 2007.

[94] Guifré Vidal. Efficient classical simulation of slightly entangled quantum computations. *Phys. Rev. Lett.*, 91(14):147902, Oct 2003.

[95] Matthias Vojta, Ralf Bulla, Fabian Gï¿œttge, and Frithjof Anders. Mass-flow error in the numerical renormalization-group method and the critical behavior of the sub-ohmic spin-boson model. *Physical Review B*, 81(7):075122, February 2010.

[96] Matthias Vojta, Ning-Hua Tong, and Ralf Bulla. Quantum phase transitions in the sub-ohmic spin-boson model: Failure of the quantum-classical mapping. *Physical Review Letters*, 94(7):070604, February 2005.

[97] Matthias Vojta, Ning-Hua Tong, and Ralf Bulla. Erratum: Quantum phase transitions in the sub-ohmic spin-boson model: Failure of the quantum-classical mapping [Phys. rev. lett. 94, 070604 (2005)]. *Physical Review Letters*, 102(24):249904, June 2009.

[98] Rok Žitko and Thomas Pruschke. Energy resolution and discretization artifacts in the numerical renormalization group. *Physical Review B*, 79(8), February 2009.

[99] Xiaoqun Wang and Tao Xiang. Transfer-matrix density-matrix renormalization-group theory for thermodynamics of one-dimensional quantum systems. *Phys. Rev. B*, 56(9):5061–5064, Sep 1997.

[100] A. Weichselbaum, F. Verstraete, U. Schollwöck, J. I. Cirac, and Jan von Delft. Variational matrix-product-state approach to quantum impurity models. *Physical Review B*, 80(16):165117, October 2009.

[101] Andreas Weichselbaum and Jan von Delft. Sum-rule conserving spectral functions from the numerical renormalization group. *Physical Review Letters*, 99(7):076402, August 2007.

[102] W. Wernsdorfer, M. Murugesu, and G. Christou. Resonant tunneling in truly axial symmetry mn_12 single-molecule magnets: Sharp crossover between thermally assisted and pure quantum tunneling. *Physical Review Letters*, 96(5):057208, February 2006.

[103] S. R. White. *Phys. Rev. B*, 48:345, 1993.

[104] S. R. White and R. L. Martin. *Chem. Phys.*, 110:4127, 1999.

[105] Steven R. White. Density matrix formulation for quantum renormalization groups. *Physical Review Letters*, 69(19):2863–2866, November 1992.

[106] Steven R. White. Spin gaps in a frustrated heisenberg model for *cav*4*o*9. *Phys. Rev. Lett.*, 77(17):3633–3636, Oct 1996.

[107] Steven R. White. Density matrix renormalization group algorithms with a single center site. *Physical Review B*, 72(18):180403, November 2005.

[108] Steven R. White and Adrian E. Feiguin. *Phys. Rev. Lett.*, 93:076401, 2004.

[109] Steven R. White and David A. Huse. Numerical renormalization-group study of low-lying eigenstates of the antiferromagnetic s=1 heisenberg chain. *Physical Review B*, 48(6):3844–3852, August 1993.

[110] Kenneth G. Wilson. The renormalization group: Critical phenomena and the kondo problem. *Rev. Mod. Phys.*, 47(4):773–840, Oct 1975.

[111] André Winter, Heiko Rieger, Matthias Vojta, and Ralf Bulla. Quantum phase transition in the sub-ohmic spin-boson model: Quantum monte carlo study with a continuous imaginary time cluster algorithm. *Physical Review Letters*, 102(3):030601, January 2009.

[112] D. Witthaut, E. M. Graefe, and H. J. Korsch. Towards a generalized landau-zener formula for an interacting bose-einstein condensate in a two-level system. *Physical Review A*, 73(6):063609, June 2006.

[113] T. Xiang. Density-matrix renormalization-group method in momentum space. *Phys. Rev. B*, 53(16):R10445–R10448, Apr 1996.

[114] Tao Xiang, Jizhong Lou, and Zhaobin Su. Two-dimensional algorithm of the density-matrix renormalization group. *Phys. Rev. B*, 64(10):104414, Aug 2001.

[115] Z. Y. Xie, H. C. Jiang, Q. N. Chen, Z. Y. Weng, and T. Xiang. Second renormalization of tensor-network states. *Physical Review Letters*, 103(16):160601, October 2009.

[116] M. Yoshida, M. A. Whitaker, and L. N. Oliveira. Renormalization-group calculation of excitation properties for impurity models. *Physical Review B*, 41(13):9403–9414, May 1990.

[117] C. Zener. *Proc. R. Soc. London*, 137:696, 1932.

Acknowledgements

First and most I want to thank my supervisor Prof. Jan von Delft for his patient help, invaluable advices, timely encouragement and generous support during my PhD study. His attitude towards work, his way of thinking and his role as a group leader are great examples for me to learn. I also enjoyed his humor and wisdom a lot in numerous meetings and discussions.

I acknowledge many valuable discussions with my collaborators Prof. Matthias Vojta, Prof. Florian Marquardt and Prof. Stefan Kehrein.

I want to thank my colleague, collaborator and friend Dr. Andreas Weichselbaum for the countless fruitful and exciting discussions. He often has a very different point of view with me, and his opinion is therefore extremely helpful.

I thank my former colleague Barbara, Theresa, Michael, Peter, Hamed, Max, Clemens, Wolfgang and Alex for all the kind and heartwarming help when I just started to work and live in Germany. I thank my officemates Andreas, Markus, Constantin, Stefan, Annika, Benedikt, Florian, Wael and colleagues Max, Olga, Jiang, Oliver, Arne, Florian, Markus, Jan, Oleg, Pei, Wei, Björn, Korbinian, Jad, Katharina, Kati, Stephan, Stephan and Fabian for the wonderful time together. The moments shared with you are the most cherished memory in my PhD time.

I thank our secretaries Stéphane Schoonover and Sylvia Kaiser for helping me with the administrative stuff. I thank the LRZ cluster administrators for their excellent work.

I acknowledge the CeNS IDK PhD program and the NIM graduate program for the financial support and excellent workshops and training opportunities they have provided. I acknowledge Prof. Ignacio Cirac to give me the honour to be my second supervisor of the IDK program. I am thankful to Maria, Kamila and many others in CeNS for organizing many unforgettable events.

I thank Andreas, Markus, Jon, Benedikt and Ricky for extremely careful proofreading of my thesis and many suggestions on it. I thank Olga for translating the abstract into German.

I thank Nicola for providing me with the most pleasant place to live during the past two years. I thank Alex, Korbi, Donato, Lawrence and other flat mates in Munich for having so much fun living together. I feel especially grateful to have Ema's warming company during my thesis writing. I feel extremely grateful to have the Fantastic Four, the Karaoke group, the small Munich Chinese Speakers group and many great friends. I am deeply grateful to have the love and support from my family back in China.